PREDICTION OF THE CONCENTRATION POLARIZATION AND THE FOULING FORMATION IN MEMBRANE DESALINATION PROCESSES

A Dissertation

by

WENDE LI

Submitted to the Office of Graduate and Professional Studies of
Texas A&M University
in partial fulfillment of the requirements for the degree of

DOCTOR OF PHILOSOPHY

Chair of Committee,	Alan Palazzolo
Co-Chair of Committee,	Shehab Ahmed
Committee Members,	Ying Li
	Sai Lau
Head of Department,	Ying Li

May 2019

Major Subject: Mechanical Engineering

ABSTRACT

Membrane desalination provides fresh water product beyond the hydrologic cycle, and is promising especially for coastal regions with a freshwater shortage. Membrane lifetime and permeate flux are affected by the concentration polarization (CP) phenomenon and membrane surface fouling. A numerical simulation model based on the lattice Boltzmann method (LBM) is developed and an effective flux boundary scheme is proposed in this study to predict CP and inorganic fouling growth.

Results of the CP and permeate flux prediction are compared with published results in a complete rejection condition. When the membrane rejection rate is considered, prediction results show that a higher membrane rejection rate results in not only better product water quality but also higher CP and lower permeate flux. CP and permeate prediction results in a spacer filled desalination channel indicate that there is a higher fouling potential immediately behind the spacer filaments.

Coupling of the CP prediction model with gypsum growth kinetics provides an approach to study inorganic fouling growth on the membrane surface at a single crystal level. The axially asymmetric growth of the gypsum crystal shown in the fouling growth result could be explained by the concentration field result that the salt concentration decreases from the crystal frontal flow-stagnation edge to the rear of the crystal. Predicted equivalent radius and accumulated mass of the growing gypsum crystal agree with analytical results and published test data.

A vibration assisted desalination process is proposed and experimentally realized using a periodically oscillating desalination cell. Test data shows that CP near membrane surface can be reduced in the vibration assisted desalination. A slower flux decline can be observed in the vibration assisted desalination with a larger vibration velocity. Experimental observations

validate that the proposed vibration assisted desalination process helps enhance the permeate flux and mitigate the formation of inorganic fouling on the RO membrane surface.

A novel desalination centrifuge is designed in this study to reduce desalination hardware cost and mitigate membrane fouling. An estimation of energy consumption of the designed centrifuge shows that under certain conditions, the power usage by the desalination centrifuge is less than the industrial average.

DEDICATION

This dissertation is dedicated to my wife Mrs. Chao Zhang. Thank you for your support along the way.

ACKNOWLEDGEMENTS

This work would not have been possible without the financial support of the Texas A&M University Assistantship and Qatar National Research Fund. First and foremost, I am especially indebted to my supervisor, Professor Alan Palazzolo. He provided me valuable instructions and helped me solve detailed problems. His dedication, his kindness and his respect to others will always be my guidelines of conduct in my future career and life.

I also would like to express my gratitude to my co-advisor, Profess Shehab Ahmed. He is always supportive to my work, and he is very considerate to team members.

Same thanks are extended to Professor Sai Lau and Professor Ying Li for their guidance of my research and their service as my committee members.

I appreciate my teammate, Dr. Xu Su, for his support and cooperation. We shared same excitement and happiness, and I will miss the time when we work together.

I would like to thank Mr. Erwin Thomas for his continuous help in the experimental test rig design and operation.

I would also like to thank Professor Iman Borazjani, for this agreement in joining my final defense as a substitute member for Professor Sai Lau.

Finally, and most importantly, I would like to thank my parents, my wife and my daughter, for their unconditional love and support.

CONTRIBUTORS AND FUNDING SOURCES

This work was supervised by a dissertation committee consisting of Professor Alan Palazzolo (advisor) of the Department of Mechanical Engineering, Professor Shehab Ahmed (co-advisor) of the Department of Electrical Engineering, Professors Sai Lau and Ying Li of the Department of Mechanical Engineering.

All other work conducted for the dissertation was completed by the student independently.

Graduate study was supported by Qatar National Research Fund (NPRP No.: 6-213-2-090, Centrifugal Pressure Vibrating Membrane Reverse Osmosis Desalination and Fracking Waste Water Recovery).

NOMENCLATURE

$\mathbf{u}$	fluid velocity vector, [m/s]
C	solute concentration, [kg/m^3] or [g/L]
C_0	feed water concentration, [kg/m^3] or [g/L]
C_b	feed water buck flow concentration, [kg/m^3] or [g/L]
C_p	permeate water concentration, [kg/m^3] or [g/L]
C_w	solute concentration at the boundary wall nodes, [kg/m3] or [g/L]
C_f	solute concentration at the boundary fluid nodes, [kg/m3] or [g/L]
C_s	solute saturation concentration, [kg/m3] or [g/L]
D	diffusion coefficient or diffusivity, [m^2/s]
δ_c	concentration polarization boundary layer thickness, [m]
k	mass transfer coefficient, $k = D/\delta_c$, [m/s]
ρ	fluid density, [kg/m^3]
$\mathbf{n}$	unit normal vector to a boundary
u_0	centerline (maximum) velocity of the fluid in a plain channel, [m/s]
H_c	height of the desalination channel, [m]
W_c	width of the desalination channel, [m]
L_c	length of the desalination channel, [m]
d_h	hydraulic diameter, [m]
L	characteristic length, [m]
v	kinematic viscosity of fluid, $v = \mu/\rho$, [m^2/s]
μ	dynamic viscosity or absolute viscosity of fluid, [(N·s/m^2)] or [kg/(m·s)]
Re	Reynolds number, Re = uL/v with u the fluid velocity with respect to the object

Sc	Schmidt number, Sc = v/D
Sh	Sherwood number, Sh = kd_h/D
Pe	Peclet number, Lu/D with u the fluid velocity with respect to the object
v_w	permeate flux (volumetric flux), [m/s]
SI	supersaturation ratio
r_{eq}	equivalent radius of fouling formation, [m]
R_{obser}	observable removal efficiency of membrane
R_{true}	true removal efficiency of membrane
γ	shear rate, [1/s]
R_{ej}	membrane rejection rate
r_c	desalination system permeate water recovery ratio

TABLE OF CONTENTS

Page

LIST OF FIGURES

Page

LIST OF TABLES

Page

1. INTRODUCTION

This section covers a background introduction of the present research in saline water desalination, recent studies in predictions of the concentration polarization (CP) and membrane fouling formation, and a summary of membrane fouling mitigation strategies in academia and in industry.

1.1. Research Background

Water covers 71% of the earth surface and plays a vital role in the survival of all living organisms. Fresh water is vital for people and wildlife, and its withdrawal is necessary for agriculture, industry and domestic use. Fresh water is usually defined as water with less than 500 ppm (parts per million) of total dissolved salts. Out of all water sources on earth, saline water such as seawater and saline groundwater makes up about 97% of all water sources, and only 3% of earth water sources is fresh water in nature. About 2/3 of fresh water in nature is frozen in glaciers and polar ice caps and most of the rest 1/3 is fresh groundwater and soil moisture (only 1% of the fresh water in nature is surface fresh water in lakes, swamps and rivers). The fresh groundwater, soil moisture and surface fresh water is considered available fresh water, which is about 0.5% - 0.8% of the total water resource on earth.

Fresh ground water and surface fresh water is not always sufficiently available, and the scarcity is expected to increase in the future [1]. Regions with limited water resources and rapid population growth are facing an increasing freshwater shortage. Freshwater scarcity is not only a regional challenge but also a global crisis. Therefore, people are seeking alternative water sources such as wastewater and saline water to provide supplementary freshwater to human societies and to relieve the water shortage pressure. However, different from traditional fresh water sources, intensive treatments are needed for these alternative water sources to obtain fresh

water, and such treatments like wastewater reclamation and saline water desalination. Although wastewater reclamation is more energy efficient than salt water desalination, its freshwater product is not enough to meet the increasing demand.

Freshwater product from saline water desalination is beyond the hydrologic cycle, which refers to the continuous exchange of water within the hydrosphere, between the atmosphere, soil water, surface water, groundwater, and plants. Besides water purification techniques for wastewater and saline water, a coordinated approach involving water management, water purification, and water conservation [2] could be adopted to address the freshwater shortage.

Two most commercially successful saline water desalination technologies are thermal distillation and membrane separation. The thermal distillation technology includes multi-stage flash (MSF), multi-effect distillation (MED), vapor compression (VC), etc., whereas the membrane technology includes reverse osmosis (RO) and electro-dialysis (ED), etc. The energy consumption of these most commonly used methods in seawater desalination are shown in Table 1.1 [3], which indicates that thermal distillation requires higher energy than RO membrane desalination. By 2010, the membrane separation technologies accounted about 38%, 87% and 79% of the total water production from sources of seawater, brackish water and wastewater, respectively [4]. RO desalination has been widely applied and is recognized as the leading saline water desalination technology [5].

Table 1.1 Energy Consumption of Main Desalination Processes (A. Al-Karaghouli, 2013)

Properties	**SWRO**	**BWRO**	**MSF**	**MED**
Electrical (kW h/m3)	4-6	1.5-2.5	2.5-5	2-2.5
Thermal (MJ/m3)	None	None	190-282	145-230
Total (kW h/m3)	4-6	1.5-2.5	19.58-27.25	14.45-21.35
Water Quality (ppm)	400-500	200-500	≈10	≈10

Although membrane desalination consumes less energy than thermal distillation [3], it still suffers several aspects of limitations. For example, membrane desalination usually is feedwater quality sensitive, has relatively low production rate, and suffers membrane fouling. Membrane lifetime and permeate flux are primarily affected by CP and membrane fouling [2]. CP arises when a portion of water solvent passes through the membrane and rejected solute ions tend to accumulate in the vicinity of the membrane surface, as illustrated in Figure 1.1. A steady-state concentration gradient will be established when the solute convection process is balanced by the solute back-diffusion process. Thus, CP leads to an elevated solute concentration near the membrane surface. The development of CP in a membrane desalination channel is affected by local hydrodynamic conditions and mass transport conditions. True CP values usually are difficult to observe experimentally [6]. Thus, a numerical CP prediction model is useful and even crucial for the performance estimation and process improvement in membrane desalination [7].

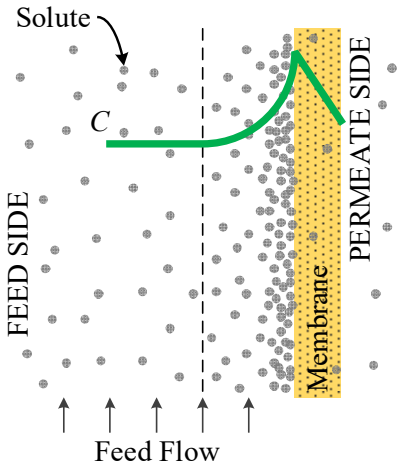

Figure 1.1 Illustration of CP Near the Membrane

The inherent CP reduces transmembrane pressure and plays a vital role in triggering membrane fouling. Membrane surface fouling enhances CP in turn since it hinders back-diffusion of salt ions, this is called the cake-enhanced CP phenomenon [8]. One popular opinion says that the rapid decline of permeate flux over time is a result of membrane fouling, especially

inorganic fouling [9], which is a also major obstacle for the wide application of membrane desalination [10][11]. Membrane fouling in saline water desalination results in reduced plant productivity, deteriorated permeate quality, increased energy consumption, higher treatment cost, and shorter membrane life span [12].

Despite extensive studies in CP and membrane fouling in membrane desalination processes, fundamental mechanisms in terms of fluid dynamics and mass transport for in CP formation and fouling growth are still not fully understood.

1.2. Studies of CP

The CP phenomenon has been widely studied for membrane desalination processes. The stagnant film model (or the classical film theory) provided an intuitive explanation of the CP phenomenon [13]. However, in the stagnant film model, the assumption of a uniform CP layer and invariant permeate flux along the desalination channel is not accurate for cross-flow membrane desalination, where the CP layer develops gradually along the desalination channel. Also, the constant permeate flux assumption also leads to significant errors in the CP prediction [14]. In later studies, numerical methods were used to solve the solute transport equation involving convection and diffusion in a desalination channel, such numerical methods like the finite difference method [6][14] and the finite element method [15]. However, all these works employed a simplified laminar velocity profile in a porous wall channel with a theoretical solution proposed by Berman [16]. Thus, the detailed interaction between flow momentum and mass transport in the membrane desalination process was not sufficiently reflected.

The presence of the feed spacer (or so-called turbulence promoter) in the desalination channel affects the concentration distribution in the channel, thus special attention is required for the feed spacer during the simulation. It has been reported in the literature [17] that feed spacers

can significantly alter hydrodynamic conditions and mass transfer patterns in the membrane desalination channel. The commercial computational fluid dynamics (CFD) software has been applied as a rigorous tool to predict CP with different feed spacer configurations. The main advantage of the CFD software lies in its ability to represent hydrodynamics and mass transfer properties in complex geometries utilizing finite element or finite volume numerical approaches [18][19]. The enormous improvements in computational methods facilitate the developing of more flexible and advanced algorithms that surpass the commercial CFD software to solve hydrodynamics coupling mass transport problems. Song [20] developed a two-dimensional streamline finite element model to numerically solve the convection-diffusion equation and Navier-Stokes equations in a feed channel to predict CP with the presence of the feed spacer. The impact of the spacer filament geometry on CP and permeate flux was further studied by Song [21] with the same method.

Kromkamp [22] developed a numerical model in the lattice Boltzmann method (LBM) to predict CP in microfiltration of suspension flow. This study [22] assumed that suspended particles are fully retained by applying non-flux boundary conditions on the membrane. However, this study [22] didn't consider influences of the membrane rejection rate and spacer filaments in the desalination channel on the CP prediction.

1.3. Studies of Membrane Fouling

1.3.1. Simulation of Membrane Fouling

Increased concentration near the membrane surface may cause over-saturation of sparingly soluble salts, such as calcium sulfate dihydrate (gypsum, $CaSO_4 \cdot 2H_2O$), calcium carbonate (calcite, $CaCO_3$), and barium sulfate (barite, $BaSO_4$), especially in desalination of brackish water with higher recovery ratios. When the mineral salt concentration exceeds its saturation, mineral

scaling on the membrane surface appears (due to homogenous and heterogeneous mineral salt crystallization) which decreases the available permeation surface for fresh water, leading to a decline of overall permeate flux [23]. Crystallization on the membrane surface [24] by inorganic salts such as the aforementioned $CaSO_4$, $CaCO_3$ and $BaSO_4$ is a common fouling mechanism. During the pressure-driven membrane desalination process, ions of inorganic salts are rejected and a CP layer will be formed, which results in an initial flux decline due to the increase of osmotic pressure. If nucleation of inorganic salts occurs in an over-saturation condition, a scaling layer will be formed at the nucleation position on the membrane surface, then a further flux will be induced.

Permeate flux decline due to membrane surface fouling was explained by two mechanisms, cake formation (modeled by resistance-in-series) and surface crystallization (modeled by surface blockage). Okazaki [25] proposed a cake-filtration mechanism to explain permeate flux decline due to gypsum precipitation on the membrane. However, Hasson [26] argued that the flux decline mechanism actually involves blockage of the membrane surface by lateral growth of the deposit rather than the hydraulic resistance of a cake building up at the membrane surface. Thereafter, a flux decline model was proposed by Hasson [27] based on the surface blockage mechanism, which fitted flux decline data better than previous studies with the speculatively assumed cake filtration mechanism. The cake formation and the surface blockage may occur simultaneously as the bulk phase becoming supersaturated when the membrane operates at high recovery ratios. Thus, the resulting permeate flux due to membrane fouling can be represented by combining the cake filtration and the surface blockage model [4]. In addition to characterize formed fouling on the membrane surface using permeate flux, Hasson [28] and Cohen [29] derived gypsum growth kinetics and directly quantified gypsum fouling accounting factors that

affect crystal growth, such as the mass transfer coefficient and the solution supersaturation ratio. Inorganic fouling growth is often a slow kinetic process, and fouling mitigation strategies typically rely on thermodynamic solubility calculations and experimental trial and error. Numerical modeling could be an effective and economical method for the direct simulation of fouling growth and the characterization of local flow and concentration fields.

Visual inspection and microscopy, although require disassembly of test modules, are direct methods to evaluate the extent of inorganic fouling in certain operating conditions and to check effects of fouling mitigation strategies. Cohen [30] developed a visual inspection method to study the gypsum scale formation in a plate-and-frame RO module via flux decline measurement and membrane surface imaging. Thereafter, Cohen [31] utilized the aforementioned direct visual observation method in [30] to quantify mineral scale nucleation and crystal growth on the RO membrane surface, and to test the effectiveness of antiscalants in retarding mineral scale formation. However, this direct observation method was constrained by dimensions of the test module, such as the membrane surface area, the membrane length, and the channel height, thus it may not be effective as a prediction tool for other desalination systems. Also, the development of the hardware module, as well as the destructive testing feature of this method are also uneconomical. Furthermore, the fouling attachment will be disturbed during the disassembly process, thus the accuracy of this observation method will be reduced. Although a non-destructive scale observation detector consisting of a plate-and-frame RO cell with an optical window, an optical microscope, and a high-resolution digital camera, was developed for a real-time monitoring of the mineral surface scaling on the RO membrane [32]. Except the real-time fouling observation function, this direct observation method still does not provide field results, such as fluid dynamics and solute concentration distribution.

Numerical modeling should be an effective and economical method for a direct simulation of fouling growth and to provide local field results. Picioreanu [33] developed a two-dimensional mathematical model integrating fluid dynamics and mass transport to study gypsum ($CaSO_4 \cdot 2H_2O$) scaling in a spacer filled desalination channel. The thickness of the outer scaling layer during the precipitate expansion is tuned by fitting experimental data while the inner precipitate layer does not grow. However, this study [33] only focused on crystal mass accumulation on a two-dimensional cross-section of the feed channel, while the expansion of gypsum fouling on the membrane surface parallel to channel plates was not addressed. Johns [34] performed a three-dimensional simulation for biofilm growth in porous media, which showed a promising applicability of LBM in mass transport problems. However, literatures involving the modeling and the prediction of inorganic fouling growth on the membrane surface to facilitate direct fouling simulation and visualization are still very limited.

1.3.2. Membrane Fouling Mitigation

RO membrane fouling is a complicated problem affected by a number of complex physical and chemical parameters. Parameters include: 1) feed solution chemistry, particle size, foulant concentration and solution pH values; 2) membrane hydrophilicity and surface roughness; and 3) operating pressure, cross flow velocity and feed temperature etc. Fane [12] summarized these factors into three categories: feed water characteristics, membrane properties, and hydrodynamic conditions.

Thus, the most common fouling mitigating techniques can be correspondingly grouped into three categories: 1) feed water pretreatment; 2) RO membrane modification; and 3) optimization and alteration of operating conditions. Besides these fouling mitigating techniques, membrane cleaning process is vital to reduce already formed fouling.

1.3.2.1. Pretreatment

Feed water pretreatment focuses on removing source water constituents and adjusting feed water chemistry, and is necessary to prevent membrane fouling and prolong the membrane lifetime. Currently, conventional pretreatment includes disinfection, coagulation and filtration, while non-conventional pretreatment includes microfiltration, ultrafiltration and the beach-well system [35]. The high ionic strength in seawater reduces the effectiveness of traditional pretreatment, thus making it difficult to remove problematic constituents. From the energy consumption point of view, the overall energy consumption of new SWRO plants is three to four times higher than the theoretical minimum due to the need for extensive pretreatment and posttreatment steps [36]. Another effect of pretreatment is that coagulant residuals from the pretreatment process may negatively affect reverse osmosis membrane performance [37].

1.3.2.2. Antiscalants

The application of antiscalants in membrane desalination is also a pretreatment process in saline water desalination. Low dosage levels of antiscalants in pretreatment can prevent precipitation of scale-forming salts by retarding growth of mineral salt crystals and reduce the use of hazardous acids since one of the methods to prevent scaling is to reduce the feed water pH value [38]. Unluckily, the antiscalants are prone to enhancing biofilm growth on the RO membrane (up to 10 times of the membrane's normal biofilm growth rate) by either altering membrane surface properties or by serving as a nutritional source for microorganisms [4][39].

1.3.2.3. Membrane Properties

An innovative method involving the changing of membrane properties shows that by the membrane surface modification one can inhibit formation of membrane fouling, especially organic fouling and biofouling.

A validation case of this method was proposed by Elimelech [40] which used four polyamide thin-film composite membranes with different surface characteristics to test the influence of the membrane surface roughness on colloidal fouling. AFM analysis revealed that particles preferentially accumulate in the valleys of rough membranes and more severe flux decline was observed than smooth membranes.

Based on the finding that the RO membrane with a hydrophobic surface is particularly susceptible to organic fouling, Gilron [41] modified commercial RO membranes to get a hydrophilic RO membrane. And such modified membranes potentially show better resistance to hydrophobic foulants.

Lee [42] experimentally investigated a method to improve the fouling resistance to more general foulants by using hydrophilic epoxy compound on the membrane surface, hydrolyzed functional groups were then formed so that less foulants will be brought to the membrane. However, given that this membrane surface modification approach aims at increasing the hydrophilicity, this method cannot be applied to types of fouling resulting from the deposition of small organic molecules or inorganic salts since small particles are less likely to be affected by the hydrophilic membrane than hydrophobic foulants.

And one has to admit that advantages of membrane modification could be hardly observed under severe fouling conditions. Once the deposition of foulants has taken place, the surface modification is no longer effective to prevent fouling. This is because the effect of solute-membrane interaction is severely reduced and fouling could be dominated by foulant-deposits-foulant interaction instead of foulant-membrane interaction. Thus, the surface properties will no longer play a role in affecting further deposition of foulants [12][43]. Strategies like alternating

properties of hydrodynamics and thermodynamics in operating conditions are promising ideas to prevent the deposition of foulants on the membrane surface.

1.3.2.4. Near Membrane Hydrodynamics

Membrane fouling is strongly affected by membrane operating conditions, such as the cross-flow velocity and permeate flux. It is possible to improve the membrane filtration performance by altering hydrodynamic conditions near the membrane surface. In general, severe fouling occurs at larger permeate flux or smaller cross flow. The cross-flow velocity is defined as the superficial velocity of the feed stream travelling parallel (tangential) to the membrane surface. The cross-flow velocity has a direct influence on the near membrane mass transfer coefficient. Ackerberg [44] experimentally examined the enhancement of mass transfer in pulsatile flow. A higher near membrane mass transfer coefficient promotes back-diffusion of salt ions and reduces CP. Kennedy [45] proposed that a large near wall velocity induced by pulsating flow helps counteract CP. Therefore, the enhancement of the back-diffusion process by altering operating conditions are helpful to reduce CP and accordingly reduce membrane fouling.

Feasible methods of altering membrane operating conditions include: 1) increase the cross-flow velocity to promote solute back-diffusion; and 2) move the membrane to disturb the fluid-solid interface boundary layer. In the cross-flow RO system, solely increasing the cross-flow velocity is usually achieved by increasing operating pressure. However, both surface crystallization and bulk crystallization favor high operating pressure [4], thus this approach tends to promote membrane fouling. Bertram [46] experimentally investigated a tubular ceramic MF unit with periodically interrupted cross-flow to enhance flux of yeast suspension. The cross flow was interrupted periodically (6.3-6.8 Hz) by a pulsation generator. There was a maximum of 102% flux enhancement for the pulsating feed flow compare to the steady feed flow. However,

there are still very limited experimental and theoretical studies in altering the near membrane hydrodynamics reported in literatures for membrane desalination processes. One commercial application of the membrane moving approach to enhance the cross-flow velocity in RO membrane filtration is the vibratory shear enhanced process (VSEP) featuring a torsional membrane motion [47]. The VSEP unit operates at a fixed shaking frequency of approximately 55 Hz with an angular amplitude of 0° - 13°, corresponding to a linear motion of 0 - 3.2 cm at the outer edge of a disk with a 28 cm diameter. Experimental studies showed that there is an increased natural organic matter removal efficiency [48] and reduced inorganic scaling [49] with the VSEP technique. An increased shear rate γ was adopted to explain the mechanism of the effect in VSPE [50]. The shear rate, defined as $\gamma = (velocity\ scale)/(length\ scale)$ (s^{-1}) relates the cross-flow velocity gradient near the membrane. A larger cross-flow velocity gradient induces a higher shear rate and results in increased back-transport of particles away from the membrane surface. This phenomenon is termed as shear-induced diffusion [51]. The rotational shaking method in VSPE is limited by inconsistent shaking amplitudes throughout the membrane area due to radial differences, thus the vibration benefit is not fully achieved. Another approach associated with membrane operating conditions is the rotation of the RO module. The rotation of the RO module takes advantage of a high shear rate and the Taylor vortex instability to reduce the permeate flux decline due to reduced CP and membrane fouling [52].

1.4. Summary

CP and surface fouling are remarkable features affecting the performance of membrane desalination processes. In the present work, a numerical model for CP prediction and membrane fouling simulation is developed based on the lattice Boltzmann method. Boundary conditions involving hydrodynamics, mass transport and reactions are discussed and validated in the LBM

framework. A flux boundary scheme is developed to prescribe mass flux directly on the boundary, without the normal derivative calculation nor the boundary neighboring nodes interpolation. The flux boundary scheme is numerically validated with a number of cases with different flux boundary conditions. Successful applications of the proposed flux boundary scheme to large Peclet number convection-diffusion desalination processes reveal the CP and fouling phenomena.

A vibration assisted desalination process is proposed to reduce membrane surface CP and fouling. This process is realized experimentally by a vibratory desalination cell. The experimental setup is introduced and results about CP values and membrane fouling indices are discussed.

Finally, the design of a desalination centrifuge is introduced for a centrifugal reverse osmosis desalination idea. The design of the desalination centrifuge in intended to reduce energy consumption, mitigate membrane fouling and increase fresh water product during seawater desalination process. Details of the design and system dynamics are discussed. The power consumption of the centrifuge is also estimated in this work.

2. DEVELOPMENT AND VALIDATION OF THE NUMERICAL MODEL

In this section, a numerical model based on the lattice Boltzmann method (LBM) to predict CP and fouling in membrane desalination is developed. First, the basic derivation process from the Boltzmann equation to the lattice Boltzmann method is introduced. Thereafter, an LBM model solving coupled fluid dynamics and mass transport is developed. Then, basic boundary schemes for fluid dynamics and mass transport are introduced and validated. Finally, a flux boundary scheme for the numerical study of CP and membrane fouling is designed and validated with a variety of cases.

2.1. Introduction

The lattice Boltzmann method is a fluid simulation method originated from the kinetic theory of gases. The fundamental idea is that gases can be imagined as consisting of a large number of small particles moving with random motions. The exchange of momentum and energy is achieved through the particle streaming and the particle collision instead of solving Navier–Stokes equations. Although the streaming and collision processes are applied across a limited number of particles, the intrinsic particle interactions in viscous flow can be sufficiently represented.

LBM has been developed as a viable and effective computational method for the simulation of fluid dynamics and mass transport. Different from conventional numerical methods, which are based on the discretization of macroscopic continuum equations, LBM stems from kinetic theory and describes a system from the macroscopic scale [53]. Beyond successful applications in complex flows [54][55][56], LBM possesses wide applications in the energy and environmental science (such as heat and mass transfer in heterogeneous media [57]), chemical engineering

(such as chemical dissolution in porous media [58]), geology (such as mass transport in saturated karst [59]), and so on.

2.2. Development of the LBM Model

2.2.1. The Boltzmann Equation

For ideal gas, after the integration of the molecules motion, the Boltzmann transport equation can be obtained, as shown in Equation (2.1).

$$\left(\frac{\partial}{\partial t}+\boldsymbol{\xi}\cdot\nabla_{\mathbf{r}}+\frac{\mathbf{F}}{m}\cdot\nabla_{\xi}\right)f\left(\mathbf{r},\boldsymbol{\xi},t\right)=\Omega\left(f\right) \tag{2.1}$$

In Equation (2.1), the distribution function $f(\mathbf{r},\boldsymbol{\xi},t)$ is a fundamental variable in kinetic theory representing the density of particles with a velocity of $\boldsymbol{\xi} = (\xi_x,\xi_y,\xi_z)$ at space $\mathbf{x}$ and time t, $\mathbf{F}$ denotes the external force acting on particles at a point of $(\mathbf{r},\boldsymbol{\xi})$, and the source term $\Omega(f)$ is the collision operator representing the local redistribution of the distribution function f due to collisions, which is actually the rate of change between final and initial status of the distribution function.

The Boltzmann equation is difficult to solve because the collision term $\Omega(f)$ is very complicated. The original collision operator considers all the possible outcomes of two-particle collisions. Bhatnagar, Gross and Krook (BGK) [60] in 1954 introduced a simplified model for the collision operator, called the BGK collision operator, as shown in Equation (2.2).

$$\Omega\left(f\right)=-\frac{1}{\tau}\left(f-f^{\mathrm{eq}}\right) \tag{2.2}$$

In Equation (2.2), the parameter τ is the relaxation time related to the fluid viscosity in hydrodynamics or the diffusion coefficient in mass transport, and f^{eq} is the equilibrium distribution function such as the Maxwell-Boltzmann distribution function, as shown in Equation

(2.3). The BGK relaxation term as a replacement of the original collision operator indicates a relaxation of the distribution function towards an equilibrium state.

$$f^{\mathrm{eq}}\left(\mathbf{r},\boldsymbol{\xi},t\right)=\rho\left(\mathbf{r}\right)\left[\frac{m}{2\pi kT\left(\mathbf{r}\right)}\right]^{3/2}\exp\left\{-\frac{m\left[\boldsymbol{\xi}-\boldsymbol{\xi}_0\left(\mathbf{r}\right)\right]^2}{2kT\left(\mathbf{r}\right)}\right\} \tag{2.3}$$

In Equation (2.3), m is the particle mass, k is the Boltzmann constant, and $\rho(\mathbf{r})$ and $T(\mathbf{r})$ are the local density and temperature, respectively. The final Boltzmann-BGK model without external forces can be written in Equation (2.4) based on Equation (2.1).

$$\frac{\partial f}{\partial t}+\boldsymbol{\xi}\cdot\frac{\partial f}{\partial \mathbf{r}}=-\frac{1}{\tau}\left(f-f^{\mathrm{eq}}\right) \tag{2.4}$$

2.2.2. The Lattice Boltzmann Equation

By discretizing the Boltzmann-BGK model shown in Equation (2.4), the lattice Boltzmann equation (LBE) can be derived, as shown in Equation (2.5).

$$f_i\left(\mathbf{x}+\mathbf{e}_i\delta t,t+\delta t\right)=f_i\left(\mathbf{x},t\right)-\frac{1}{\tau}\left[f_i\left(\mathbf{x},t\right)-f_i^{\mathrm{eq}}\left(\mathbf{x},t\right)\right] \tag{2.5}$$

Equation (2.5) is also called the LBGK model. The subscript i in the discretized distribution function f_i indicates a discrete lattice direction, $\mathbf{e}_i$ denotes a discrete lattice velocity, δx is the lattice spacing, and δt is the time increment. A common terminology used in LBM to refer the dimension of the problem and the number of speeds is *DnQm*, where *n* represents the dimension of the problem (2 for 2D and 3 for 3D) and *m* refers to the speed model. For example, in a commonly used *D2Q9* lattice model, the discrete speeds and distribution functions are in 9 directions, thus the subscript $i = 1 \sim 8$ in Equation (2.5).

2.2.3. LBM Model for Convection-Diffusion

Mass transport of salt ions in feed water during membrane desalination can be described by the convection-diffusion process.

The convection-diffusion equation for a physical quantity without sources or sinks can be expressed in Equation (2.6).

$$\frac{\partial C}{\partial t} + \nabla \cdot \left(\mathbf{u}C - D\nabla C \right) = 0 \tag{2.6}$$

In Equation (2.6), C is the variable of interest (such as the species concentration in mass transport, or the temperature in heat transfer), D is the diffusivity or diffusion coefficient (such as the mass diffusivity in mass transport, or the thermal diffusivity in heat transfer), and $\mathbf{u}$ is the given velocity that the quantity is moving with.

The feed water is assumed to be incompressible in this study due to the low cross-flow velocity (about 0.1 m/s) in the desalination channel. Two sets of particle distribution functions are employed to simulate the convection-diffusion process. One set of distribution function is adopted to solve fluid dynamics and another set of distribution function is adopted to solve mass transport. The evolution of distribution functions describing the convection-diffusion process is governed by the LBGK model shown in Equation (2.7) [61][62].

$$\begin{cases} f_i\left(\mathbf{x} + \mathbf{e}_i \delta t, t + \delta t\right) = f_i\left(\mathbf{x}, t\right) - \dfrac{1}{\tau}\left[f_i\left(\mathbf{x}, t\right) - f_i^{\mathrm{eq}}\left(\mathbf{x}, t\right) \right] \\ g_i\left(\mathbf{x} + \mathbf{e}_i \delta t, t + \delta t\right) = g_i\left(\mathbf{x}, t\right) - \dfrac{1}{\tau_s}\left[g_i\left(\mathbf{x}, t\right) - g_i^{\mathrm{eq}}\left(\mathbf{x}, t\right) \right] \end{cases} \tag{2.7}$$

In Equation (2.7), $f_i(\mathbf{x},t)$ and $g_i(\mathbf{x},\mathrm{t})$ are the distribution functions for the fluid field and the concentration field, respectively, at space $\mathbf{x}$ and time t, and f_i^{eq} and g_i^{eq} are the equilibrium distribution functions for f_i and g_i, respectively. Again, the subscript of the distribution functions i is used to distinguish lattice speed directions, $\mathbf{e}_i$ denote a lattice velocity, δt is the time increment, τ and τ_s are the dimensionless relaxation times which control the rates approaching equilibrium for f_i and g_i, respectively. The kinematic viscosity v and the diffusion coefficient D are related to the dimensionless relaxation times by Equation (2.8) [61].

$$\begin{cases} \nu = (\tau - 1/2)c^2 \delta t / 3 \\ D = (\tau_s - 1/2)c^2 \delta t / 3 \end{cases} \tag{2.8}$$

The equilibrium distribution functions must be defined appropriately so that the mass and momentum are conserved [63]. For small fluid velocities and small Mach numbers, the equilibrium distribution functions in Equation (2.7) can be written in Equation (2.9) [64] in order to recover the Navier-Stokes equations [65] and the convection-diffusion equation [66].

$$\begin{cases} f_i^{\mathrm{eq}} = w_i \rho \left[1 + \dfrac{\mathbf{e}_i \cdot \mathbf{u}}{c_s^2} + \dfrac{(\mathbf{e}_i \cdot \mathbf{u})^2}{2c_s^4} - \dfrac{\mathbf{u} \cdot \mathbf{u}}{2c_s^2} \right] \\ g_i^{\mathrm{eq}} = w_i C \left[1 + \dfrac{\mathbf{e}_i \cdot \mathbf{u}}{c_s^2} \right] \end{cases} \tag{2.9}$$

In Equation (2.9), $\mathbf{u}$ is the fluid velocity, ρ is the fluid density, C is the solute mass concentration, and w_i is the weight coefficient. Note that the equilibrium distribution function g_i^{eq} can also be written as a similar form like f_i^{eq} [61]. Also, the lattice sound speed $c_s = c/\sqrt{3}$, and in which the lattice speed $c = \delta h/\delta t = 1$ for a standard square lattice with the lattice spacing $\delta h = \delta x = \delta y = 1$ and the lattice time step $\delta t = 1$. Weight coefficients $w_0 = 4/9$, $w_i = 1/9$ for $i = 1\sim4$, and $w_i = 1/36$ for $i = 5\sim8$ for a D2Q9 lattice model. The discrete velocity $\mathbf{e}_i$ can be given by Equation (2.10).

$$\mathbf{e}_i = \begin{cases} (0,0) & i = 0 \\ c\left\{\cos\left[(i-1)\pi/2\right], \sin\left[(i-1)\pi/2\right]\right\} & i = 1,2,3,4 \\ \sqrt{2}c\left\{\cos\left[(2i-9)\pi/4\right], \sin\left[(2i-9)\pi/4\right]\right\} & i = 5,6,7,8 \end{cases} \tag{2.10}$$

Macroscopic properties, such as the fluid density ρ, velocity $\mathbf{u}$, pressure p, and concentration C, are readily available from the distribution functions, as shown in Equation (2.11).

$$\rho = \sum_{i=0}^{8} f_i, \mathbf{u} = \frac{1}{\rho} \sum_{i=0}^{8} \mathbf{e}_i f_i, \; p = c_s^2 \rho, \; C = \sum_{i=0}^{8} g_i \tag{2.11}$$

Equation (2.11) indicates that macroscopic variables for the fluid mass density ρ and mass flux $\rho\mathbf{u}$ can be directly recovered by the zeroth order moment and the first-order moment of the fluid field distribution functions, respectively. The second-order moment $\mathbf{\Pi}$ of the fluid field distribution functions relates the momentum flux tensor $\mathbf{M}$. The equilibrium part of the second-order moment leads to the pressure (isotropic stress) and the convective term in the momentum flux tensor [67], as seen in Equation (2.12).

$$\Pi_{\alpha\beta}^{(0)} = \sum_{i=0}^{q-1} e_{i\alpha} e_{i\beta} f_i^{(0)} = c_s^2 \rho \delta_{\alpha\beta} + \rho u_\alpha u_\beta \tag{2.12}$$

In Equation (2.12), α and β are coordinates, $\delta_{\alpha\beta}$ is the Kronecker delta, and the equilibrium part of the distribution function $f_i^{(0)}$ is equal to the equilibrium distribution f_i^{eq} [68]. The non-equilibrium part of the second-order moment relates to the shear stress, as shown in Equation (2.13).

$$\begin{cases} \Pi_{\alpha\beta}^{(1)} = \sum_{i=0}^{q-1} e_{i\alpha} e_{i\beta} f_i^{(1)} \approx -\dfrac{\tau}{3\nu} \sigma_{\alpha\beta} = -\dfrac{2\rho\tau}{3} s_{\alpha\beta} \\ s_{\alpha\beta} = \frac{1}{2}\left(\partial_\alpha u_\beta + \partial_\beta u_\alpha\right); \sigma_{\alpha\beta} = \mu\left(\partial_\alpha u_\beta + \partial_\beta u_\alpha\right) \end{cases} \tag{2.13}$$

In Equation (2.13), $s_{\alpha\beta}$ is the shear linear deformation component (rate-of-strain tensor component), $\sigma_{\alpha\beta}$ is the shear stress component. The non-equilibrium part of the particle distribution function $f_i^{(1)}$ is equal to $(f_i - f_i^{(0)})$ [69]. Consequently, the component of the total momentum flux tensor $\mathbf{M}$ can be expressed in Equation (2.14).

$$M_{\alpha\beta} = p\delta_{\alpha\beta} + \rho u_\alpha u_\beta - \sigma_{\alpha\beta} = \Pi_{\alpha\beta}^{(0)} + \left(1 - \frac{1}{2\tau}\right)\Pi_{\alpha\beta}^{(1)} \tag{2.14}$$

Equation (2.11) also indicates that the concentration C can be calculated by the zeroth order moment of the concentration field distribution functions resembling the fluid filed treatment.

Both Navier-Stokes equations and the convection-diffusion equation can be recovered from the equilibrium distribution functions shown in Equation (2.9) via the Chapman-Enskog analysis with a second-order accuracy [70]. In LBM, the domain and boundary are discretized and the distribution functions are solved locally at each node through the collision process and the streaming process, as shown in Equation (2.15). Then the macroscopic parameters are determined following Equation (2.11) using the post-streaming form of the distribution functions.

$$\begin{cases} \varphi_i^+(\mathbf{x},t) = \varphi_i(\mathbf{x},t) - \dfrac{1}{\tau_\varphi}\left[\varphi_i(\mathbf{x},t) - \varphi_i^{\mathrm{eq}}(\mathbf{x},t)\right], \text{Collision} \\ \varphi_i(\mathbf{x}+\mathbf{e}_i\delta t, t+\delta t) = \varphi_i^+(\mathbf{x},t), \text{Streaming} \end{cases} \tag{2.15}$$

In Equation (2.15), the distribution function φ_i stands for either the fluid filed distribution function f_i or the concentration field distribution function g_i, and φ_i^+ is the post-collision form of the distribution function of φ_i. In the computing process, each lattice site at point $\mathbf{x}$ and time t stores m populations of φ_i for a *DnQm* LBGK model. In the collision step (or called the relaxation step), each population $\varphi_i(\mathbf{x},t)$ receives a collisional contribution and becomes $\varphi_i^+(\mathbf{x},t)$. The collision process is a local and algebraic operation. In the streaming step (or called the propagation step), all post-collision populations stream along their associated direction $\mathbf{e}_i$ to reach a neighboring lattice site where they become $\varphi_i(\mathbf{x}+\mathbf{e}_i\delta t, t+\delta t)$. The streaming process is a non-local operation [71].

2.2.4. Force Term Implementations

LBE for hydrodynamics without external forces can be expressed in Equation (2.5). In the presence of a force density term $\mathbf{F} = \rho\boldsymbol{\alpha}$ (force per volume or pressure gradient, with a unit of N/m^3 or Pa/m), where $\boldsymbol{\alpha}$ is the acceleration due to $\mathbf{F}$, the LBE must be modified to account for the force by adding an additional term to the LBE, as shown in Equation (2.16).

$$f_i\left(\mathbf{x}+\mathbf{e}_i\delta t, t+\delta t\right)=f_i\left(\mathbf{x},t\right)-\frac{1}{\tau}\left[f_i\left(\mathbf{x},t\right)-f_i^{\mathrm{eq}}\left(\mathbf{x},t\right)\right]+F_i\delta t \tag{2.16}$$

Note that during the implementation process, the force term F_i, which can be calculated by Equation (2.17) in order to match the correct Navier-Stokes equations [72], should be added to the post-collision distribution function f_i before the post-streaming process. And the lattice time step δt in Equation (2.16) is unity.

$$F_i=\left(1-\frac{1}{2\tau}\right)w_i\left[\frac{\mathbf{e}_i-\mathbf{u}}{c_s^2}+\frac{\left(\mathbf{e}_i\cdot\mathbf{u}\right)}{c_s^4}\mathbf{e}_i\right]\cdot\mathbf{F} \tag{2.17}$$

In Equation (2.17), F_i has a unit of kg/(m^3·s). The calculation of the fluid velocity **u** in Equation (2.11) should be updated with Equation (2.18) with the external force term **F**.

$$\mathbf{u}=\frac{1}{\rho}\sum_i\mathbf{e}_i f_i+\frac{\delta t}{2}\frac{\mathbf{F}}{\rho} \tag{2.18}$$

For a thermal lattice Boltzmann model, the LBE with a source term can be expressed in Equation (2.19).

$$h_i\left(\mathbf{x}+\mathbf{e}_i\delta t, t+\delta t\right)=h_i\left(\mathbf{x},t\right)-\frac{1}{\tau_h}\left[h_i\left(\mathbf{x},t\right)-h_i^{\mathrm{eq}}\left(\mathbf{x},t\right)\right]+H_i\delta t+\frac{1}{2}\left(\delta t\right)^2\frac{\partial H_i}{\partial t} \tag{2.19}$$

The term H_i represents the effect of viscous heating and can be determined by Equation (2.20) [73].

$$H_i=w_i\frac{\Phi}{\rho c_p}\left[1+\frac{\mathbf{e}_i\cdot\mathbf{u}}{c_s^2}\left(1-\frac{1}{2\tau_h}\right)\right] \tag{2.20}$$

In Equation (2.20), Φ is viscous heating term due to viscous dissipation, as shown in Equation (2.21) with a unit of $kg/(m\cdot s^3)$, c_p is the specific heat at constant pressure, and τ_h is the dimensionless relaxation time in heat transfer LBM.

$$\Phi=2\mu s_{\alpha\beta}s_{\alpha\beta}-\frac{2\mu}{3}\left(\nabla\cdot\mathbf{u}\right)^2 \tag{2.21}$$

For incompressible flow, the divergence of the flow velocity $\nabla \cdot \mathbf{u} = 0$, then Φ can be simplified, as shown in Equation (2.22).

$$\Phi = 2\mu s_{\alpha\beta} s_{\alpha\beta} = \mu |s|^2 \tag{2.22}$$

In Equation (2.21) and Equation (2.22), $s_{\alpha\beta}$ is the rate-of-strain tensor component, which can be calculated by the non-equilibrium part of the second-order moment shown in Equation (2.13).

2.3. Basic Boundary Schemes in LBM

Same as in other numerical methods, boundary schemes in LBM are critical for successful simulations of both fluid dynamics and mass transport. Usually the inward distribution functions from the solid boundary toward the fluid domain are unknown in the streaming process, and need to be determined following boundary condition constraints at the fluid-solid interface. There are a variety of boundary schemes existing for general or specific applications.

2.3.1. Basic Boundary Schemes for Fluid Dynamics

2.3.1.1. The Bounce-back Boundary Scheme

In hydrodynamics, the most common fluid-solid interface condition is the no-slip boundary. The bounce-back scheme in LBM can be used to model the no-slip boundary (stationary or moving) or flow-over obstacles. The bounce-back scheme follows a rule that distribution functions hitting a rigid wall during streaming are reflected back to where they originally came from. The bounce-back scheme indicates that there is no flux (no mass flux in fluid dynamics or in mass transfer) across the boundary since all particles are bounced back, and that there is no slip on the wall since there is no relative transverse motion between fluid and boundary [71].

For a stationary boundary wall, the bounce-back scheme can be expressed by Equation (2.23). In Equation (2.23), f_i^+ is the known post-collision distribution function at node $\mathbf{x}_f$, f_{i*} is the unknown post-streaming distribution function in the opposite direction of f_i^+. After the collision

process and in the streaming step, the post-collision distribution function f_i^+ at the boundary nodes $\mathbf{x}_f$ leave $\mathbf{x}_f$ at time t and encounter the wall surface at time $t+\delta t/2$ where it is reflected back with a velocity $\mathbf{e}_{i*} = -\mathbf{e}_i$, arriving at time $t+\delta t$ at the node $\mathbf{x}_f$ from which they came.

$$f_{i*}\left(\mathbf{x}_f + \mathbf{e}_i\,\delta t/2 + \mathbf{e}_{i*}\,\delta t/2, t+\delta t\right) = f_i^+\left(\mathbf{x}_f, t\right) \tag{2.23}$$

After the standard streaming step, unknown post-streaming distribution functions at boundary nodes should be calculated by Equation (2.23). For example, as illustrated in Figure 2.1, distribution functions f_1, f_3, f_4, f_7 and f_8 are known from the streaming process, and the unknow distribution functions can be specified as $f_2 = f_4^+, f_5 = f_7^+$, and $f_6 = f_8^+$.

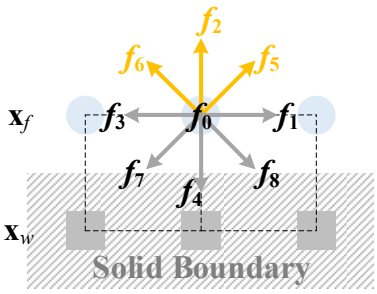

Figure 2.1 Illustration of a Straight Bottom Boundary

The standard bounce-back formula shown in Equation (2.23) should be corrected to count a given amount of momentum for a moving boundary wall, as shown in Equation (2.24) [74], in order to prescribe a no-slip wall boundary with a wall velocity vector $\mathbf{u}_w$.

$$f_{i*}\left(\mathbf{x}_f + \mathbf{e}_i\,\delta t/2 + \mathbf{e}_{i^*}\,\delta t/2, t+\delta t\right) = f_i^+\left(\mathbf{x}_f, t\right) + 2w_i\rho_w \frac{\mathbf{e}_{i*}\cdot\mathbf{u}_w}{c_s^2} \tag{2.24}$$

Equation (2.24) shows that only the velocity component along the link direction ($\mathbf{e}_{i*}\cdot\mathbf{u}_w$) is included in the calculation of unknown post-streaming distribution functions. Also, in Equation (2.24), ρ_w is the fluid density defined at the wall location $\mathbf{x}_w = \mathbf{x}_f + 1/2\mathbf{e}_i\delta t$. The bounce-back scheme for a moving boundary shown in Equation (2.24) can be used to prescribe a known velocity boundary, i.e. a Dirichlet boundary condition.

It is known the bounce-back scheme in LBM assumes that the boundary is located midway between solid and boundaries. So, if in a validation simulation, a half lattice spacing should be taken into consideration when using the bounce-back scheme.

2.3.1.2. The Zou-He Velocity Scheme

In LBM, a general approach to find the fluid density on a straight boundary subject to a Dirichlet velocity boundary is through the fluid velocity **u** and mass flux $\rho\mathbf{u}$ calculated in Equation (2.11). For a straight bottom wall shown in Figure 2.1, the zeroth order moment and the first-order moment of the fluid field distribution functions can be calculated as shown in Equation (2.25).

$$\begin{cases} \rho_w = \sum_{i=0}^{8} f_i = \underbrace{f_0 + f_1 + f_3 + f_4 + f_7 + f_8}_{\text{known}} + \underbrace{f_2 + f_5 + f_6}_{\text{unknown}} \\ \rho_w u_{w,x} = \sum_{i=0}^{8} \mathbf{e}_i f_i \cdot \mathbf{i} = \underbrace{c\left(f_1 - f_3 + f_8 - f_7\right)}_{\text{known}} + \underbrace{c\left(f_5 - f_6\right)}_{\text{unknown}} \\ \rho_w u_{w,y} = \sum_{i=0}^{8} \mathbf{e}_i f_i \cdot \mathbf{j} = \underbrace{-c\left(f_4 + f_7 + f_8\right)}_{\text{known}} + \underbrace{c\left(f_2 + f_5 + f_6\right)}_{\text{unknown}} \end{cases} \tag{2.25}$$

In Equation (2.25), the boundary velocity to be prescribed $\mathbf{u}_w = (u_{w,x}, u_{w,y})$, the lattice speed c is unity. The fluid density at the wall node can first be determined from Equation (2.25) as shown in Equation (2.26).

$$\rho_w = \frac{1}{1 - u_{w,y}}\left[f_0 + f_1 + f_3 + 2\left(f_4 + f_7 + f_8\right)\right] \tag{2.26}$$

However, f_2, f_5 and f_6 remain underdetermined. To close the system, Zou and He [75] proposed that bounce-back rule is still correct for the non-equilibrium part of distribution functions normal to the boundary. Thus, for the bottom boundary shown in Figure 2.1, f_2-f_2^{eq} = f_4-f_4^{eq}. With f_2 obtained, f_5 and f_6 can be found, as shown in Equation (2.27).

$$\begin{cases} f_2 = f_4 + \dfrac{2}{3}\rho u_{w,y} \\ f_5 = f_7 - \dfrac{1}{2}\left(f_1 - f_3\right) + \dfrac{1}{2}\rho u_{w,x} + \dfrac{1}{6}\rho u_{w,y} \\ f_6 = f_8 + \dfrac{1}{2}\left(f_1 - f_3\right) - \dfrac{1}{2}\rho u_{w,x} + \dfrac{1}{6}\rho u_{w,y} \end{cases} \tag{2.27}$$

Equation (2.27) is only viable for the bottom boundary, and similar procedures can be used to obtain the calculation equations on top, left and right boundaries. This boundary scheme is the so-called wet-node approach and is feasible on straight boundaries. This boundary scheme can be used prescribe the known velocity boundary and is also called the Zou-He boundary condition.

2.3.2. Basic Boundary Schemes for Mass Transport

Robin boundary conditions (or called third type boundary conditions), which are a weighted combination of Neumann boundary conditions and Dirichlet boundary conditions as shown in Equation (2.28), are widely applied in simulating mass transport processes governed by the convection-diffusion equation shown in Equation (2.6).

$$\alpha_1 \frac{\partial C}{\partial \mathbf{n}} + \alpha_2 C = \alpha_3, \quad 0 < t < t_s, \mathbf{x} \in \partial\Omega \tag{2.28}$$

In Equation (2.28), **n** is a unit normal vector for the boundary $\partial\Omega$ pointing outward from the solid phase to the fluid phase, coefficients α_k (k=1,2,3) should be given functions of space **x** and time t, and t_s is a pre-specified simulation time. Specifically, if $\alpha_1 = 0$ and $\alpha_2 \neq 0$, Equation (2.28) represents a Dirichlet boundary condition; if $\alpha_1 \neq 0$ and $\alpha_2 = 0$, Equation (2.28) represents a Neumann boundary condition.

For a Dirichlet boundary in mass transport, a constant wall concentration $C_w = \alpha_3/\alpha_2$ should be prescribed on the boundary. Zhang [61] proposed that the Dirichlet boundary can be implemented using an anti-bounce-back scheme shown in Equation (2.29) for a stationary boundary.

$$g_{i^*}\left(\mathbf{x}_f, t+\delta t\right) = -g_i^+\left(\mathbf{x}_f, t\right) + 2w_i C_w \tag{2.29}$$

In Equation (2.29), g_i^+ is the known post-collision distribution function at node $\mathbf{x}_f$, g_{i^*} is the unknown post-streaming distribution function in the opposite direction of g_i^+, and w_i is the weight coefficient.

For interpolation type boundary schemes, unknown post-streaming distribution functions can be calculated by interpolating known post-collision distribution functions at boundary-neighboring nodes with a series of carefully chosen interpolation coefficients [76][77]. However, interpolation-based schemes for treatment of curved boundaries destroy mass conservation near the boundary and the interpolation-free approaches in LBM for curved boundaries can improve the accuracy of the computed results [78].

When the boundary moves with a nonzero velocity $\mathbf{u}_w$, Equation (2.29) should be corrected as shown in Equation (2.30) for a Dirichlet boundary condition [61] on a moving wall.

$$g_{i^*}\left(\mathbf{x}_f, t+\delta t\right) = -g_i^+\left(\mathbf{x}_f, t\right) + 2w_i C_w \left[1 + \frac{3}{2}\frac{\left(\mathbf{e}_i \cdot \mathbf{u}_w\right)^2}{c_s^2} - \frac{1}{2}\frac{\left|\mathbf{u}_w\right|^2}{c_s^2}\right] \tag{2.30}$$

In LBM, a Neumann boundary can be transformed into a Dirichlet boundary by the finite difference method to approximate the normal derivative [61][62]. For example, the normal derivative of the concentration in a mass transport process can be approximated by the unknown wall concentration C_w at a wall node $\mathbf{x}_w$ and the known concentration C_f at a neighboring fluid node $\mathbf{x}_f$ along the normal direction, as shown in Equation (2.31).

$$D\frac{\partial C}{\partial \mathbf{n}} \approx D\frac{C_f - C_w}{\left|\mathbf{x}_f - \mathbf{x}_w\right|} \tag{2.31}$$

Note that in the right-hand side of Equation (2.31), the numerator of the finite difference approximation should always be (C_f -C_w) when considering the direction of the unit normal

vector **n**. Then the calculated wall concentration C_w will be imposed to calculate the unknown post-streaming distribution functions following exactly the Dirichlet boundary treatment by the anti-bounce-back scheme shown in Equation (2.29) and Equation (2.30).

Yoshino [64] proposed a flux boundary scheme in LBM which can be used to impose the flux boundary directly without using the finite difference nor the interpolation treatment. However, this boundary scheme was based on an assumption that mass flux of σ-species normal through the boundary is zero, and the unknown wall concentration at the boundary C_w is specified by Equation (2.32).

$$C_w = -\frac{\sum_{i(\mathbf{c}_i \cdot \mathbf{n} \le 0)} g_i \mathbf{e}_i \cdot \mathbf{n}}{\sum_{i(\mathbf{c}_i \cdot \mathbf{n} > 0)} w_i \mathbf{e}_i \cdot \mathbf{n}} \tag{2.32}$$

The calculated wall concentration C_w will be used to calculate the unknown distribution functions by $g_i = w_i C_w$ ($\mathbf{e}_i \cdot \mathbf{n} > 0$). Since this flux boundary scheme assumes that normal flux through the boundary is zero, thus it could be called a zero-flux boundary scheme. This zero-flux boundary scheme can be used to predict membrane CP under a complete rejection assumption (a 100% rejection rate).

2.3.3. Periodic and Symmetrical Boundary Conditions

The periodic boundary condition and the symmetric boundary condition can be used both in fluid dynamics LBM and in mass transport LBM.

2.3.3.1. The Periodic Boundary Condition

In a numerical simulation, if the fluid filed or the concentration field is periodically varying in space or is infinitely large in a direction, a periodic unit can be used to represent the whole domain, and periodic boundary conditions will be adopted at corresponding boundaries [71]. The Periodic boundary condition states that fluid leaving the domain on one side will,

instantaneously, re-enter at the opposite side. The periodic boundary condition can be illustrated in Figure 2.2.

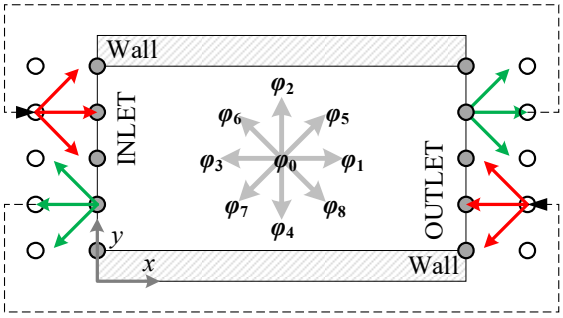

Figure 2.2 Illustration of the Periodic Boundary Condition

The periodic boundary illustrated in Figure 2.2 can be prescribed using Equation (2.33).

$$\begin{cases} \varphi_{1,5,8}(0,j) = \varphi_{1,5,8}(N_x,j) \\ \varphi_{3,6,7}(N_x+1,j) = \varphi_{3,6,7}(1,j) \end{cases} \tag{2.33}$$

In Equation (2.33), the distribution φ_i represents either f_i or g_i, and nodes at $i = 0$ or $i = N_x+1$ are solid nodes.

2.3.3.2. The Symmetrical Boundary Condition

A symmetrical boundary, where one half of the domain is the mirror image of the other, can be implemented to save computer resources. The symmetrical boundary condition can be illustrated in Figure 2.3.

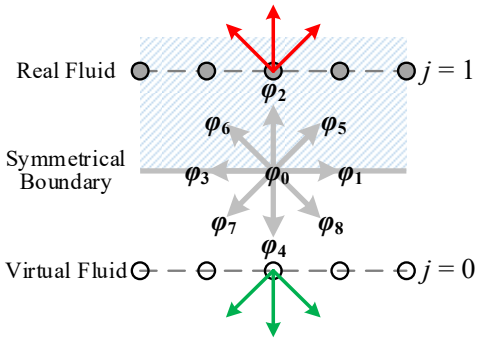

Figure 2.3 Illustration of the Symmetrical Boundary Condition

The symmetrical boundary illustrated in Figure 2.3 can be prescribed using Equation (2.34).

$$\varphi_{2,5,6}(i,1) = \varphi_{4,8,7}(i,0) \tag{2.34}$$

Distribution functions $\varphi_{4,8,7}(i,0)$ in post-streaming form in Equation (2.34) equal post-collision distribution functions on real fluid nodes $(i,1)$ in corresponding directions. A free-slip boundary condition, which enforces a zero normal fluid velocity $u_n = 0$ with a nonzero tangential fluid velocity u_t, can be implemented exactly the same way as the symmetry boundary condition.

2.4. Validation of the LBM Model

2.4.1. 2D Poiseuille Flow

Fully developed two-dimensional Poiseuille flow driven by a pressure gradient (external force) has a parabolic velocity profile as shown in Equation (2.35).

$$u_x = -\frac{1}{2\mu}\frac{\partial p}{\partial x} y\left(H - y\right) \tag{2.35}$$

In Equation (2.35), u_x is the velocity along the channel length direction ($u_y = 0$), μ is the dynamic viscosity in the bulk, and H is the channel height. The pressure gradient G is a constant relating to the channel centerline velocity u_0 by Equation (2.36) [75].

$$G = -\frac{\partial p}{\partial x} = \rho a_x = 8\rho\nu u_0 \big/ H^2 \tag{2.36}$$

In Equation (2.36), the driving acceleration a_x is in the channel length direction, the kinematic viscosity $\nu = \mu/\rho$, and the flow density ρ is a constant. The Reynolds number relates the channel centerline velocity u_0 through $\mathrm{Re} = u_0 H/\nu$. Thus, the analytical velocity profile can be obtained as shown in Equation (2.37). The pressure gradient in Equation (2.36) can be implemented in LBM following Equation (2.16).

$$u_x = -\frac{1}{2\nu\rho}\frac{\partial p}{\partial x} y\left(H - y\right) = \frac{4u_0}{H^2} y\left(H - y\right) \tag{2.37}$$

In the validation simulation, the kinematic viscosity $\nu = 1.0\times10^{-6}$ m^2/s, the channel height H = 10 m, the Reynolds number is selected to be Re = 200, the solution density $\rho = 1\times10^3$ kg/m^3.

The channel centerline velocity is calculated to be $u_0 = u_{max} = 2\times10^{-5}$ m/s using the selected Reynolds number. The no-slip bounce-back boundary scheme is used for the top boundary (y = 0) and the bottom boundary ($y = H$) of the channel flow. Analytical and LBM simulation results of the Poiseuille flow velocity profile can be seen in Figure 2.4.

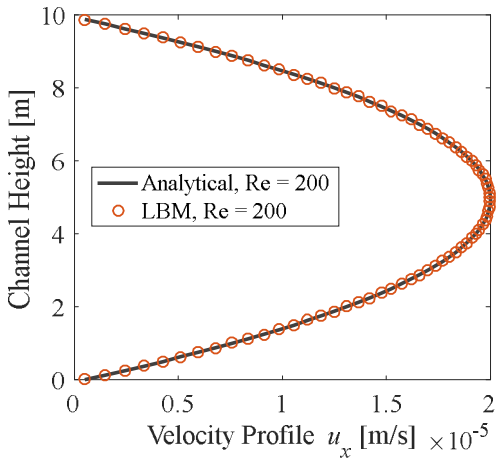

Figure 2.4 Velocity Profile of the 2D Poiseuille Flow

Figure 2.4 shows that the simulation result with LBM matches well with the analytical result. The accuracy of the LBM model is examined by the relative l^2-error norm versus the mesh size. The relative error norm in the whole computational domain is defined with Equation (2.38).

$$Er = \frac{\sqrt{\sum_{x,y}\left(u_{num} - u_{ana}\right)^2}}{\sqrt{\sum_{x,y} u_{ana}^2}} \tag{2.38}$$

The summation in Equation (2.38) covers all nodes in the simulation domain. The velocities u_{num} and u_{ana} denote the numerical value and the analytical solution, respectively. Three Reynolds numbers Re = 100, 200, 300 are selected for a better evaluation. For each Reynolds number, eight different meshes with node number in y direction NY = 10, 20, 30, …, 80 are adopted. The relative error calculation results are shown in Figure 2.5.

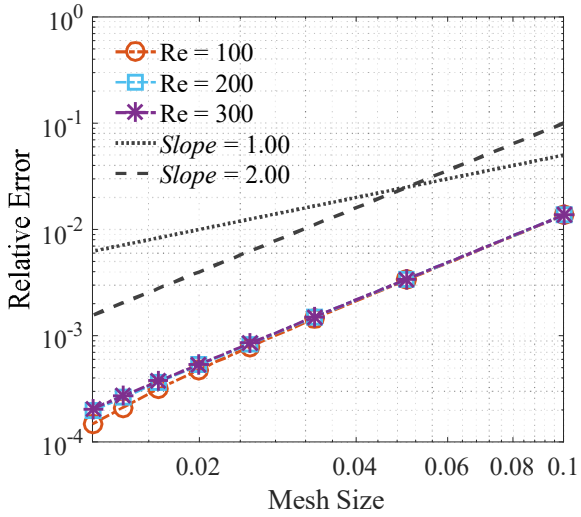

Figure 2.5 Accuracy Order of the 2D Poiseuille Flow

Figure 2.5 indicates that the developed LBM model with the bounce-back boundary scheme has a convergence order of 2.

2.4.2. 2D Thermal Poiseuille Flow

In this validation case, the two-dimensional Poiseuille flow problem with a constant wall temperature T_t is considered, as illustrated in Figure 2.6.

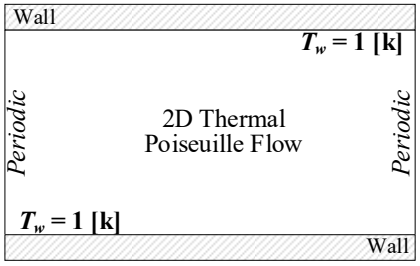

Figure 2.6 Illustration of the 2D Thermal Poiseuille Flow

For incompressible flow with a constant specific heat capacity and a constant thermal conductivity, the equation of the conservation of energy can be written in Equation (2.39).

$$\rho c_p \left[\frac{\partial T}{\partial t} + (\mathbf{u} \cdot \nabla) T \right] = k \nabla^2 T + \Phi \tag{2.39}$$

In Equation 2.39, c_p is the specific heat capacity at constant pressure, k is he thermal conductibility with a unit of W/(m·K) or kg·m/(s^{3}K) with K the temperature unit Kelvin, T is the

temperature, and Φ is the viscous heating source given in Equation (2.22). For strictly incompressible solids and liquids, the density does not depend on the temperature, and then the constant volume and constant pressure specific heat capacities are equal, $c_p = c_v$. The thermal diffusivity is defined as $\alpha = k/(\rho c_p)$ with a unit of m^2/s, and a dimensionless Prandtl number is defined as the ratio of momentum diffusivity to thermal diffusivity as $\mathrm{Pr} = \nu/\alpha = \mu c_p/k$. Thus, the temperature distribution is given in Equation (2.40) [79].

$$T(y) = T_w + \left(\frac{h^2}{2}\frac{dp}{dx}\right)^2 \frac{1}{3k\mu}\left[1-\left(\frac{y^*}{h}\right)^4\right] = T_w + \left(\frac{H^2}{8}\frac{dp}{dx}\right)^2 \frac{1}{3k\mu}\left[1-\left(\frac{2y}{H}-1\right)^4\right] \tag{2.40}$$

In Equation (2.40), $-h \le y^* \le h$, $0 \le y \le H$, $h = H/2$, and $y^* = y - H/2$. The pressure gradient in Equation (2.40) can be given by Equation (2.36) for two-dimensional Poiseuille flow. Thus, Equation (2.40) becomes Equation (2.41).

$$T(y) = T_w + \frac{\mu u_0^2}{3k}\left[1-\left(\frac{2y}{H}-1\right)^4\right] = T_w + \frac{\mathrm{Pr}^* u_0^2}{3}\left[1-\left(\frac{2y}{H}-1\right)^4\right] \tag{2.41}$$

In Equation (2.41), $\mathrm{Pr}^* = \mathrm{Pr}/c_p = \mu/k$. In the numerical simulation, two Pr* are selected as $\mathrm{Pr}^* = 0.5\times10^6$, 1.5×10^6 $K\cdot s^2/m^2$ (K is a temperature unit, Kelvin), Pr is fixed to be 0.6 from the constant viscosity $\nu = 1.0\times10^{-6}$ m^2/s and the thermal diffusivity $\alpha = 1.6667\times10^{-6}$ m^2/s (α is calculated based on the selected dimensionless relaxation time $\tau_h = 1.0$), and the calculated specific heat capacity at constant pressure $c_p = 1.2\times10^{-6}$, 1.2×10^{-6} $m^2/(K\cdot s^2)$ for $\mathrm{Pr}^* = 0.5\times10^6$, 1.5×10^6 $K\cdot s^2/m^2$, respectively. The thermal LBM model with a source term shown in Equation (2.19) is used for the simulation. Analytical and simulation results of the Poiseuille flow temperature profile can be seen in Figure 2.7, which shows that the simulation result with LBM matches well with the analytical result for both of the two selected characterizing numbers Pr*.

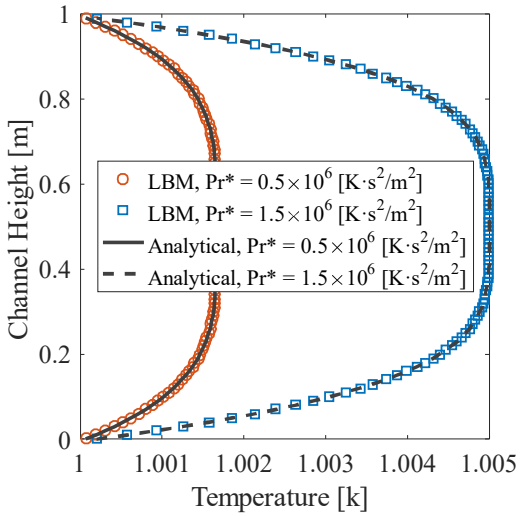

Figure 2.7 Temperature Profile of the 2D Thermal Poiseuille Flow

Thus, selected validation cases for the developed LBM model in fields of fluid dynamics and heat transfer (the mass transport problem is similar to hear transfer problem without the heating source term) show that the developed numerical model is viable for the simulation of membrane desalination processes.

2.5. Design of a Flux Boundary Scheme

Flux is an important physical variable in heat transfer and mass transport involving both convection and diffusion. A general mathematical definition of the total flux $\mathbf{J}_\sigma$ due to convection and diffusion governed by Equation (2.6) can be given by Equation (2.42). Note that flux here is by default the heat flux in heat transfer or the mass flux in mass transport, instead of the flow mass flux $\rho\mathbf{u}$ in hydrodynamics.

$$\mathbf{J}_\sigma = \mathbf{u}C - D\nabla C \tag{2.42}$$

Chai [66] proposed a numerical method to calculate boundary mass flux in the LBM framework, however, this method was not extended as a boundary scheme to prescribe boundary flux. Physically, heat and mass flux can be calculated directly through the flux definition shown

in Equation (2.42), and the gradient of the variable on boundary nodes or in interior lattice nodes can be computed by Equation (2.43) [76][80].

$$\nabla C = \frac{3}{\tau}\frac{\delta t}{(\delta h)^2}\left(\mathbf{u}C - \sum_{i=0}^{8} g_i \mathbf{e}_i\right) \tag{2.43}$$

Note that Equation (2.43) is slightly different than the form in reference [76] since the lattice speed c is included in the discrete velocity $\mathbf{e}_i$ as shown in Equation (2.10). After a rearrangement of Equation (2.43), Equation (2.44) can be obtained.

$$\left(\sum_{i=0}^{8} g_i \mathbf{e}_i\right)\cdot\mathbf{n} = \left(\mathbf{u}C - \frac{\tau}{3}\frac{\delta h^2}{\delta t}\nabla C\right)\cdot\mathbf{n} \tag{2.44}$$

The present flux boundary scheme is based on a finding that total flux normal through the boundary equals the projection of the first-order moment of distribution functions on the surface normal, and in which, the known distribution functions should be in a post-collision form while the unknown distribution functions should be in a post-streaming form, as shown in Equation (2.45).

$$\underbrace{\sum_{\mathbf{e}_i\cdot\mathbf{n}>0} g_i \mathbf{e}_i\cdot\mathbf{n}}_{\text{unkonwn}} + \underbrace{\sum_{\mathbf{e}_i\cdot\mathbf{n}\le 0} g_i^{+} \mathbf{e}_i\cdot\mathbf{n}}_{\text{konwn}} = \left(\mathbf{u}C - D\nabla C\right)\cdot\mathbf{n} = \mathbf{J}_\sigma\cdot\mathbf{n} \tag{2.45}$$

The detailed derivation of Equation (2.45) can be seen in Appendix A. In the present flux scheme, the unknown post-streaming distribution functions can be calculated from the post-collision distribution functions and the prescribed flux constraint. The calculation of the normal derivative in flux $\mathbf{J}_\sigma$ with the finite difference method or boundary-neighboring nodes interpolation treatment can be avoided. Although the derivation of Equation (2.45) in Appendix A utilizes the finite difference approximation, the implementation of this boundary scheme to calculate the unknown post-streaming distribution functions only involves boundary local nodes.

The very important step is to construct approximation equations for unknown distribution functions to close the system since Equation (2.45) only provides one equation. One approximation method for these unknown distribution functions was proposed by Yoshino [64] for a zero-flux boundary. In the present study, the same approximation method is adopted and test cases demonstrate that the approximation is still valid although the present boundary scheme removes the zero-flux assumption. On boundary nodes, unknown distribution functions are approximated by Equation (2.46) [64].

$$g_i = w_i C_w \tag{2.46}$$

The approximation equation shown in Equation (2.46) is actually the equilibrium distribution function for the concentration field shown in Equation (2.9) with the fluid velocity term eliminated. It can be demonstrated that if the concentration field equilibrium distribution functions are used directly as approximation equations without eliminating the velocity term, the final result is the same as using reduced approximation equations shown in Equation (2.46). Another approximation method to close the system was proposed by Kang in [81][82][83], which stated that the non-equilibrium portion of the distribution functions on the boundary are equal in magnitude but take on opposite signs in reverse directions, as shown in Equation (2.47).

$$g_{i*}^{\text{neq}} = -g_i^{\text{neq}} \tag{2.47}$$

In Equation (2.47), subscripts i and i* are used to denote distribution functions in opposite directions, i.e. $\mathbf{e}_{i*} = -\mathbf{e}_i$. The proposed flux boundary scheme is explained using a straight top boundary illustrated in Figure 2.8.

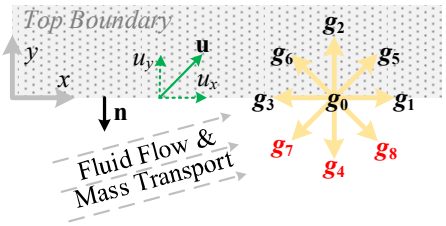

Figure 2.8 Simplified Illustration of a Straight Top Boundary

The projection of the first-order moment of distribution functions on the boundary normal **n** can be calculated following Equation (2.45) and shown in Equation (2.48).

$$\underbrace{-c\left(g_2^+ + g_5^+ + g_6^+\right)}_{\mathbf{c}_i\cdot\mathbf{n}\le 0} + \underbrace{c\left(g_4 + g_7 + g_8\right)}_{\mathbf{c}_i\cdot\mathbf{n}>0} = -J_y \tag{2.48}$$

In Equation (2.48), c is the lattice speed which is unity, J_y is the flux magnitude through the top boundary. Substitute the approximate equations for g_4, g_7 and g_8 in Equation (2.46) into Equation (2.48), the wall concentration C_w can then be calculated, as shown in Equation (2.49).

$$C_w = \frac{-J_y + c\left(g_2^+ + g_5^+ + g_6^+\right)}{c\left(w_4 + w_7 + w_8\right)} \tag{2.49}$$

The unknown post-streaming distribution functions g_4, g_7 and g_8 can be calculated by the approximation equation in Equation (2.46) and the calculated wall concentration C_w in Equation (2.49). From Equation (2.45) and as discussed in Appendix A, the generalized calculation method for the wall concentration C_w can be given by Equation (2.50).

$$C_w = \frac{\mathbf{J}\cdot\mathbf{n} - \sum_{\mathbf{e}_i\cdot\mathbf{n}\le 0} g_i^+ \mathbf{e}_i\cdot\mathbf{n}}{\sum_{\mathbf{e}_i\cdot\mathbf{n}>0} w_i \mathbf{e}_i\cdot\mathbf{n}} = \frac{\left(\mathbf{u}C - D\nabla C\right)\cdot\mathbf{n} - \sum_{\mathbf{e}_i\cdot\mathbf{n}\le 0} g_i^+ \mathbf{e}_i\cdot\mathbf{n}}{\sum_{\mathbf{e}_i\cdot\mathbf{n}>0} w_i \mathbf{e}_i\cdot\mathbf{n}} \tag{2.50}$$

If the approximation of unknown distribution functions adopts Equation (2.47), and combining Equation (2.47) with local equilibrium distribution functions in Equation (2.9) yields Equation (2.51).

$$
\begin{aligned}
g_2^+ + g_4 &= g_2^{\mathrm{eq}} + g_4^{\mathrm{eq}} = 2w_2C_w = 2w_4C_w \\
g_5^+ + g_7 &= g_5^{\mathrm{eq}} + g_7^{\mathrm{eq}} = 2w_5C_w = 2w_7C_w \\
g_6^+ + g_8 &= g_6^{\mathrm{eq}} + g_8^{\mathrm{eq}} = 2w_6C_w = 2w_8C_w
\end{aligned} \tag{2.51}
$$

Substitute the approximate equations for g_4, g_7 and g_8 in Equation (2.51) into Equation (2.48), the wall concentration C_w can be calculated, as shown in Equation (2.52).

$$
C_w = \frac{-\frac{1}{2}J_y + c\left(g_2^+ + g_5^+ + g_6^+\right)}{c\left(w_4 + w_7 + w_8\right)} \tag{2.52}
$$

The unknown post-streaming distribution functions g_4, g_7 and g_8 should be calculated by the approximation equation in Equation (2.51) and the calculated wall concentration C_w in Equation (2.52). Then the generalized calculation method for the wall concentration C_w should be given by Equation (2.53).

$$
C_w = \frac{\frac{1}{2}\mathbf{J}\cdot\mathbf{n} - \sum_{\mathbf{e}_i\cdot\mathbf{n}\le 0} g_i^+ \mathbf{e}_i\cdot\mathbf{n}}{\sum_{\mathbf{e}_i\cdot\mathbf{n}>0} w_i\mathbf{e}_i\cdot\mathbf{n}} = \frac{\frac{1}{2}\left(\mathbf{u}C - D\nabla C\right)\cdot\mathbf{n} - \sum_{\mathbf{e}_i\cdot\mathbf{n}\le 0} g_i^+ \mathbf{e}_i\cdot\mathbf{n}}{\sum_{\mathbf{e}_i\cdot\mathbf{n}>0} w_i\mathbf{e}_i\cdot\mathbf{n}} \tag{2.53}
$$

Note that each approximation method has a specific generalized form of the wall concentration C_w, and unknown post-collision distribution functions should be calculated through C_w and the corresponding approximation approach in Equation (2.46) or in Equation (2.47). In most cases, the two approximation methods expressed by Equation (2.46) or Equation (2.47) provide identical results. In this study, the first approximation method expressed by Equation (2.46) is adopted in validation and application cases.

The calculation of the wall concentration by Equation (2.50), and then the calculation of the unknown distribution functions based on the approximation equations following Equation (2.46), show that the present boundary scheme only involves boundary local nodes. Such a local boundary scheme is desirable in simulating transport processes in complex geometries, such as in porous media.

2.6. Validation of the Flux Boundary Scheme

Cases with different types of flux boundary conditions are investigated to validate the present flux boundary scheme. These flux boundary conditions cover the general Neumann boundary (for the diffusive flux boundary), the zero normal derivative Neumann boundary (for the convective flux boundary), and the total flux boundary (for the convective plus diffusive flux boundary).

2.6.1. The Neumann Boundary

The Neumann boundary is usually used to prescribe the normal derivative of a variable on the boundary. A pure mass diffusion problem is invested with top and bottom boundary conditions expressed in Equation (2.54). The rectangular simulation domain $L \times H$ is prescribed with a Dirichlet boundary at bottom ($y = 0$) and a Neumann boundary at top ($y = H$). Both the left boundary ($x = 0$) and the right boundary ($x = L$) are periodic boundaries. Since it is a pure diffusion problem, there is no fluid flow through the simulation domain, i.e. $\mathbf{u} = 0$ in Equation (2.45). Also, from Equation (2.54), the concentration derivative normal to the top boundary ($y = H$) varies sinusoidally along the horizontal x direction.

$$\begin{cases} C(x,y)\big|_{y=0} = C_0 \text{ (Dirichlet boundary)} \\ \left(\dfrac{\partial C(x,y)}{\partial y}\right)\Big|_{y=H} = C_s = |C_s|\sin(\beta x) \text{ (Neumann boundary)} \end{cases} \tag{2.54}$$

In Equation (2.54), the wave number $\beta = \pi/24$ for convenience. The system is analytically solvable and the exact solution of this problem is shown in Equation (2.55) [62].

$$C(x,y) = C_0 + \frac{|C_s|\sin(\beta x)}{\beta}\frac{\sinh(\beta y)}{\cosh(\beta H)} \tag{2.55}$$

The height of the simulation domain $H = 20$, and the length of the simulation domain $L = 48$. The Dirichlet boundary condition is applied on bottom (y = 0) according to Equation (2.29) with

selected concentrations $C_0 = 1$ and $C_s = 0.01$ [62]. All simulation parameters are in lattice units (dimensionless), and conversion procedures between physical units and LBM units are shown in Appendix B. When the developed flux boundary scheme in Equation (2.50) is applied on the top Neumann boundary, the calculated wall concentration can be shown in Equation (2.56).

$$C_w = \frac{\left(\mathbf{u}C - D\nabla C\right)\cdot\mathbf{n} - \sum_{\mathbf{e}_i\cdot\mathbf{n}\le 0} g_i^+ \mathbf{e}_i\cdot\mathbf{n}}{\sum_{\mathbf{e}_i\cdot\mathbf{n}>0} w_i \mathbf{e}_i\cdot\mathbf{n}} = \frac{D\left|C_s\right|\sin\left(\beta x\right) + c\left(g_2^+ + g_5^+ + g_6^+\right)}{c\left(w_4 + w_7 + w_8\right)} \quad (2.56)$$

The simulation result can be expressed by the concentration distribution at 5 different horizontal positions ($x = 1/4L$, $3/8L$, $1/2L$, $5/8L$, $3/4L$) from the bottom wall to the top wall. Figure 2.9 shows simulation results using different boundary schemes, which indicates that the predicted concentration distribution using the present flux boundary scheme is identical to the result using the finite difference scheme, and both results match well with the analytical solution.

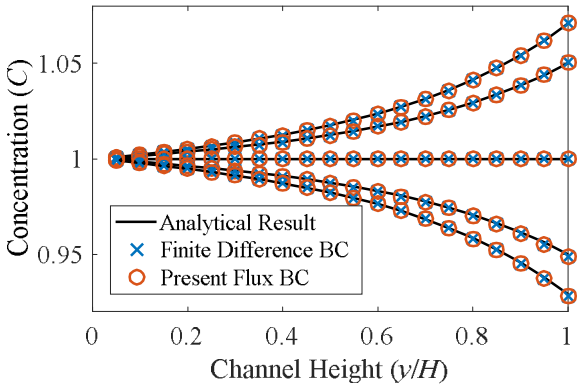

Figure 2.9 Concentration Distribution in the Pure Diffusion Process

Besides the above pure diffusion case, a convection-diffusion process is tested for further validation. The fluid flow is added for the convection-diffusion transport with a Reynolds number Re = 10 and a Peclet number Pe = 10. For the flow field, a pressure-driven Poiseuille flow is assumed for the x direction (horizontal direction) velocity with a maximum centerline velocity $u_{max} = 0.0833$ in a lattice unit. The bottom boundary ($y = 0$) is a no-slip boundary and the top boundary is a velocity boundary with $u_x = 0$ and $u_y = 0.001$ in a lattice unit. The adoption

of the velocity boundary u_y on the top boundary is intended to generate mass convection through the boundary. For the concentration field, all parameters and boundary conditions stay the same as in the pure diffusion case. Thus, the top boundary ($y = H$) of the concentration field is a mass flux boundary involving both convection and diffusion. The left boundary ($x = 0$) and the right boundary ($x = L$) are periodic boundaries for both flow field and concentration field.

Concentration distributions at 5 different horizontal positions ($x = 1/4L$, $3/8L$, $1/2L$, $5/8L$, $3/4L$) from the bottom wall to the top wall with the finite difference scheme and the present flux scheme can be seen in Figure 2.10.

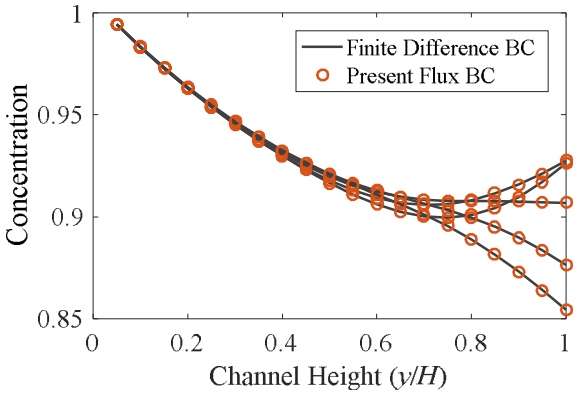

Figure 2.10 Concentration Distribution in the Convection-Diffusion Process

Results in Figure 2.10 show that the present boundary scheme matches with the finite different scheme, and the total concentration in the simulation domain is reduced due to mass convection through the top boundary. However, at the top boundary, the concentration gradients at different horizontal positions are the same as the pure diffusion case because of the same constraint of the Neumann boundary shown in Equation (2.54).

2.6.2. The Robin Boundary

The Robin boundary is a weighted combination of the Dirichlet boundary and the Neumann boundary, which can be used to prescribe the total flux boundary composed of convection flux and diffusion flux. This validation case focuses on a time-dependent convection-diffusion

problem in a two-dimensional domain $L \times H$ with constant mass flux as the input from the inlet ($x = 0$). For the concentration field, the detailed initial and boundary conditions can be described using Equation (2.57). For the flow field, the inlet ($x = 0$) is a velocity boundary. The bottom boundary ($y = 0$) and the top boundary ($y = H$) of the simulation domain are symmetric boundaries for the flow field and the concentration field.

$$\begin{cases} C(x,t)\big|_{t=0} = 0, 0 < x < L \left(\text{Initial condition}\right) \\ \left(\mathbf{u}C - D\partial C/\partial \mathbf{n}\right)\big|_{x=0} = \mathbf{u}C_f, t > 0 \left(\text{Total flux boundary}\right) \\ \left(\partial C/\partial \mathbf{n}\right)\big|_{x=L} = 0, t > 0 \left(\text{Zero normal derivative Neumann boundary}\right) \end{cases} \tag{2.57}$$

In Equation (2.57), $D = 0.01$ m^2/s, $C_f = 50$ mol/m^3, and $L = 1$ m. The non-dimensional Peclet number $\mathrm{Pe} = u_x L/D = 1$. The inlet velocity u_x can be calculated using the Peclet number. The Neumann boundary defined in Equation (2.57) at the outlet ($x = L$) indicates that there is no diffusion flux through this boundary. When t is sufficiently small, the above problem has an asymptotic solution shown in Equation (2.58) [76].

$$C(x,t) = C_f \left(\begin{array}{l} \dfrac{1}{2}\mathrm{erfc}\left(\dfrac{x-u_x t}{2\sqrt{Dt}}\right) + \sqrt{\dfrac{u^2 t}{\pi D}}\exp\left(-\dfrac{\left(x-u_x t\right)^2}{4Dt}\right)\cdots \\ \cdots - \dfrac{1}{2}\left(1 + \dfrac{u_x x}{D} + \dfrac{u_x^2 t}{D}\right)\exp\left(\dfrac{u_x x}{D}\right)\mathrm{erfc}\left(\dfrac{x+u_x t}{2\sqrt{Dt}}\right) \end{array} \right) \tag{2.58}$$

In Equation (2.58), *exp* is the exponential function and *erfc* is the complementary error function. The present flux boundary scheme Equation (2.45) is used to prescribe the Robin boundary at the inlet ($x = 0$) and the Neumann boundary at the outlet ($x = L$). The simulation results of concentration distribution with the present flux boundary scheme matches well with the analytical asymptotic solution at different time spots, as seen in Figure 2.11. These results show that the concentration on the left inlet boundary increases with time, and it is foreseeable

that the concentration in the whole domain will finally reach C_f if the simulation time is long enough.

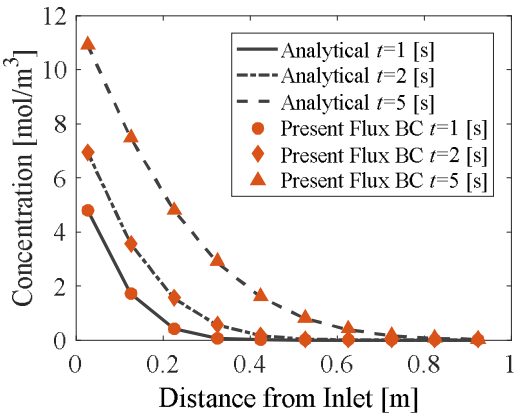

Figure 2.11 Transient Concentration in Different Simulation Durations

The accuracy of the boundary scheme is examined by the relative l^2-error norm versus the mesh size. The relative error norm in the whole computational domain is defined with Equation (2.59).

$$Er = \frac{\sqrt{\sum_{x,y}\left(C_{num} - C_{ana}\right)^2}}{\sqrt{\sum_{x,y} C_{ana}^2}} \tag{2.59}$$

The summation in Equation (2.59) covers all nodes in the simulation domain. Concentrations C_{num} and C_{ana} denote the numerical value and the analytical solution, respectively. The simulation time t = 5s, and four different concentration relaxation times τ_s = 0.05, 0.8, 1.0, 2.0 are selected for a better evaluation. For each relaxation time, eight different meshes are adopted with the node number in x direction NX = 10, 20, 30, …, 80. The relative error calculation results are shown in Figure 2.12, which indicates that the new flux boundary scheme has a convergence order of 1.

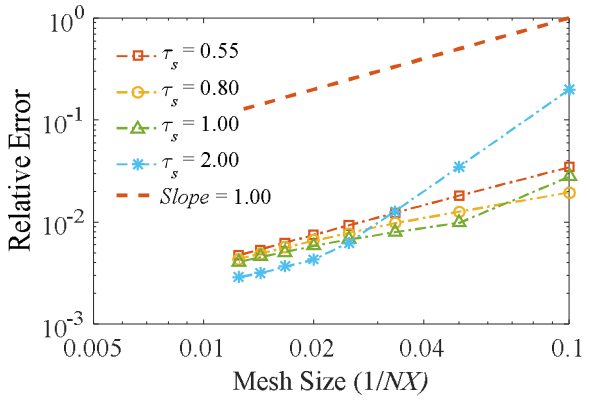

Figure 2.12 Relative Error Versus Mesh Size in the Robin Boundary Case

The convergence order evaluation result is within expectation since the approximation equation shown in Equation (2.46) for the unknown distribution functions is first order. A higher convergence order, if desirable, may be achieved with a higher order approximation algorithm as a replacement of Equation (2.46).

2.6.3. The Reaction Boundary

To further validate the proposed flux boundary scheme, a reaction boundary in a rectangular domain with the length and the height as $L \times H$ is selected and for which there exists an analytic solution. Refer to Figure 2.13 and Equation (2.60), the reaction takes place at the top boundary ($y = H$) with first-order linear kinetics, which is actually a Newman boundary. At the bottom boundary ($y = 0$) and the right boundary ($x = L$), zero concentration gradient normal to the boundary is specified. Solute is allowed to diffuse into the domain from the left boundary ($x = 0$), thus there should be a Dirichlet boundary condition ($C = C_0$) specified there.

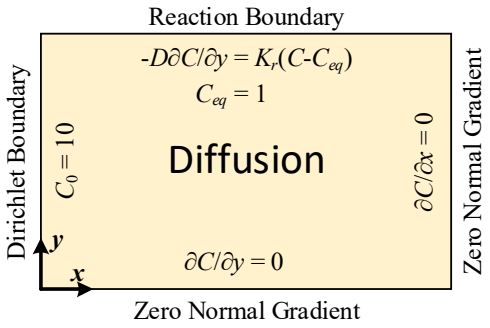

Figure 2.13 Illustration of Boundary Conditions in the Reaction Boundary Case

$$\begin{cases} C(0,y) = C_0;\ \left.\dfrac{\partial C}{\partial x}\right|_{x=L} = 0;\ \left.\dfrac{\partial C}{\partial y}\right|_{y=0} = 0 \\ -D\left.\dfrac{\partial C}{\partial y}\right|_{y=H} = k_r\left(C\big|_{y=H} - C_{eq}\right) \end{cases} \tag{2.60}$$

In Equation (2.60), the reaction rate $k_r = 0.1$, the diffusion coefficient $D = 1/6$, the equilibrium concentration $C_{eq} = 1$, the inlet concentration $C_0 = 10$, the length of the simulation domain $L = 100$, and the height of the simulation domain $H = 80$ (all parameters are in lattice unit). The analytical solution for $C(x,y)$ can be obtained by separation of variables, as shown in Equation (2.61) [82].

$$\begin{cases} C(x,y) = C_{eq} + \left(C_0 - C_{eq}\right)\sum_{n=1}^{\infty} \dfrac{\sin\left(\beta_n H\right)}{N_n^2 \beta_n} \dfrac{\cosh\left[\beta_n\left(x-L\right)\right]}{\cosh\left(\beta_n L\right)} \cos\left(\beta_n y\right) \\ N_n^2 = \dfrac{H}{2}\left(1 + \dfrac{\sin\left(2\beta_n H\right)}{2\beta_n H}\right) \end{cases} \tag{2.61}$$

The variable β_n in Equation (2.61) can be determined from the transcendental equation in Equation (2.62).

$$\left(\beta_n H\right)\tan\left(\beta_n H\right) = \frac{k_r H}{D} \tag{2.62}$$

The left Dirichlet boundary is prescribed using Equation (2.29), the right and the bottom zero normal gradient boundaries are prescribed using the present boundary scheme in Equation

(2.45). Two boundary schemes are used on the top reaction boundary for a comparison purpose, which are Kang's (improved) reaction boundary scheme [83] and the present flux boundary scheme Equation (2.45). The analytical result as well as the simulation result for the solute concentration at steady state are shown in Figure 2.14.

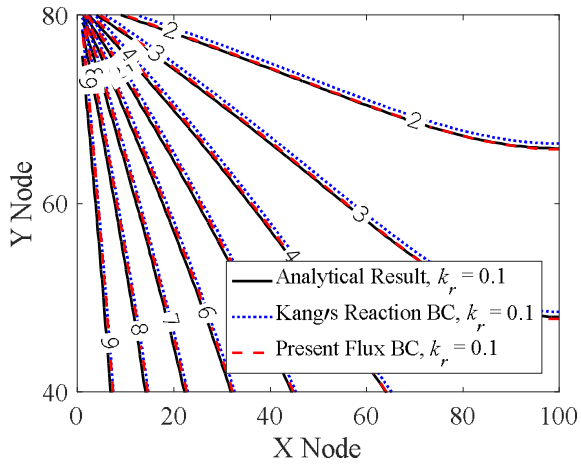

Figure 2.14 Steady State Concentration Contours in the Reaction Boundary Case

Figure 2.14 shows that near the top reaction boundary, simulation result by the present flux boundary scheme matches better with the analytical result.

The accuracy of the boundary scheme for the reaction boundary is examined by the relative l^2-error norm versus the mesh size following Equation (2.63).

$$Er = \frac{\sqrt{\sum_{x,y}\left(C_{num} - C_{ana}\right)^2}}{\sqrt{\sum_{x,y} C_{ana}^2}} \tag{2.63}$$

Two reaction rates are selected as k_r = 0.1, 0.01. For each reaction rate, seven different mesh plans with node number in y direction NY = 40, 60, 80, 100, 120, 140, 160 are adopted. The relative error calculation results are shown in Figure 2.15.

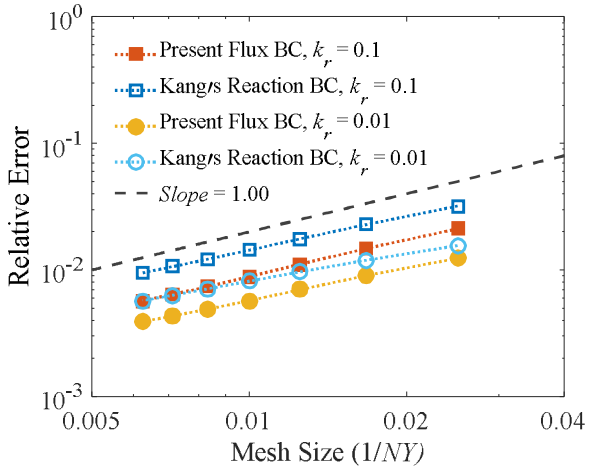

Figure 2.15 Relative Error Versus Mesh Size in the Reaction Boundary Case

Figure 2.15 shows that although both Kang's reaction boundary scheme [83] and the present flux boundary scheme have an accuracy order of 1, the present flux boundary scheme has lower relative error for both of the reaction rates.

3. PREDICTION OF THE CONCENTRATION POLARIZATION*

This section covers the application of the developed LBM model in the CP study. First, the setup of the simulation model and its boundary conditions are introduced. Then viable treatment to deal with the large Peclet number problem existing in seawater desalination is discussed and adopted to improve the numerical stability of the LBM model. Thereafter, CP and permeate flux in a plain channel are predicted and compared with a finite element method (FEM) benchmark with a complete membrane rejection assumption. Then CP and permeate flux are studies with different membrane rejection rates. Finally, CP and permeate flux in a spacer filled desalination channel are predicted with the LBM model.

3.1. Model Setup and Boundary Conditions

3.1.1. Simulation Model Setup

A benchmark model is selected for the verification of the CP prediction model. Song [21] developed a finite element model for the CP prediction, in which both fluid dynamics and mass transport can be simultaneously solved either in a plain channel and in a spacer filled channel. In this study, the simulation domain covers the initial 1 cm length upstream of the desalination channel, since CP develops faster at this initial length and then increases very slowly along the extra channel length. The height (in y direction) of the desalination channel H_c = 1 mm and the length (in x direction) of the channel L_c = 1 cm. The width (in z direction) of the channel is

*Part of this section is reprinted with permission from "Numerical Modeling of Concentration Polarization and Inorganic Fouling Growth in the Pressure-Driven Membrane Filtration Process" by Wende Li, et al., 2019. Journal of Membrane Science, 569, 71-82 (https://doi.org/10.1016/j.memsci.2018.10.007), Copyright [2019] by Elsevier.

assumed to be sufficiently large in spanwise direction, thus a two-dimensional simulation domain is targeted to represent the desalination channel.

3.1.2. Boundary Conditions in CP Prediction

The geometry of the spacer filled feed channel in the pressure-driven membrane desalination process and applied boundary conditions are illustrated in Figure 3.1. Boundary schemes in LBM for the fluid dynamics and the mass transport are applied separately. The distribution functions φ_i in Figure 3.1 denotes f_i for the fluid field or g_i for the concentration field.

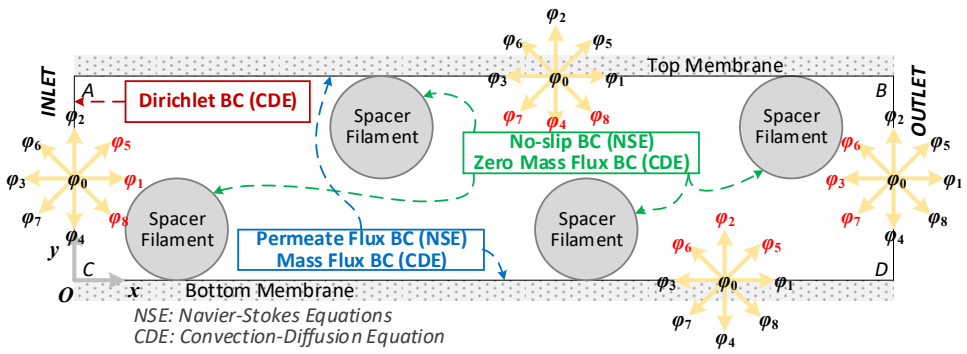

Figure 3.1 Illustration of Boundary Conditions for a Desalination Channel

3.1.2.1. Hydrodynamics Boundary Conditions

The known velocity boundary condition is applied for the bottom boundary and the top membrane boundary by the Zou-He boundary scheme [75] to prescribe the permeate flux normal through the membranes. The tangential velocity on the bottom and top boundaries is set to be zero to meet the no-slip condition. The bounce-back scheme is used to prescribe the no-slip boundary condition at the circumference of the spacer filaments. Following the bounce-back scheme, the unknown populations in post-streaming form on boundaries can be calculated through Equation (2.23).

3.1.2.2. Mass Transport Boundary Conditions

In solving the convection-diffusion equation, a zero-flux boundary scheme will be used at the membrane boundary (if in a full membrane rejection condition) and around the feed spacer

filaments. Yoshino zero-flux boundary scheme [64] comprising a wall concentration C_w calculation equation shown in Equation (2.32) and approximation equations for unknown post-streaming distributions functions is suitable to prescribe zero-flux boundaries in the desalination channel illustrated in Figure 3.1. Also, in mass transport problems governed by the convection-diffusion equation shown in Equation (2.6), the mass particles bounce-back boundary [84] resembling the non-slip bounce-back boundary in hydrodynamics shown in Equation (2.23) can also be used prescribe the zero-flux boundary.

The membrane mass rejection rate is defined as R_{ej} = (conductivity of feed-conductivity of permeate)/(conductivity of feed)×100% = (1-C_p/C_0)×100%, and in which C_p is the permeate water concentration, and C_0 is the feed water concentration. For a complete rejection membrane, the rejection rate R_{ej} = 100% since the permeate flux salinity C_p = 0. Usually the permeate flux (volumetric flux, with a unit of $m \cdot s^{-1}$) through the membrane can be measured, and salt ion mass flux (rate of mass flow per unit area, with a unit of $kg \cdot s^{-1} \cdot m^{-2}$) through the membrane can be treated as a convection process. This is because the RO membrane is very thin, and if the mass flux is assumed a constant through the membrane, there should be no accumulation of salts ions within the membrane. This assumption indicates a constant salt concentration and a negligible concentration gradient in the membrane. Thereafter, the mass diffusion process is ignored (the concentration gradient is negligible) and only the mass convection process is considered.

Thus, referring to the flux boundary scheme proposed in Equation (2.46) and Equation (2.50), the mass flux boundary scheme incorporating the rejection rate can be designed and shown in Equation (3.1).

$$\begin{cases} C_w = \dfrac{\left[\mathbf{u}C\left(1\text{-}R_{ej}\right)\right]\cdot\mathbf{n} - \sum_{\mathbf{e}_i\cdot\mathbf{n}\le 0} g_i^{+}\mathbf{e}_i\cdot\mathbf{n}}{\sum_{\mathbf{e}_i\cdot\mathbf{n}>0} w_i\mathbf{e}_i\cdot\mathbf{n}} \\ g_i = w_i C_w \quad \left(\mathbf{e}_i\cdot\mathbf{n}>0\right) \end{cases} \tag{3.1}$$

3.2. Treatment of the Large Peclet Number

In many mass transport cases, small particles such as ions in dilute solution have a very small diffusion coefficient. For example, the self-diffusion coefficients of the five major ions in seawater at 25 °C are all in the order of 1×10^{-9} m^2/s [85]. Following the conversion procedures shown in Appendix B between lattice units and physical units, the solute relaxation time can be calculated by Equation (3.2).

$$D_{LBM} = \left(\tau_s - 1/2\right)c^2\delta t/3 \xrightarrow{c=1,\delta t=1} \tau_s = 3D_{LBM} + 1/2 \tag{3.2}$$

The diffusion coefficient D_{LBM} with a lattice unit in Equation (3.2) can be calculated from the diffusion coefficient $D_{PHY} = 1.5\times10^{-9}$ m^2/s with a physical unit. Then the calculated relaxation time $\tau_s = 0.5008$, which is actually near the instability value of 0.5 in LBM [61]. Sometimes, in a coupled simulation of Navier-Stokes equations and the convection-diffusion equation, the correlation between the fluid field relaxation time τ and the concentration field relaxation time τ_s should be strictly controlled to accurately represent the ratio of convective mass transport to diffusive mass transport. The Peclet number can be defined to be the ratio of advection by the flow for a physical quantity to the rate of diffusion by an appropriate gradient, as shown in Equation (3.3).

$$\mathrm{Pe} = \frac{Lu}{D} = \frac{Lu}{\nu}\cdot\frac{\nu}{D} = \mathrm{Re}\cdot\mathrm{Sc} \tag{3.3}$$

In Equation (3.3), L is the characteristic length, u the local flow velocity, D the mass diffusion coefficient, ν is the kinematic viscosity, and Sc is the Schmidt number. Take seawater for example, the kinematic viscosity $\nu = 1\times10^{-6}$ m^2/s, and the calculated Schmidt number Sc ≈ 667. From Equation (3.3), for a channel flow with Re = 100, the calculated Peclet number Pe ≈ 66700. In a mass transport process with such a large Peclet number, the mass diffusion can actually be ignored in the desalination channel bulk flow since mass convection is dominant.

However, in other cases, such as mass transport in membrane filtration, although bulk flow mass transport is convection dominant, near-membrane mass transport is not necessarily convection dominant. Mass diffusion plays an important role near the boundary layer since permeate flow induced convection is comparable with the concentration gradient induced back diffusion near the membrane surface. Thus, the simulation of such a complex convection-diffusion process is challenging with a regular LBM routine.

Perko developed an effective lattice Boltzmann scheme to deal with the instability problem featuring large diffusion-coefficient heterogeneities and high-advection [86] in convection diffusion processes. The basic idea is to divide the physical diffusion coefficient into a reference value D_{ref}, which is constant over the entire domain, and a fluctuating residue value D_{res}, which represents a deviation from the reference, as $D = D_{ref} + D_{res}$. Then, the fluctuating residue diffusion part is transferred to an advection term by introducing a diffusion velocity $\mathbf{u}_d$, as shown in Equation (3.4).

$$\mathbf{J} = \mathbf{u}C - \left(D_{ref} + D_{res}\right)\nabla C = -D_{ref}\nabla C + \left(\mathbf{u} + \mathbf{u}_d\right)C \tag{3.4}$$

In Equation (3.4), the diffusion velocity can be calculated by Equation (3.5). Note that all variables in Equation (3.5) should be in lattice unit.

$$\mathbf{u}_d = \frac{\dfrac{D_{res}}{\tau_s c_s^2}}{\left(1 + \dfrac{D_{res}}{\tau_s c_s^2}\right)}\left(\frac{\sum_i \mathbf{e}_i g_i}{C} - \mathbf{u}\right) \tag{3.5}$$

For a transport process with a very small diffusion coefficient and a very large Peclet number, such as in seawater desalination, the reference diffusion coefficient can be selected to be a large value for a better numerical stability, and then the calculated residue fluctuating diffusion part should be negative. A validation case is adopted to investigate the feasibility of the present

boundary scheme in the application of the Peclet number transport process following the treatment proposed by Perko [86].

A validation case focusing on a pure mass diffusion process in a simulation domain comprised of three regions is selected, as seen in Figure 3.2. The first and last 2 cm regions have a small diffusion coefficient $D_{low} = 1\times10^{-11}$ m^2/s, while the middle 0.06 m region has a much larger diffusion coefficient $D_{high} = 2000D_{low}$. The reference diffusion coefficient is selected to be D_{low} for the whole domain. The initial concentration $C(x,t_0) = 0.1$ mol/m^3. The left boundary of the simulation domain is prescribed with a constant concentration as a Dirichlet boundary, and the right boundary is a zero diffusive flux Neumann boundary (zero gradient normal to the boundary). Symmetric boundaries are assumed on the top boundary and the bottom boundary. Simulation time is selected to be 500 days. A numerical solution was obtained in reference [86] using commercial FEM-based COMSOL Multiphysics software.

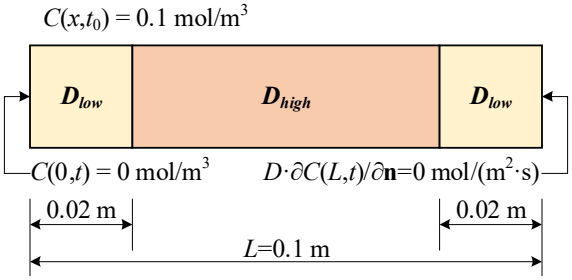

Figure 3.2 Pure Diffusion with Spatially Variable Diffusion Coefficients

Simulation results of the present flux boundary scheme, as well as the finite difference boundary scheme are compared with the reference solution, as shown in Figure 3.3.

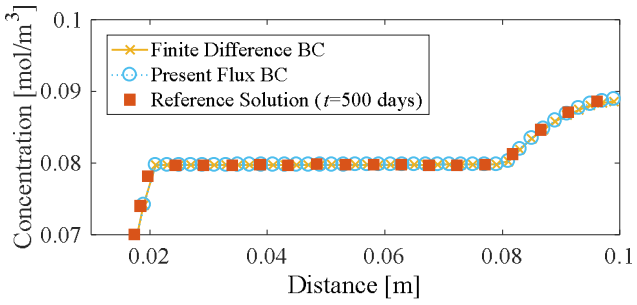

Figure 3.3 Concentration in the Diffusion-Coefficient Heterogeneity Case

Well match of results shown in Figure 3.3 from different numerical methods and boundary schemes demonstrate the feasibility of the present flux boundary scheme in the simulation of large Peclet number convection-diffusion process.

3.3. CP Prediction in a Plain Channel

Pressure-driven RO seawater desalination is a convection dominant large Peclet number process since the diffusion coefficient of salt ions in the feed flow is very small (in an order of 10^{-9} m^2/s). Treatment for the numerical instability problem due to a large Peclet number discussed in Section 3.2 is used to improve the numerical stability.

The transmembrane permeate flux will be calculated in each time step and then be prescribed on membrane boundaries of the desalination channel. The permeate flux $v_w = P_{er} \cdot (\Delta p - \Delta\pi)$, as given by reference [87], in which $P_{er} = 7.3\times10^{-12}$ m/(s·Pa) is a permeability constant of the RO membrane, $\Delta p = 5.5\times10^{6}$ Pa is the transmembrane pressure, and $\Delta\pi$ is the osmotic pressure between the feed side and the permeate side of the RO membrane. The concentration of the feed seawater C_0 = 32,000 mg/L, the diffusion coefficient of salt ions in the feed seawater $D = 1.5\times10^{-9}$ m^2/s. The flow in the desalination channel (with or without spacers) is driven by a pressure gradient ($G=-\partial p/\partial x$, in a unit of N/m^3), which can be achieved by adding a body force density term in LBM shown in Equation (2.16) following Guo's force term implementation method [72]. The pressure gradient for the feed flow in the desalination channel $\partial p/\partial x$ = -800 Pa/m.

First, the zero-flux boundary by the proposed flux boundary scheme is prescribed on membrane boundaries located at top and bottom of a plain desalination channel, which means there is no mass flux through the membrane and all salt ions are rejected by the membrane. The bounce-back scheme in LBM is used to prescribe the zero-flux boundary for a comparison

purpose. Simulation results of CP and permeate flux, as well as the FEM benchmark by Song [21], are shown in Figure 3.4.

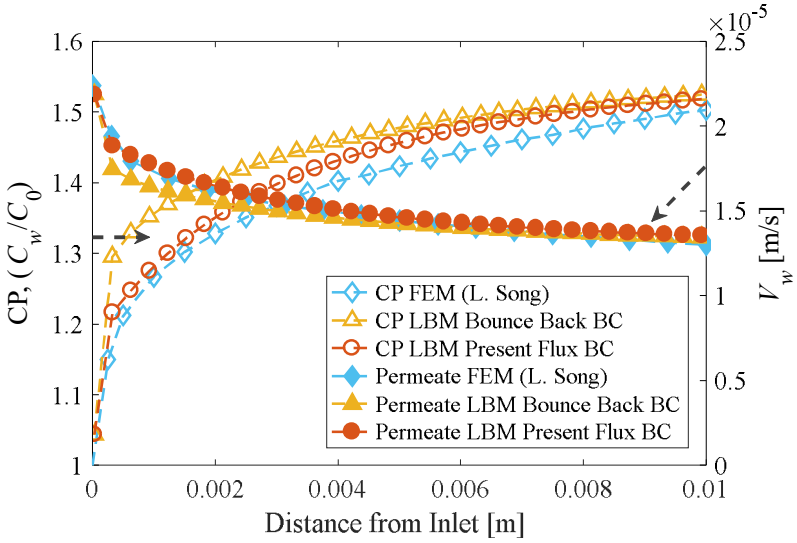

Figure 3.4 CP and Permeate Flux in a Plain Channel

Figure 3.4 shows that results from the proposed flux boundary scheme match better with published FEM benchmark results than the bounce-back scheme especially at the vicinity of the inlet. For the bounce-back scheme, the post-streaming distribution functions are calculated using the post-collision distribution functions in the collinear opposite directions only (along the link direction). This means all mass particles are bounced back without any slip at the membrane boundary. However, the no-slip constraint is released in the present flux boundary scheme, in which the post-collision distribution functions in multiple non-collinear directions are accounted to calculate the post-streaming distribution functions. Since the no-slip constraint of the bounce-back boundary scheme delays the relative transverse motion between mass particles and boundaries, the predicted CP near the inlet is higher than that using the present flux boundary scheme. While far from the inlet and near the steady state CP region, the difference vanishes for the two schemes. This can explain the better match of the simulation results with the present flux boundary scheme near the inlet region shown in Figure 3.4.

To check whether CP and permeate flux reach steady state, simulations with different durations (2s, 4s, and 8s) are performed, and results shown in Figure 3.5 demonstrate that the settling time for CP and permeate flux is less than 2s.

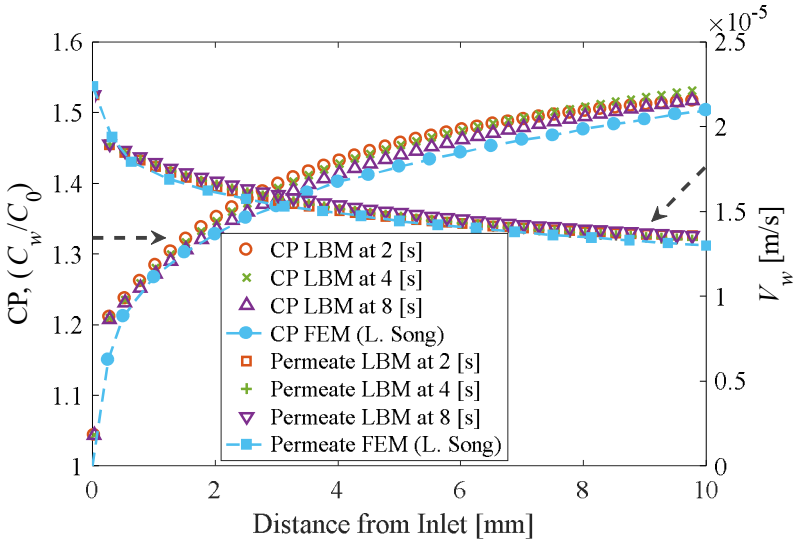

Figure 3.5 CP in a Plain Channel in Different Simulation Durations

The CP development in feed flow with different Reynolds numbers can be seen in Figure 3.6. In Figure 3.6, reduced CP and increased permeate flux can be observed for feed flow with higher Reynolds numbers. This is because in feed flow with higher Reynolds numbers, the back-diffusion process tends to be promoted thus the solute accumulation near the membrane surface is reduced.

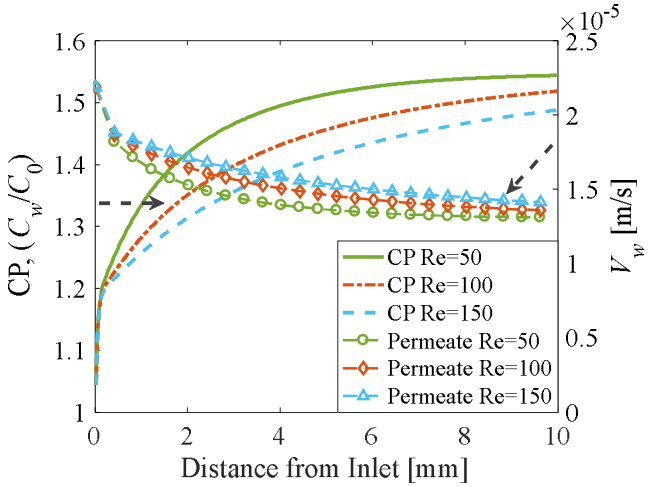

Figure 3.6 CP in a Plain Channel with Different Reynolds Numbers

The thicknesses of CP boundary layers in feed flow with different Reynolds numbers can be seen in Figure 3.7. All boundary thicknesses in different Reynolds numbers are about 0.125 mm. But a detailed view in Figure 3.7 shows that a higher Reynolds number not only induces a lower CP value but also causes a thinner CP layer thickness.

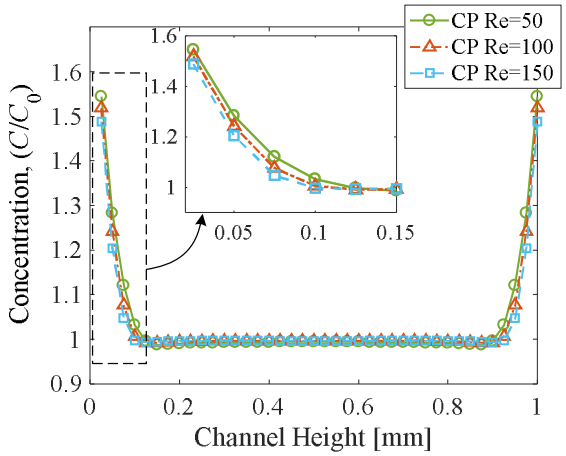

Figure 3.7 Concentration Profile and CP Boundary Thickness in a Plain Channel

The CP prediction with the membrane salt rejection rate varying from 50% ~ 100% is performed by applying the rejection rate coupled mass flux boundary scheme shown in Equation (3.1). Prediction results for CP and permeate flux with different membrane rejection rates are shown in Figure 3.8, which indicate that CP is lower with a lower membrane rejection rate. This is because more salt ions will be transported though the membrane to the permeate side in a lower rejection rate situation and less amount of salt ions will be accumulated near the membrane surface.

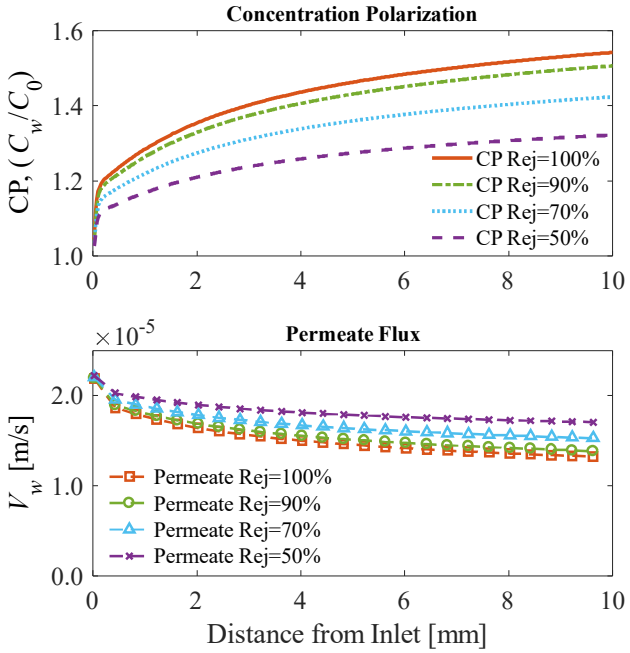

Figure 3.8 CP and Permeate Flux with Different Membrane Rejection Rates

Also, permeate flux prediction results in Figure 3.8 show that the membrane designed with a higher salt rejection rate has lower permeate flux. This conclusion indicates a trade-off between the membrane selectivity (salt rejection) and the membrane permeability (permeate flux), as reported by reference [88] that highly permeable membranes lack the selectivity and vice versa. Detailed review and discussion about the permeability-selectivity trade-off for synthetic membranes can be seen in reference [88].

3.4. CP Prediction in a Spacer Filled Channel

The staggered configuration of the spacer filaments in a desalination channel is illustrated in Figure 3.1. The diameter of the spacer filament is 0.5 mm, and the distance between adjacent spacer filaments is 2.5 mm. In this study, the distance between the center of a cylindrical filament to the nearest membrane is set to be 0.3 mm.

CP prediction results in the spacer filled channel with different Reynolds numbers can be seen in Figure 3.9. Reynolds numbers in Figure 3.9 are calculated using maximum velocities in the channel.

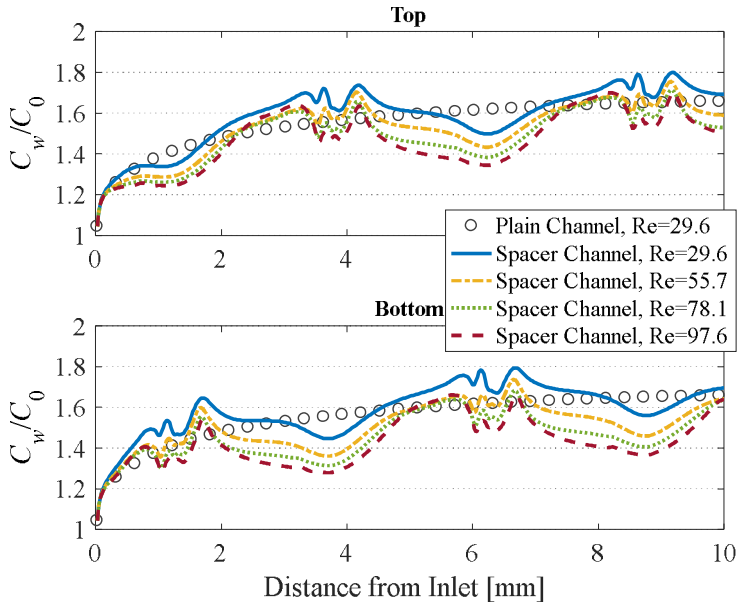

Figure 3.9 CP Near Top and Bottom Boundaries in a Spacer Filled Channel

Results in Figure 3.9 show that CP values near the corner of spacer filaments are higher than those far from spacer filaments. This is because the fluid velocity around the corners of spacers is lower than the velocity far from the spacer elements. However, CP values far from spacers are lower than the plain channel CP values, this is because the cross-flow velocity far from spacer filaments (such as the position between two spacer filaments) in a spacer filled channel are larger than the cross-flow velocity in a plain channel at the same position. Whereas the comparison between a plain channel CP and a spacer filled channel CP with a same Reynolds number (Re = 29.6) shown in Figure 3.9 indicates that plain channel CP is lower than spacer filled channel CP at the spacer filament locations. CP curves shown in Figure 3.9 also shows that the maximum CP near the bottom membrane is almost the same as the maximum CP near the top membrane for

the same Reynolds number. Also, as in the plain channel, a larger CP value can be observed in feed flow with a lower cross-flow Reynolds number Figure 3.9.

The cross-flow velocity in the spacer filled channel with different Reynolds numbers can be seen in Figure 3.10.

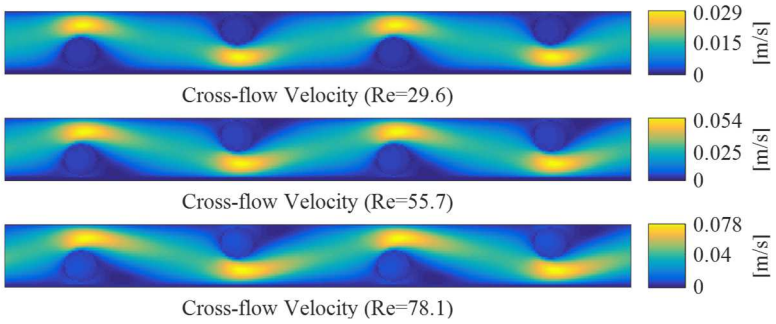

Figure 3.10 Cross-flow Velocity in a Spacer Filled Channel

The concentration distribution profile in the spacer filled channel can be seen in Figure 3.11.

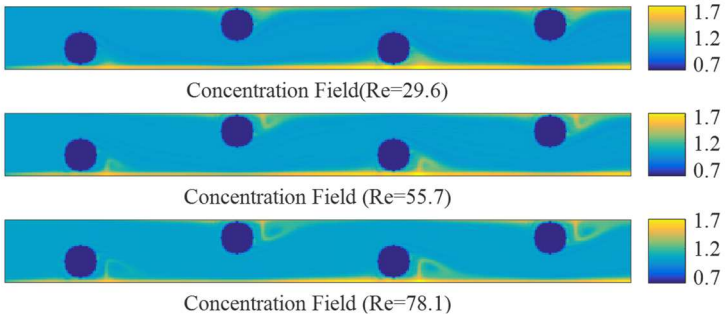

Figure 3.11 Concentration Distribution in a Spacer Filled Channel

Figure 3.11 shows that more rejected salt ions accumulate immediately behind the spacer filaments. This observation conforms to the cross-flow velocity profile shown in Figure 3.10, in which the fluid velocity immediately behind the spacer filaments is lower than that in front of the filaments. Also, a larger Reynolds number reduces the concentration accumulation at this fouling potential area immediately behind the spacer filaments.

4. PREDICTION OF THE FOULING FORMATION*

This section covers the simulation of inorganic fouling growth in terms of the fouling size, formation and mass accumulation. Gypsum scale is selected as a representative for the inorganic fouling, and a single gypsum crystal is focused. First, gypsum growth kinetics is introduced. Thereafter, the implementation of the gypsum growth kinetics and a reacting boundary condition is discussed in the LBM framework. Finally, simulation results of gypsum growth are validated and discussed.

4.1. Gypsum Growth Kinetics

In order to develop effective fouling mitigation strategies, there is a need for a direct quantification of fouling formation on the RO membrane surface.

Q. Kang et. al. proposed a lattice Boltzmann model for crystal growth in a supersaturated solution [81], but the influence of the fluid flow on the growth of the crystal was not considered, and the crystal growth model was also lattice grid dependent. In the present study, a 2×2 mm^2 membrane surface area is targeted. The top and bottom edges of the simulation domain are assumed to be symmetric boundaries. Both hydrodynamic conditions and mass transfer parameters are set to be the same as those in the CP prediction model, except the pressure gradient ($G = -\partial p/\partial x$) in the feed channel since the cross-flow velocity near the membrane surface should be lower than the cross-flow velocity in the bulk flow. The pressure gradient is set

*Part of this section is reprinted with permission from "Numerical Modeling of Concentration Polarization and Inorganic Fouling Growth in the Pressure-Driven Membrane Filtration Process" by Wende Li, et al., 2019. Journal of Membrane Science, 569, 71-82 (https://doi.org/10.1016/j.memsci.2018.10.007), Copyright [2019] by Elsevier.

to be 160 Pa/m and the cross-flow velocity near the membrane surface is approximately 0.2 times of the cross-flow velocity in bulk flow.

Calcium sulfate dihydrate (gypsum) is selected as the mineral scalant, given its common occurrence in desalination of ground brackish water as well as its tenacity of the formed gypsum scale [31][89]. While calcite scaling can be controlled by pH adjustment, gypsum scaling remains one of the major factors that limits the product water recovery [30]. In this study, a direct simulation of the gypsum scale formation at a single crystal level is targeted with respect to different solution supersaturation levels on the membrane surface.

Two pathways for the crystallization have been identified [90]: surface (heterogeneous) crystallization and bulk (homogeneous) crystallization. A variety of studies showed that at low supersaturation levels (supersaturation ratio $SI < 3$), the gypsum nucleation mechanism was heterogenous [91][92]. Thus, only the dominant surface crystallization mechanism in the pressure-driven membrane filtration process by inorganic salts $CaSO_4$ is considered here. According to Cohen [29], the growth of a single gypsum crystal on the membrane surface can be described by standard diffusion gypsum growth kinetics as shown in Equation (4.1).

$$\frac{dM}{dt} = k_m A_c \left(C - C_s \right) \tag{4.1}$$

In Equation (4.1), M is gypsum crystal mass, A_c is the single crystal surface area in contact with the solution, C and C_s are the solution concentration and saturation concentration, respectively, and k_m is the solute mass transfer coefficient in crystal growth.

Equation (4.1) shows that growth of gypsum crystal mass, at a given solution saturation with respect to the gypsum (i.e., SI_g), is directly proportional to the gypsum crystal surface area. Also, surface gypsum crystals gradually grow into rosette structures as reported in [29] for RO

membrane desalination. A hemispherical geometry is taken to represent the gypsum rosette, thus, Equation (4.2) can be derived from Equation (4.1).

$$\frac{dM}{dt} = \frac{d\left(\frac{2}{3}\pi r_{eq}^3 \rho_g\right)}{dt} = 2\pi\rho_g r_{eq}^2 \frac{dr_{eq}}{dt} = k_m \cdot 2\pi r_{eq}^2 \left(C - C_s\right) \tag{4.2}$$

In Equation (4.2), r_{eq} is the equivalent radius of the coverage area by a single crystal, ρ_g is the effective density of the gypsum crystal. Thus, the gypsum crystal growth equation can be derived and given by Equation (4.3).

$$\frac{dr_{eq}}{dt} = \frac{k_m}{\rho_g}\left(C - C_s\right) \tag{4.3}$$

Hasson [28] proposed that the radial growth of gypsum crystals is described by the widely adopted kinetic expression shown in Equation (4.4).

$$\rho_g \frac{dr}{dt} = k\left(C_w - C_s\right)^n \tag{4.4}$$

In Equation (4.4), C_w is the solute mass concentration at the membrane surface, k is the crystallization rate coefficient, and n is the order of the kinetic equation.

The value of n is either 1 or 2 [4][28] in Equation (4.4). When the crystallization process is diffusion controlled, $n = 1$ and $k = k_m$ (mass transfer coefficient in crystal growth). When the crystallization process is controlled by a surface reaction, $n = 2$ and $k = k_r$ (surface integration rate coefficient).

It should be noted that Cohen [31] and Lee [93] stated that $CaSO_4$ crystallization in the cross-flow membrane system follows a first-order equation ($n = 1$). Thus, the derived crystal growth equation shown in Equation (4.3) should be the same as Hasson's kinetic expression show in Equation (4.4). In this study, gypsum growth kinetics expressed in Equation (4.1) and Equation (4.3) will be implemented in the crystal growth LBM model.

4.2. Implementation of the Crystal Growth Model in LBM

4.2.1. Implementation of Gypsum Growth Kinetics

A node number independent crystal growth implementation scheme is developed in LBM for the direct evaluation and quantification of crystal growth radius and mass. If a constant mass transfer coefficient k_m is supposed, the rate of surface crystallization is directly proportional to the membrane wall concentration of $CaSO_4$ salts [93]. Discretizing Equation (4.3) yields Equation (4.4).

$$\Delta r_{eq} = \frac{k_m}{\rho}\left(C_w - C_s\right)\Delta t \tag{4.4}$$

The saturation concentration C_s of calcium sulfate at a given temperature can be estimated through Equation (4.5).

$$C_s = \left(1846 + 9T\right)\times 10^{-3} \quad \left[\mathrm{g/L}\right] \text{or} \left[\mathrm{kg/m^3}\right], \quad 15 \le T \le 30\ ^\circ\mathrm{C} \tag{4.5}$$

The saturation concentration C_s of calcium sulfate is calculated to be 2.071 g/L at a given temperature of 25 °C. The concentration of $CaSO_4$ in seawater near the membrane surface $C_w = SI \times C_s$, in which SI is the supersaturation ratio. Since the crystal growth in LBM may not necessarily be a circle, the equivalent radius r_{eq} is used record the crystal size by transforming the arbitrary shape into a circular form, as seen in Figure 4.1.

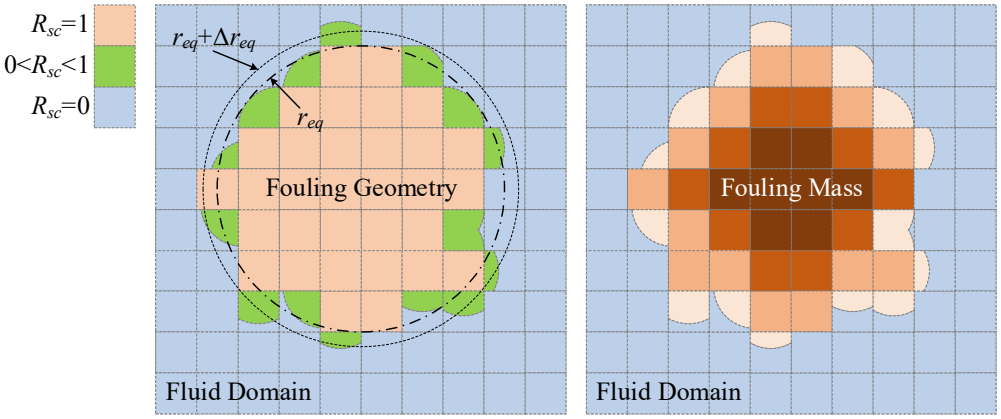

Figure 4.1 Implementation of the Fouling Growth Model in LBM

A node coverage ratio of the gypsum crystal R_{sc} is defined to record the growth of the crystal, as shown in Equation (4.6).

$$R_{sc}:\begin{cases} R_{sc}=1, \text{ fully covered} \\ 0<R_{sc}<1, \text{ partially covered, growing} \\ R_{sc}=0, \text{ not covered} \end{cases} \tag{4.6}$$

The value of R_{sc} for partially covered nodes (light green areas in Figure 4.1) will increase in each time step by Δr_{eq}. The boundary nodes may not necessarily be at the boundary; they actually include all partially covered and still growing nodes. A fully covered node, although at the boundary, will not contribute to the radius growth, but its mass increase will be ongoing. Once a partially covered node becomes a fully covered node, one of the nearest liquid nodes becomes a solid partially covered node, following Kang's crystal nodes expansion scheme [81]. At each time step, the grown portion of the fouling mass Δm_{eq} is distributed equally to all solid fouling nodes including both the fully covered nodes and the partially covered nodes. The developed node number independent LBM implementation scheme is capable of predicting the crystal morphology and quantifying the crystal growth size.

4.2.2. Implementation of a Reaction Boundary

Gypsum growth kinetics depends highly on the solute concentration around growing fouling. Thus, the curved boundary condition at the fluid-solid interface is critical in simulating the fouling size and the fouling morphology. In this study, the first-order kinetic-reaction model [81] shown in Equation (4.7) is used at the fluid-fouling interface.

$$D\,\partial C/\partial \mathbf{n} = k_r\left(C - C_s\right) \tag{4.7}$$

In Equation (4.7), D is the diffusivity of salt ions, C is the solute concentration at the interface, C_s is the solute saturation concentration, k_r is the local reaction rate, and $\mathbf{n}$ is the direction normal of a staircase boundary pointing toward the fluid phase.

From Equation (4.7) and discussions in Appendix A, the term ($-D\partial C/\partial \mathbf{n}$) is diffusion flux flowing out of the solid phase toward the fluid phase, thus the term ($D\partial C/\partial \mathbf{n}$) on the left-hand side of the Equation (4.7) represents reaction flux of the gypsum ions from the fluid phase to the solid phase to provide ions for continuous crystallization of the fouling crystal. In this study, the curved reaction boundary is prescribed using the proposed flux boundary scheme in Equation (2.45) and Kang's reactive transport method [81].

The implementation of the present boundary scheme is illustrated in Figure 4.2. In Figure 4.2, the rosette structure of the surface gypsum crystal is illustrated by a circular structure and then numerically approximated by zig-zag staircases. Indicators will be defined to find and mark different types of cells in the simulation domain.

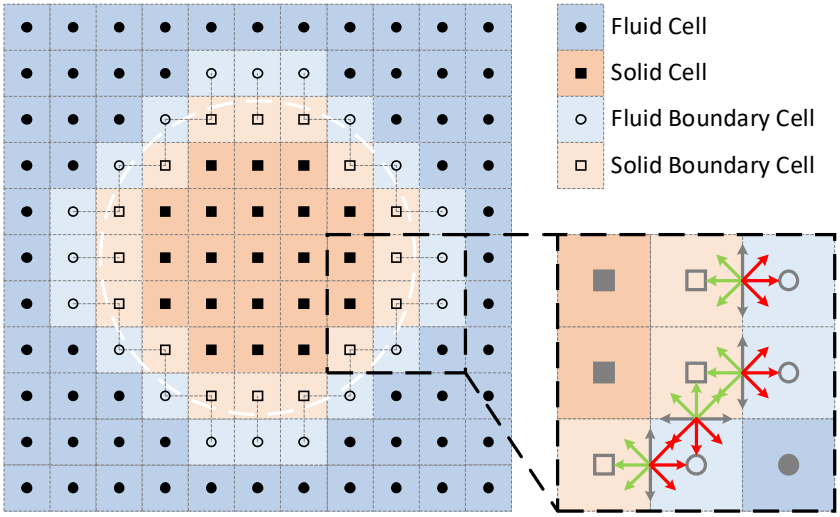

Figure 4.2 Implementation of the Flux Scheme in Staircase Fouling Structure

All staircase edges at the interface between a solid boundary cell and a fluid boundary cell are reaction edges, which will be applied with the reaction boundary shown in Equation (4.7). Substitution of the reaction boundary Equation (4.7) into the present boundary scheme expressed in Equation (2.45) yields Equation (4.8).

$$\underbrace{\sum_{\mathbf{e}_i\cdot\mathbf{n}>0} g_i\mathbf{e}_i\cdot\mathbf{n}}_{\text{unkonwn}}+\underbrace{\sum_{\mathbf{e}_i\cdot\mathbf{n}\le 0} g_i^{+}\mathbf{e}_i\cdot\mathbf{n}}_{\text{konwn}}=\left(\mathbf{u}C-D\nabla C\right)\cdot\mathbf{n}=\left(\mathbf{u}\cdot\mathbf{n}\right)C-k_r\left(C-C_s\right) \tag{4.8}$$

Equation (4.8) indicates that there is always a negative sign attached to the term $k_r(C\text{-}C_s)$ at reaction edges with different unit normal vectors **n** on different boundaries. This means that reaction mass flux is always in the opposite direction of the unit normal vector **n**, and the reaction mass flux should flow from the fluid phase toward the solid phase.

4.3. Crystal Growth Simulation Results

The initial plate-like gypsum crystal grows radially outward from a growth center, forming a rosette structure which blocks the permeation area of a membrane. To validate the proposed gypsum crystal growth model in LBM, results of an experimental study by Cohen [94] about the influence of bicarbonate on membrane gypsum scaling are used for comparison.

In the experimental study by Cohen [94], bicarbonate concentration was varied ($HCO_3^- \leq$ 7.81 mM) for a fixed initial gypsum saturation index at the membrane surface of 2.0. Time evolutions of crystal rosettes clearly demonstrate that there was a remarkable retardation of gypsum scale growth with the increase of the bicarbonate concentration. Simulation results from the LBM model are compared with experimental data of crystal rosette radii under different bicarbonate concentrations. In the experimental study by Cohen [94], linear growth of crystal rosettes with time was observed. Consequently, experimental data is linearly fitted to obtain the mass transfer coefficient in Equation (4.4) based on the proposed method in [29]. The calculated mass transfer coefficient is 2.949×10^{-5} m/s, which is located in the range of $1.4\times10^{-5} \sim 8.1\times10^{-5}$ m/s estimated under operating conditions in [31][94] using a mass transfer coefficient estimation method proposed in [87]. The size of a nucleus originated by the primary nucleation is usually less than 10^{-8} m [95], so in this paper, the initial equivalent radius of the nucleus is selected to be 1×10^{-8} m. The initial mass of the nucleus is estimated using a gypsum crystal density of 2310 kg/m^3.

In the first study, the gypsum crystal growth simulation is performed in the absence of the bicarbonate and with a $CaSO_4$ supersaturation ratio $SI = 2.0$. Simulation results of crystal size and mass accumulation using the present boundary scheme and Kang's reaction boundary are shown in Figure 4.3. The dashed crosslines in Figure 4.3 show the initial nucleation positions, which clearly indicate that crystals are more prone to grow in the opposite direction of the feed flow (feed flow direction is from left to right). This conforms to experimental observations [29] shown in Figure 4.4, in which growth of gypsum crystals is more prone in the direction opposite to that of feed flow. This phenomenon could be explained by local fluid and concentration simulation results, shown in Figure 4.5 and Figure 4.6, that the salt concentration decreases from the crystal frontal flow-stagnation edge to the rear of the crystal, and higher concentration induces faster growth in the direction opposite to the feed flow direction.

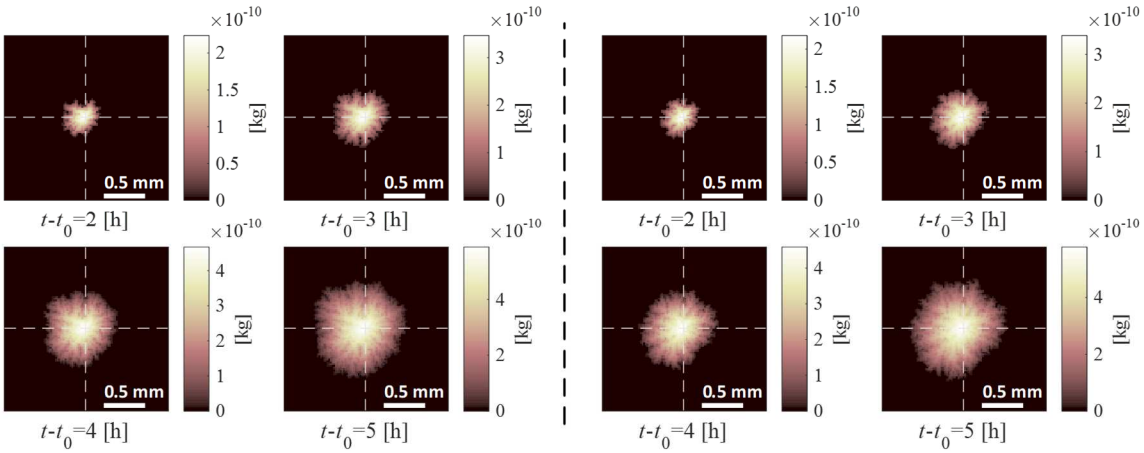

Figure 4.3 Fouling Formation: Present Scheme (Left) and Kang's Scheme (Right)

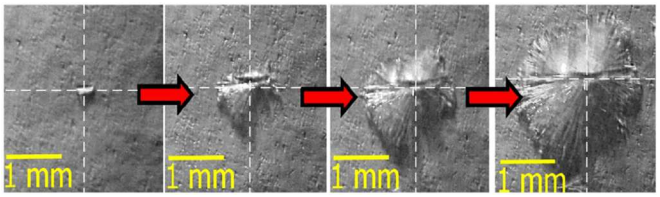

Figure 4.4 Asymmetric Growth of Gypsum Crystal Fouling

Figure 4.5 also shows that crystals on the membrane surface act as solid obstacles and affect the local cross-flow velocity due to applied no-slip boundaries around crystals.

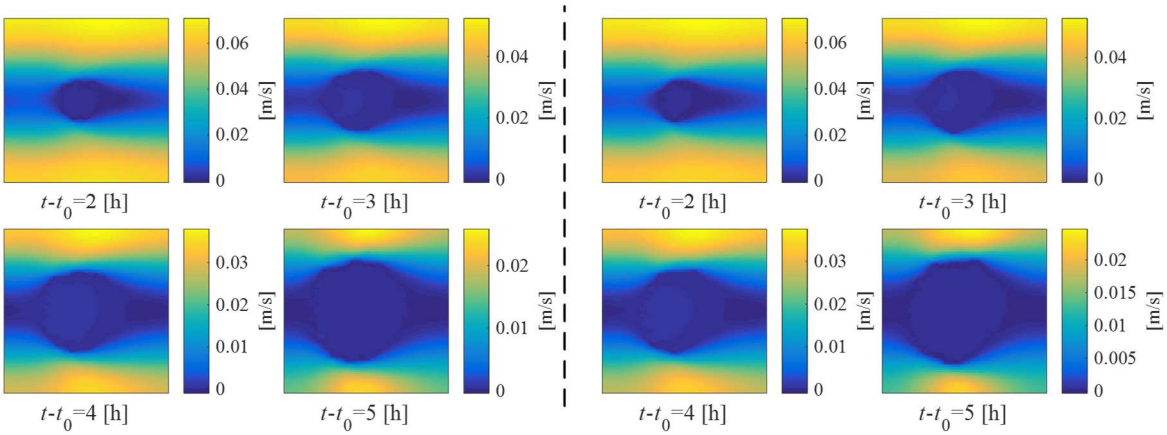

Figure 4.5 Cross-flow Velocity: Present Scheme (Left) and Kang's Scheme (Right)

Axially asymmetric growth of the gypsum crystal could be explained by concentration simulation results as shown in Figure 4.6. The salt concentration decreases from the crystal frontal flow-stagnation edge to the rear of the crystal, and a higher concentration induces faster growth of the crystal toward the direction opposite to the feed flow direction. The reduced calcium sulfate concentration at the rear of the crystal results from mixing eddies caused by the abrupt obstacle of the non-permeation crystal. Gypsum crystallization gradually consumes salt ions around the crystal, thus the salt concentration layer around the crystal is lower than the concentration in bulk flow.

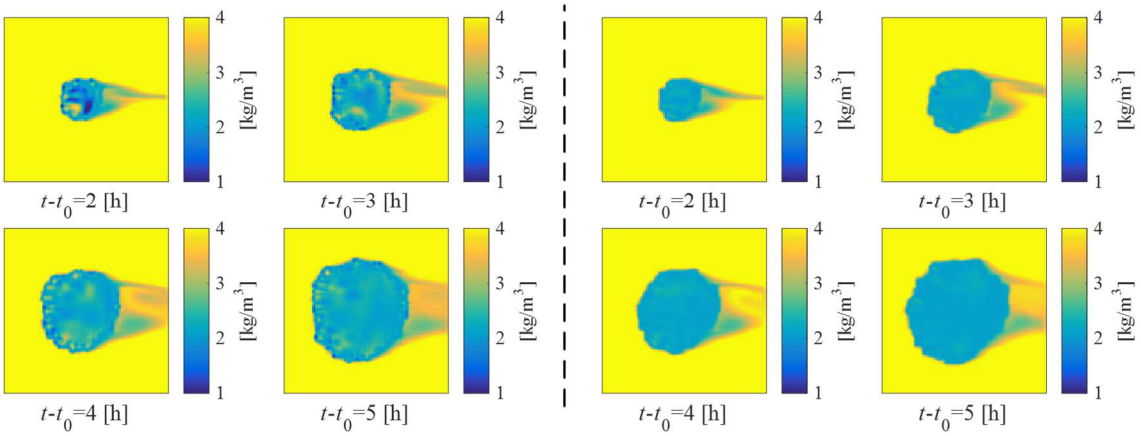

Figure 4.6 Field Concentration: Present Scheme (Left) and Kang's Scheme (Right)

Simulation results from the present boundary scheme and Kang's reaction scheme [81] show that equivalent radii of fouling crystals are 0.190 mm, 0.286 mm, 0.381 mm, and 0.475 mm, for growing time of 2 hours, 3 hours, 4 hour, and 5 hours, respectively. Inorganic fouling growth simulation results in Figure 4.3 and Figure 4.6 show that when used to prescribe the reaction boundary condition in Equation (4.7), the present boundary scheme agrees well with Kang's reaction scheme in terms of the crystal size, mass accumulation and concentration distribution around the fouling crystal. Implementation procedures of the present boundary scheme in staircase approximated curve boundaries are actually the same with those in straight boundaries.

Linear growth of crystal rosettes with time was observed experimentally with a nearly constant rate that decreased with rising bicarbonate concentration [94]. Bicarbonate adsorption was assumed as a plausible explanation for the observed gypsum scale retardation following the Langmuir isotherm. For growth of gypsum crystal rosettes on RO membranes, the relevant Langmuir adsorption isotherm for a monolayer of bicarbonate adsorbed onto the gypsum crystal surface can be represented by Equation (4.9).

$$\Theta = \frac{K_A \left[\mathrm{HCO_3^-} \right]_{\mathrm{lm}}^{T}}{1 + K_A \left[\mathrm{HCO_3^-} \right]_{\mathrm{lm}}^{T}} \tag{4.9}$$

In Equation (4.9), Θ is the fraction of a crystal surface area occupied by the bicarbonate adsorbed layer, the HCO_3^- term is the local bicarbonate concentration at the membrane surface (mM), and K_A is the adsorption equilibrium constant (mM^{-1}). From Equation (4.1), the growth of the gypsum crystal mass is directly proportional to the gypsum crystal surface area at a given solution supersaturation. Therefore, the rate of the crystal rosette radius growth can be derived as shown in Equation (4.10).

$$\frac{dr'_{eq}}{dt} = (1-\Theta)\frac{k_m}{\rho_g}(C - C_s) = (1-\Theta)\frac{dr_{eq}}{dt} \tag{4.10}$$

In Equation (4.10), (1-Θ) is the fraction of the gypsum surface area free of bicarbonate.

Figure 4.7 shows a comparison of simulation results and test data in terms of the gypsum crystal equivalent radius under different bicarbonate concentrations. The mass transfer coefficient in the crystal growth model Equation (4.1) with bicarbonate is set the same (2.949×10^{-5} m/s) as without bicarbonate (HCO_3^-<0.01 mM). The adsorption equilibrium constant K_A is set to be 0.25±0.05 mM^{-1} for all cases with bicarbonate [94]. Simulation results by the LBM agree well with test data, and indicate a stronger gypsum scaling retardation with increased dosage of bicarbonate. Also, the LBM simulation based on the Langmuir adsorption isotherm supports the hypothesis that the bicarbonate adsorption onto the gypsum crystals is the mechanism for the retardation of the surface gypsum crystal development.

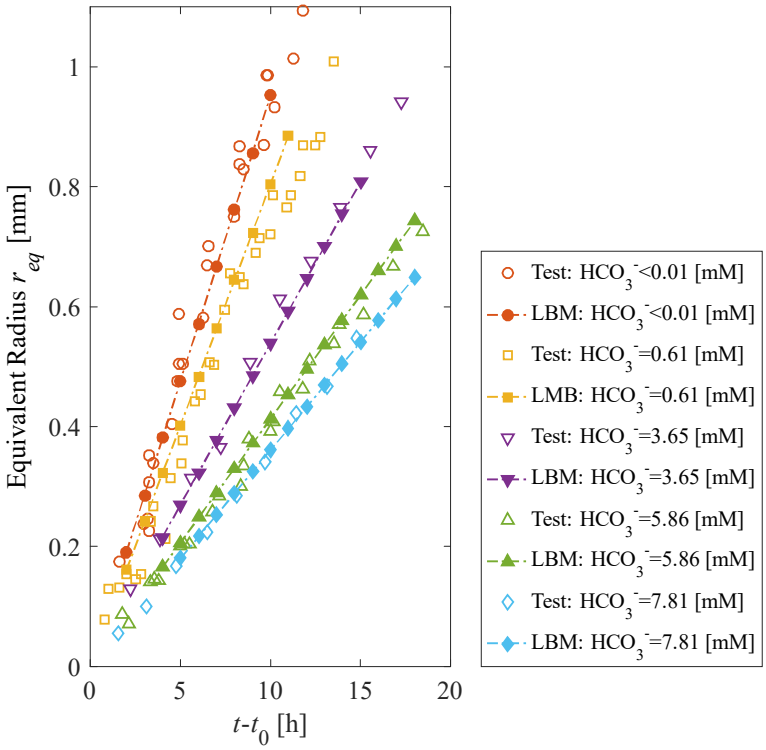

Figure 4.7 Equivalent Radius of Fouling with Different Bicarbonate Concentration

Mass accumulations of gypsum scale under different supersaturation conditions are plotted in Figure 4.8. Simulation results agree well with analytical results based on the hemisphere hypnosis of the crystal structure following Equation (4.2).

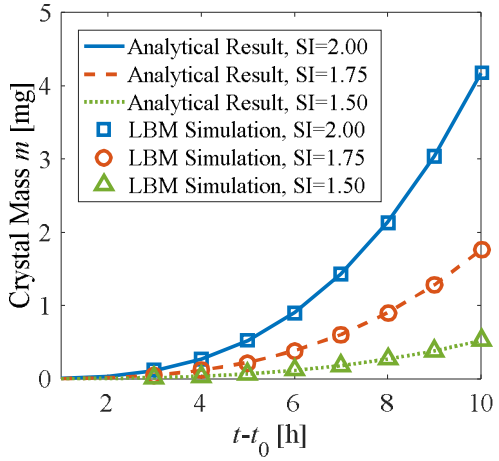

Figure 4.8 Mass Accumulation of Crystals with Different Supersaturation Ratios

Crystal growth results in terms of the equilibrium radius and mass accumulation along the channel length of the spacer filled desalination channel are obtained analytically and numerically with a growth time of 4 hours, as shown in Figure 4.9. CP values (Re = 97.6) along the top membrane are used as supersaturation ratios by assuming that ions in the feed flow are fully saturated for simplicity. The analytical result is obtained using Equation (4.4) and CP prediction data. Figure 4.9 shows that crystals grow larger at corner areas immediately in front of and behind spacer filaments along the channel length direction. Locations of the spacer filaments along the channel length direction (in x-axis) are also shown in Figure 4.9.

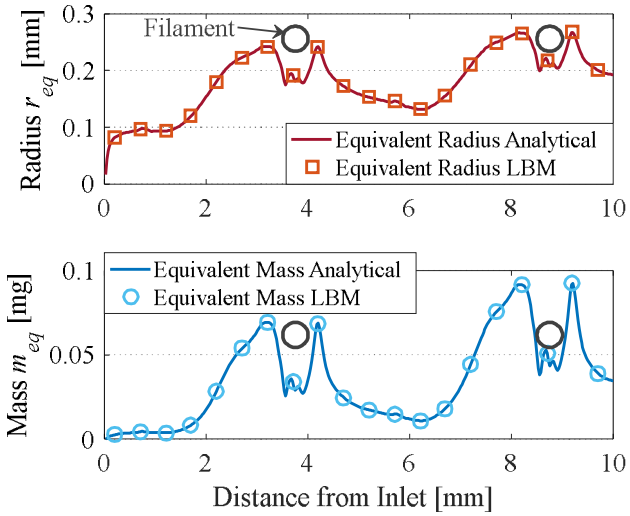

Figure 4.9 Fouling Equivalent Radius and Accumulated Mass Along Channel Length

Figure 4.9 shows that numerical results of crystal growth on the membrane along the channel length match well with analytical results. Without the fully saturation assumption of feed flow, the CP prediction result can still be used to calculate corresponding supersaturation ratios, since CP is a relative value between the concentration near the membrane and that in feed flow.

5. VIBRATION ASSISTED DESALINATION*

A novel vibration assisted desalination technique is proposed in this study to address the membrane fouling problem resulting from inorganic salt foulants, with the aim of increasing permeate flux and enhancing the overall RO membrane performance. The vibration assisted desalination process is realized by a linear motor driven vibratory desalination cell. Test results about CP values and membrane fouling indices are discussed in this section.

5.1. Experimental Setup

5.1.1. Membrane and Chemicals

In this experimental study, flat sheet RO membranes are obtained from a spiral wound polyamide RO membrane module for seawater desalination. Each membrane sheet has an active membrane surface area of 60 cm^2 (3 cm × 20 cm, $W \times L$) after installation. All membrane sheets are stored in distilled water in a 10 ℃ environment. Feed spacers and permeate carriers for the desalination cell are obtained from the same spiral wound module.

5.1.2. Feed Water Composition

Artificial seawater is selected as feed solution with a calculated formula shown in Table 5.1. The total dissolved solids (TDS) is about 32000 ppm for the artificial seawater.

Table 5.1 Artificial Seawater Formula

Reagent	Quantity (for 1 Liter Distilled Water)
NaCl	26.726 [g]
$MgCl_2$	2.260 [g]
$MgSO_4$	3.248 [g]
$CaCl_2$	1.153 [g]

*Part of this section is reprinted with permission from "Reverse Osmosis Membrane, Seawater Desalination with Vibration Assisted Reduced Inorganic Fouling" by Wende Li, et al., 2019. Desalination, 417, 102-114 (https://doi.org/10.1016/j.desal.2017.05.016), Copyright [2017] by Elsevier.

5.1.3. Desalination Cell Apparatus

This study utilizes a desalination cell to investigate the effect of the proposed vibration assisted desalination technique on reducing CP and inorganic fouling in membrane desalination processes. As seen in Figure 5.1, the desalination cell is comprised of a top plate with a feed port and a retentate port, a bottom plate with two permeate ports, membrane elements including a feed spacer, a permeate carrier and a piece of the RO membrane sheet, and sealing elements including O-rings and rubber gaskets. High pressure artificial seawater flows into the feed port of the desalination cell as feed water. Fresh product accumulates in the permeate carrier and flows out of the permeate ports, and will be collected by the feed tank after measurement. Concentrated water flows out of the retentate port and will also be collected by the feed tank to form a recycling system and keep the concentration of the feed solution constant.

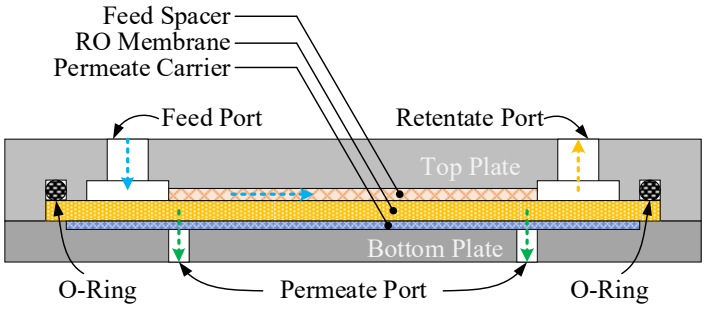

Figure 5.1 Cross-Section Diagram of the Desalination Cell

The desalination cell is driven by a linear actuator according to a variety of signal trajectories with frequencies and amplitudes set by a driver unit. The mechanical system of the desalination cell apparatus can be seen in Figure 5.2, in which the cell is supported on two shafts and four linear bearings. The stiffness of the springs is specified to achieve a resonance vibration of the cell in order to reduce the energy consumption of the vibration.

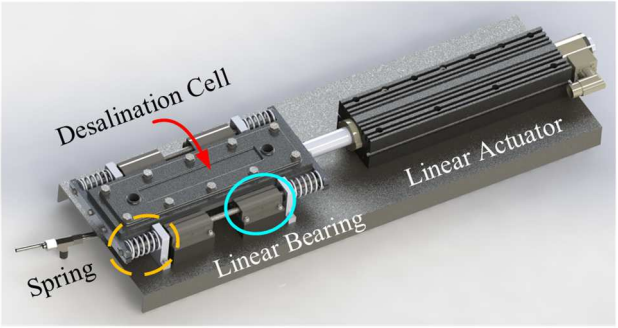

Figure 5.2 Mechanical System of the Vibratory Desalination Cell

5.1.4. Flow Loop Components

The flow loop of the experimental setup is shown in Figure 5.2, which contains a feed tank, a diaphragm pump, and several transducers for water pressure and flowrate measurement.

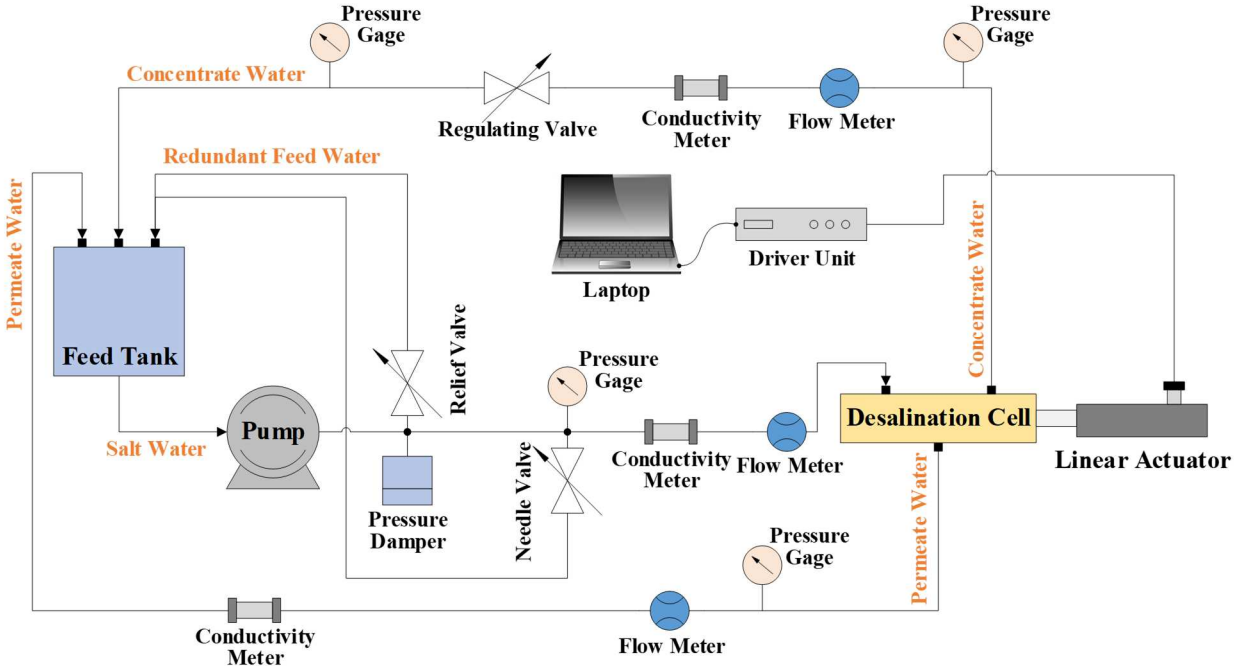

Figure 5.3 Flow Loop System of the Vibratory Desalination Cell

A diaphragm pump is used to provide feed water to the desalination cell with pressure of 800 psi and flowrate of 0.1 gpm. A conductivity meter is used to measure concentrations of feed, permeate and concentrate water. A pressure relief valve is used to control the pressure in flow loop, and a flow regulating valve is used to regulate the feed flowrate. Finally, a pressure

dampener is used to stabilize the feed pressure and eliminate pressure fluctuations during the desalination process.

5.2. CP Reduction in Vibration Assisted Desalination

As illustrated in Figure 5.4, a fully developed velocity profile in a desalination channel without spacers can be modeled as two-dimensional Poiseuille flow. Rejected solutes tend to accumulate near the membrane surface during membrane desalination and form the concentration boundary layer with a thickness of δ_c, as shown in Figure 5.4. The solute concentration is higher in the concentration boundary layer than in bulk flow. Rejection solutes also increase along the channel length (in horizontal direction), thus permeate flux decreases along the channel length, as shown in Figure 5.4.

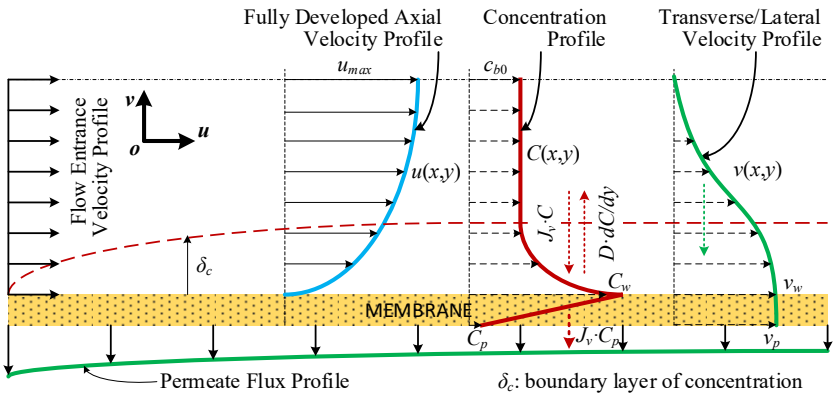

Figure 5.4 Velocity and Concentration Profiles in the Desalination Channel

The steady state concentration profile can be described by the classical stagnant film model [13] and is expressed in Equation (5.1).

$$\frac{C_w - C_p}{C_b - C_p} = \exp\left(\frac{J_v \cdot \delta}{D}\right) = \exp\left(\frac{J_v}{k}\right) \tag{5.1}$$

In Equation (5.1), C_w is the salt concentration at membrane walls, C_p is the salt concentration at permeate side, C_b is the salt concentration in feed bulk flow ($C_b = C_0$), D is the solute diffusion coefficient, $k = D/\delta_c$ is the solute mass transfer coefficient, δ_c is the concentration

boundary layer thickness, and J_v is the convective flux (volumetric flux, with a unit of m/s). Equation (5.2) can be derived from Equation (5.1) after introducing two removal efficiencies.

$$\begin{cases} \ln\left(\frac{1-R_{obser}}{R_{obser}}\right) = \ln\left(\frac{1-R_{true}}{R_{true}}\right) + \frac{J_v}{k} \\ R_{obser} = \frac{C_b - C_p}{C_b},\ R_{true} = \frac{C_w - C_p}{C_w} \end{cases} \tag{5.2}$$

In Equation (5.2), R_{obser} is the observable removal efficiency of a membrane based on the concentration in bulk flow which is actually the membrane rejection rate discussed in Section 3.1.22, and R_{true} is the true removal efficiency of a membrane based on the concentration near the membrane wall. The observable removal efficiency R_{obser} is known since the concentration in bulk flow and the concentration in the permeate side can be measured by the conductivity meter, whereas the true removal efficiency usually is difficult to measure directly. However, the true removal efficiency can be derived from Equation (5.2) and shown in Equation (5.3).

$$R_{true} = \frac{R_{obser} e^{J_v/k}}{1 - R_{obser} + R_{obser} e^{J_v/k}} \tag{5.3}$$

The concentration at the membrane surface C_w can be calculated by R_{true}. In Equation (5.3), the only unknown variable that cannot be measured directly during test is the mass transfer coefficient k. However, the mass transfer coefficient can be numerically estimated according to hydrodynamics conditions. For laminar flow in a thin rectangular channel, the mass transfer coefficient k relates the Sherwood number (Sh) through Equation (5.4) [96].

$$\begin{cases} \mathrm{Sh} = k\frac{d_h}{D} = 1.62\left(\mathrm{Re}\cdot\mathrm{Sc}\cdot d_h/L\right)^{1/3} \\ \mathrm{Re} = \frac{u d_h}{\nu},\ \mathrm{Sc} = \frac{\nu}{D} \end{cases} \tag{5.4}$$

In Equation (5.4), Re is the Reynolds number, d_h is the hydraulic diameter (for flat rectangular channels, $d_h = 2H_c$, with H_c being the channel height), Sc is the Schmidt number, and

L_c is the channel length. There are different relations between the Sherwood number and the mass transfer coefficient [97] but the basic form is similar. The mass transfer coefficient can be derived from Equation (5.4), as shown in Equation (5.5).

$$k = 1.62\left(\frac{uD^2}{2H_cL_c}\right)^{1/3} = 1.62\left(\frac{\gamma D^2}{12L_c}\right)^{1/3} \tag{5.5}$$

In Equation (5.5), γ is the shear rate with a unit of s^{-1} at the membrane surface. For a rectangular channel, the shear rate can be estimated by Equation (5.6).

$$\gamma = \frac{6Q}{W_cH_c^2} = \frac{6u}{H_c} \tag{5.6}$$

In Equation (5.6), the feed flowrate $Q = uA$, with $A = W_cH_c$ the channel cross-sectional area, and W_c is the channel width.

For turbulent flow, perhaps the best-known mass transfer correlation for fully developed turbulent flow is Equation (5.7) [96].

$$\mathrm{Sh} = 0.023\,\mathrm{Re}^{0.8}\,\mathrm{Sc}^{0.33} \tag{5.7}$$

Substituting Equation (5.7) into Equation (5.4) yields the equation of the mass transfer coefficient in turbulent flow, as shown in Equation (5.8).

$$k = 0.02\frac{u^{0.8}D^{0.67}}{H_c^{0.2}\nu^{0.47}} \tag{5.8}$$

Finally, with the mass transfer coefficient obtained, the CP modulus can be calculated by Equation (5.9).

$$\frac{C_w}{C_b} = \left(1 - R_{obser}\right) + R_{obser}\exp\left(\frac{J_v}{k}\right) \tag{5.9}$$

Figure 5.5 is a plot of the CP modulus versus J_v/k with three observable removal efficiencies (or membrane rejection rates) R_{ej} = 0.8, 0.9, 1.0. It can be seen that the CP modulus increasingly

deviates from unity with the increasing of the term J_v/k. Parameters are in accordance to test conditions, which include the cross-flow velocity u = 0.2804 m/s, convective flux $J_v = 1.5\times10^{-5}$ m/s, channel height H_c = 0.75 mm, channel length L_c = 200 mm, diffusion coefficient $D = 1.61\times10^{-9}$ m^2/s, and observable removal efficiency R_{obser} = 97%. The CP moduli with mass transfer coefficients in laminar flow shown in Equation (5.5) and in turbulent flow shown in Equation (5.8) are plotted in Figure 5.5. A predicted CP value of 1.52 for a plain channel in LBM is also plotted in Figure 5.5.

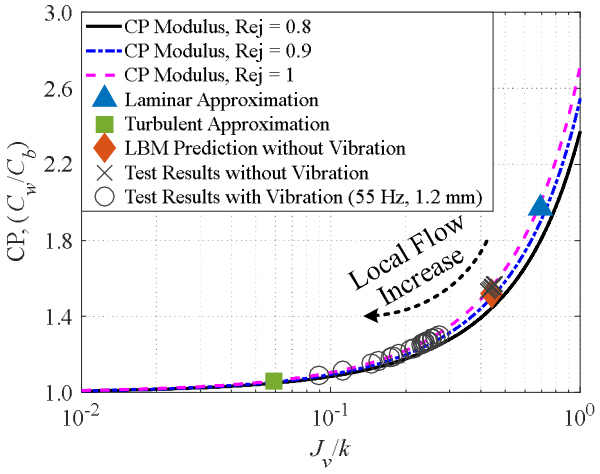

Figure 5.5 Approximated and Measured CP Modulus

Test results of CP modulus shown in Figure 5.5 is based on a mass transfer coefficient measurement method proposed in reference [98]. In this method, high-pressure pure water and salt water are used to feed the desalination cell separately with permeate flux measured. The mass transfer coefficient can be calculated through Equation (5.10) [98].

$$k = \frac{(J_v)_{salt}}{\ln\left\{\frac{\Delta P}{\pi_b - \pi_p}\left[1 - \frac{(J_v)_{salt}}{(J_v)_{pure}}\right]\right\}} \tag{5.10}$$

In Equation (5.10) Δp is applied pressure, (π_b - π_p) is the transmembrane pressure, permeate flux $(J_v)_{pure}$ and $(J_v)_{salt}$ are obtained by feeding the desalination cell with pure water and salt

water, respectively. Figure 5.5 shows that measured CP values are smaller than the estimated CP value using the laminar approximation, this is mainly due to the existing of feed spacers in the desalination channel during test. However, the estimated CP value using turbulent flow is still lower than measured CP values, since the desalination channel is too narrow for turbulence to fully develop inside the channel [20]. Test data in Figure 5.5 also shows that in vibration assisted desalination, CP moduli can be reduced from 1.6 to about 1.2 (with fluctuations). The reduction of CP moduli is due to the enhancement of the cross-flow velocity in vibration assisted desalination. Plots in Figure 5.6 are relations between estimated CP moduli (in laminar flow and in turbulence flow) with different cross-flow velocity Reynolds numbers.

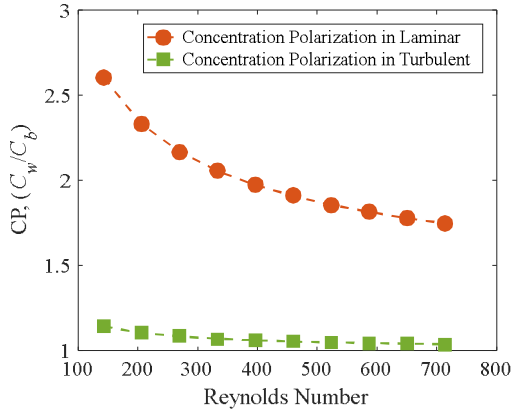

Figure 5.6 CP with Different Reynolds Numbers by Stagnant Film Model

Figure 5.6 shows that with the increasing of the cross-flow velocity Reynolds numbers, CP moduli will be reduced. This can explain the CP reduction in vibration assisted desalination.

5.3. Fouling Reduction in Vibration Assisted Desalination

5.3.1. Metrics of Membrane Fouling

Many studies adopted permeate flux decline [99][89] as an index for membrane fouling. The permeate flux decline (the decline of permeate flux due to fouling divided by initial permeate flux) can be used to quantify the effect of fouling on the productivity of a given desalination process, but does not give an insight into detailed fouling formation [100]. Two commonly used

fouling indices in the industry are the silt density index (SDI) and the modified fouling index (MFI) [101]. It should be noted that MFI is an extension of SDI.

MFI is a very useful method to explain and predict the extent of fouling in membrane desalination. MFI was derived by Schippers [102] based on the well-known cake filtration equation, which is one of the well accepted and mature theories to explain inorganic fouling formation [9] in membrane desalination. Thus, MFI is selected in this study to characterize inorganic fouling formation in desalination tests with and without vibration. The principle of MFI was frequently might not be directly mentioned in literatures. For example, in reference [103], filtration data of different feed compositions was compared and membrane resistance was estimated by the cake filtration theory, which is exactly the MFI method. Although MFI was developed for dead-end filtration, its fouling interpretation idea can be applied in cross-flow membrane desalination [42][101][103]. The vibration assisted desalination can be tested by comparing MFI values with and without vibration under same operating conditions. In this study, both permeate flux decline and MFI are selected as membrane fouling indices during tests.

5.3.2. Experimental Procedures

There is no pretreatment procedure applied to the artificial seawater, so the fouling formation time is correspondingly reduced in this study. To disassociate any flux decline due to membrane compaction, membrane sheets are compacted using distilled water until filtration flux is stable before fouling tests are performed [100]. As a result, any flux decline measured in tests is assumed to be caused by surface fouling only.

A used membrane sheet will be replaced with a new one after each test. The running period of the desalination cell for one test is about 7 to 8 hours. The fresh product is collected with a graduated cylinder at an interval about 5 to 10 min and then weighed with a digital balance.

Permeate water will be recycled to the feed tank after measurement in order to maintain a constant feed concentration.

Feed water temperature is one of the key factors affecting the performance of reverse osmosis membranes. The RO membrane productivity is very sensitive to changes in the feed water temperature, and as the water temperature increases the permeate flux increases almost linearly, due primarily to the higher diffusion rate of water through the membrane. Permeate flux is corrected according to the temperature correction factors (TCF) for polyamide membrane to eliminate the effect of temperature fluctuations of feed water in controlled group tests. Membrane manufacturers usually provide the temperature correction factors. In this study, an empirical formula in Equation (5.11) is given by the membrane manufacturer of the polyamide RO membrane.

$$\mathrm{TCF} = e^{k_t\left[1/298 - 1/(273+t)\right]} \tag{5.11}$$

In Equation (5.11), k_t is a membrane coefficient for a given membrane material, and t is the feed water temperature in degree Celsius. A temperature of 25 °C is the reference temperature point and TCF = 1 for t = 25 °C. The membrane coefficient of k_t = 2700 is usually used [87]. Tests are performed to determine a suitable set of temperature correction factors for the current desalination cell system. It is found that TCF vary with feed water concentrations. In TCF test, feed water contains 32000 ppm of NaCl without any other chemicals is used to eliminate membrane fouling. The membrane is compacted before the test and the temperature vary from 25 °C to 45 °C. TCF data from an industrial database, from the empirical formula in Equation (5.11) and from the TCF test are plotted in Figure 5.7.

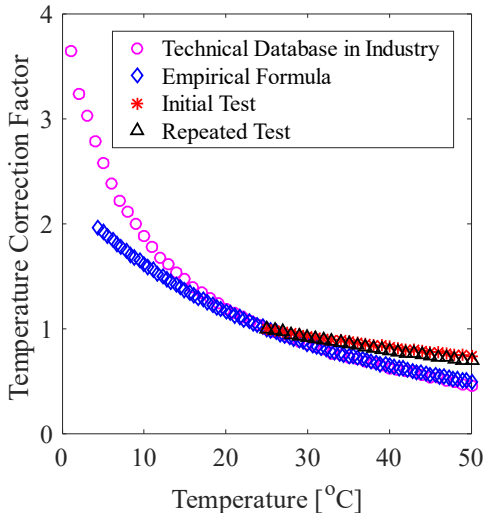

Figure 5.7 Temperature Correction Factors from a Variety of Sources

In this study, the feed water temperature is usually above 25 °C, and all measured permeate flux will be corrected using the tested TCF.

5.3.3. Evaluation of MFI in Vibration Assisted Desalination

Temperature corrected normalized permeate flux under different vibration frequencies can be plotted in Figure 5.8.

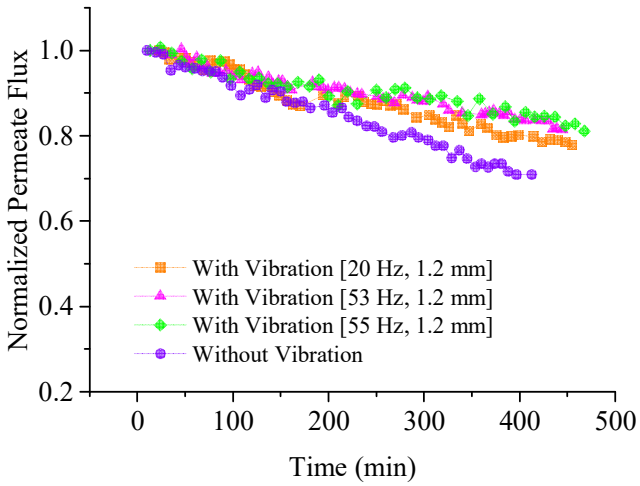

Figure 5.8 Normalized Permeate Flux with Different Vibration Frequencies

Figure 5.8 shows that permeate flux declines in all three control groups in about 400 min. Permeate flux declines about 29% without vibration, about 20% with vibration at 20 Hz, about 16% with vibration at 53 Hz, and about 15% with vibration at 55 Hz.

Mechanisms involved in membrane desalination include blocking filtration, cake filtration without compression, and cake filtration with compression [104], etc., as shown in Figure 5.9.

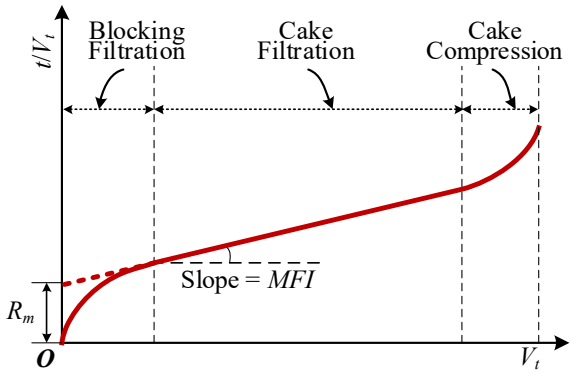

Figure 5.9 Illustration of the Modified Fouling Index

RO membranes have no pores in general, and cake formation will not be preceded by the pore blocking mechanisms [101]. Thus, cake filtration and electrostatic interaction between impurities and the RO membrane surface are the main fouling mechanisms. So, there may be no blocking filtration observed during typical tests. The permeate product rate [102] relates to the cake fouling model through Equation (5.12).

$$\frac{dV}{dt} = \frac{1}{\mu} \frac{\Delta p \cdot A_m}{\left(R_m + R_k\right)} \tag{5.12}$$

In Equation (5.12), V is the accumulated filtrate volume with a unit of m^3, Δp is the applied transmembrane pressure, R_m is the clean membrane resistance with a unit of m^{-1}, R_k is the resistance of the cake or gel per unit of area, A_m is the membrane area, and μ is the dynamic viscosity. If there is no cake compression, then $R_k = I \times V / A_m$, in which I is the fouling potential index (m^{-2}). Integrating both sides of Equation (5.12) assuming a constant Δp yields Equation (5.13).

$$\frac{t}{V} = \frac{\mu R_m}{\Delta p \cdot A_m} + \underbrace{\frac{\mu I}{2\Delta p \cdot A_m^2}}_{\text{MFI}} V \tag{5.13}$$

The MFI value serving as an index for the membrane fouling tendency is actually the slope of the t/V versus V plot, as illustrated in Figure 5.9 and Equation (5.13). The level of fouling on RO membranes can be quantified by evaluating their MFI values, and a higher MFI value indicates severer fouling occurs on the membrane surface due to a larger decline of permeate flux [42]. As discussed by Brauns [105], the linear relation between t/V and V with its slope being defined as the MFI value will hold only if the assumption of a linear relation between cake resistance and permeate volume according to $R_k = I \times V/A_m$ is valid. Calculated MFI values are shown in Figure 5.10 based on test data shown in Figure 5.8 with linear correlation R-Squared values at least 0.98. Figure 5.10 also shows that a higher vibration frequency results in a lower MFI value, or less formed membrane surface fouling on the membrane surface.

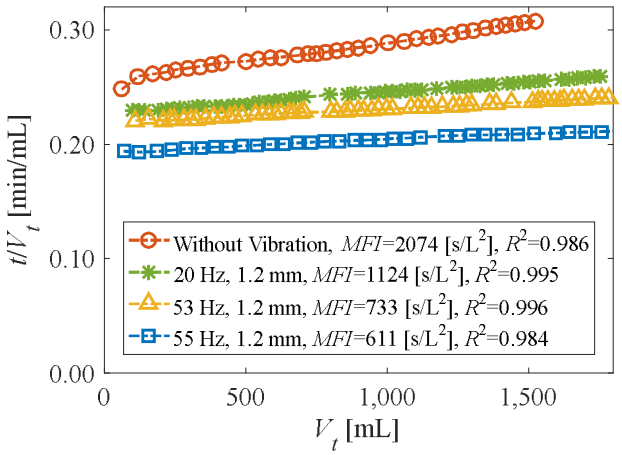

Figure 5.10 MFI Values with Different Vibration Frequencies

Slopes of the linear section of the curves in Figure 5.10 provide information about the extent of membrane surface fouling based on the cake filtration theory. However, absolute values of the curves in Figure 5.10 reflect absolute values of measured permeate flux which usually differ in different control groups due to the concentration variance of feed water.

5.3.4. Correlation Between Vibration Velocity and Permeate Flux

The vibration of the desalination cell disturbs the CP boundary layer and promotes back-diffusion of inorganic salts from the membrane surface. There are a variety of vibration forms, and the vibration velocity is a good index to characterize these vibration forms, since the vibration velocity affects the cross-flow velocity directly. Thus, the correlation between the vibration velocity and permeate flux is studied. Fouling control publications quite often use normalized permeate flux to express the fouling control effect [30]. The normalized flux is defined as the ratio of permeate flux to initial permeate flux (J/J_0, with initial permeate flux around 1.5×10^{-5} m/s). In this study, the average flux is used, which is defined the time integration of permeate flux over the test duration of 450 min, as shown in Equation (5.14).

$$F_{Nave} = \frac{1}{t_b - t_a}\int_{t_a}^{t_b} F_N(t)dt \tag{5.14}$$

In Equation (5.14), $F_N(t)$ is the time varying normalized flux and F_{Nave} is the time averaged normalized permeate flux. The relation between the vibration velocity and permeate flux is studied, as shown in Figure 5.11, based on a group of tests results with different vibration frequencies shown in Figure 5.8 and an extra test with a 10~40 Hz chirp signal.

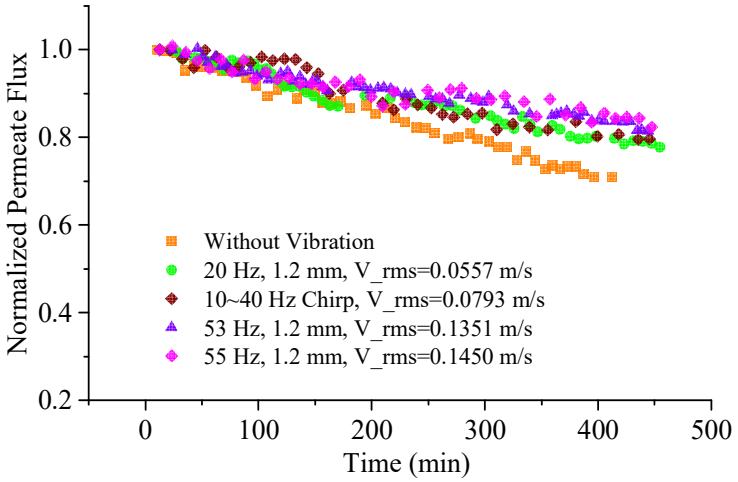

Figure 5.11 Normalized Flux with Different Vibration Velocities

Figure 5.12 is a plot of the correlation between the vibration velocity and the time averaged normalized permeate flux.

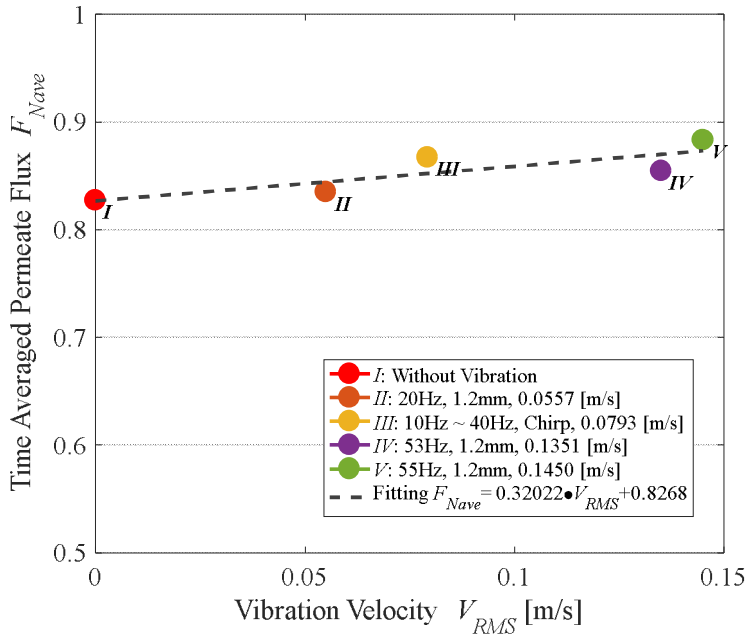

Figure 5.12 Correlation between Permeate Flux and Vibration Velocities

Figure 5.12 shows that the increase of the vibration velocity results in increased normalized flux over the 450 min test duration, and a linear fitting of the test data is obtained, as seen in Equation (5.15).

$$F_{Nave} = 0.3202 \cdot V_{RMS} + 0.8268 \tag{5.15}$$

This correlation can be used as an permeate flux prediction tool in further applications of the vibration assisted desalination technique. The correlation shown in Equation (5.15) should be used for a vibration velocity less than 0.15 m/s and in the initial 8 hours of operation.

6. DESIGN OF A DESALINATION CENTRIFUGE

The challenges of improving the membrane desalination performance include the increase of permeate freshwater flux, and the decrease of membrane fouling, power consumption and hardware cost. A novel desalination centrifuge is designed in this study to accomplish these goals by eliminating the cost of the high-pressure feed pump and mitigating membrane fouling through the vibration assisted desalination technique. Energy consumption calculations show that under certain conditions, the power usage of the desalination centrifuge is less than the industrial average.

6.1. Features of the Desalination Centrifuge

Despite major advancements in desalination technologies, seawater desalination is still more energy intensive compared to conventional technologies for fresh water production, such as the waste water reclamation. Although RO membrane desalination consumes least energy compare to other types of desalination techniques, energy consumption is the largest variable cost for seawater RO plants, varying from a third to more than a half of the total cost. For example, reference [106] summarized that the energy usage can be up to 50% of the operation and maintenance cost in a SWRO facility.

From the membrane side, it is argued that by increasing the membrane permeability, the feed pressure and energy consumption of RO desalination can be reduced. However, a trade-off exists between the membrane selectivity (salt rejection) and the membrane permeability (permeate flux), that highly permeable membranes lack the selectivity and vice versa. Thus, the increase of the membrane permeability will allow more ions to pass through the membrane and thus reduce the membrane salt rejection. Also, as discussed by Elimelech [36], the amount of

energy that can be saved by using nanotube-based or aquaporin-based membranes is likely to be very small.

Current SWRO plants are already operating near the thermodynamic limit of 1.06 kWh/m^3 as power usage (about 3 - 4 times higher than the limit). Thus, a reasonable effort for energy saving desalination is to still utilize the SWRO technology but reduce the energy consumption from the feed side and energy collection point of view. Vickers [107] proposes an ideal energy consumption model for centrifugal reverse osmosis (CRO) and concluded that the ideal energy saving of CRO is 70% if the permeate recovery rate is 15%.

6.1.1. Vibration Assisted Fouling Mitigation

The centrifuge incorporates the vibration assisted desalination process. This process is based on the idea of membrane moving to alter hydraulics near membrane surface, in order to increase the local cross flow velocity and disturb the fluid-solid interface boundary layer. Simulation results and test observations show that the vibration assisted desalination process facilitate the reduction of the CP by increasing the cross-flow velocity and enhancing the mass transfer coefficient at the filtration boundary. A reduced level of permeate flowrate decline indicates that there is less inorganic fouling on the membrane surface in the vibration assisted desalination compared to the traditional (non-vibrating) desalination process.

6.1.2. Reduced Energy Consumption

In traditional desalination plants, pumps are needed to provide 600 - 800 psi high-pressure feed water to squeeze the permeate product out from the feed side. The generation of high-pressure feed water consumes the most portion of electric energy. Also, high-pressure concentrated water coming out of the membrane module also contains hydraulic energy. Thus, energy recovery devices are usually installed at the concentrated side to recover the hydraulic

energy and reduce energy waste. For the desalination centrifuge, only low-pressure pumps are needed to provide feed water with required feed flowrate. The centrifuge will generate 600 - 800 psi pressure for the RO membrane. The hydraulic energy of the concentrated water (which contains approximately 90% of the feed water energy) will be collected by the centrifuge since the concentrated water coming out of the centrifuge is in low pressure.

6.1.3. Reduced CP by Local Flow Instabilities

Rotating RO takes advantage of high shear and the Taylor vortex instability to reduce CP and membrane fouling. For example, a developed rotating RO in reference [52] takes advantage of Taylor-Couette flow instabilities to reduce CP and membrane fouling, and control $CaSO_4$ scale formation. Belfort [108] proposed that controlled centrifugal instabilities (Dean vortices) resulting from flow around a curved channel could be used to reduce both CP and membrane fouling during microfiltration.

6.2. Centrifuge Design

The design of the desalination centrifuge in intended to reduce energy consumption, mitigate membrane fouling and increase fresh water product during the seawater desalination process. The desalination centrifuge has an overall dimension of 1.1 m × 0.61 m × 0.68 m ($L \times W \times H$), and will rotate at 4500 rpm to provide 600 psi feed water, as seen in Figure 6.1. The centrifuge can vibrate axially with a vibration frequency about 20 Hz and a peak-to-peak amplitude about 1.2 mm. The mass of total vibrating parts is about 100 kg. The estimated flowrate increase is about 5% with vibration. To reduce the vibration driving force, the centrifuge will vibrate at the resonant frequency designed to be 20 Hz. Feed flowrate to the centrifuge is about 40 - 60 gpm, and estimated permeate flowrate is about 0.84 - 1.26 gpm.

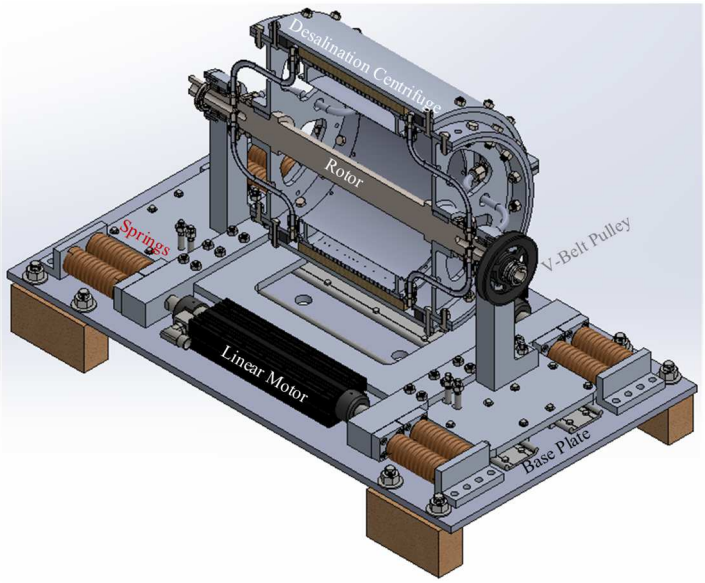

Figure 6.1 Design of the Desalination Centrifuge

The rotation of the centrifuge provides 600 psi pressure to the RO membrane wrap, thus, the high-pressure pumps required in conventional desalination plants can be eliminated for the desalination centrifuge. Also, the energy contained in concentrated water can be collected by centrifuge spokes, and energy consumption will be reduced.

The flow path of the desalination centrifuge can be illustrated in Figure 6.2. Low-pressure feed water goes into the centrifuge from the inlet side of the rotor through a rotary union. The rotating of the centrifuge increases the feed water pressure and part of feed water is squeezed through the RO membrane becoming permeate fresh water. Permeate water flows out of the membrane wrap through the permeate carrier to the permeate collector on the centrifuge. The rest of the water (concentrated brine) flows out from the right end of the rotor, and at this step the hydraulic energy in concentrated brine will also be collected.

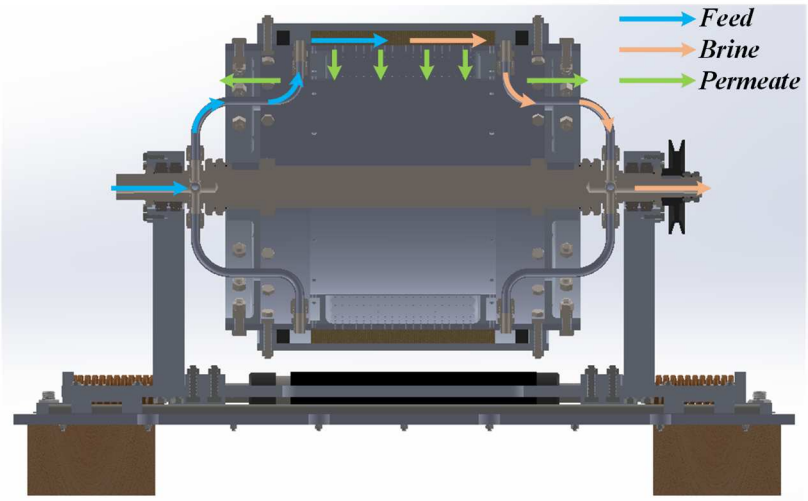

Figure 6.2 Flow Path of the Desalination Centrifuge

The centrifuge is v-belt driven with an electric motor to rotate at the required speed, as shown in Figure 6.3.

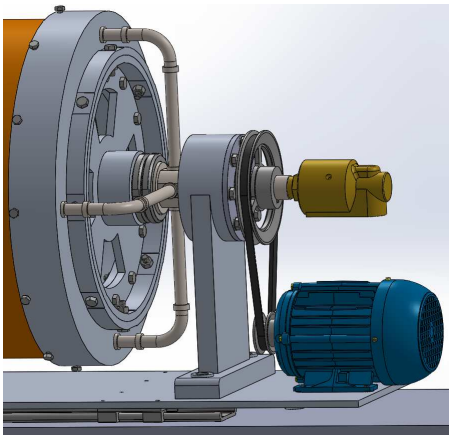

Figure 6.3 Rotation Driven System of the Desalination System

The most widely used commercial RO membrane is the spiral wound membrane module. This configuration can separate feed spacers from permeate carriers with RO membrane sheets. As shown in Figure 6.4, one membrane envelop is comprised of two layers of RO membrane and one layer of permeate carrier. And membrane envelops are separated by feed spacers, in which high-pressure feed water will flow by. The commercial spiral wound membrane wrap usually contains several envelops connecting to the center permeate tube with permeate carrier glued on

it. Thus, the permeate water flows to the center permeate tube and then flows out of the membrane module.

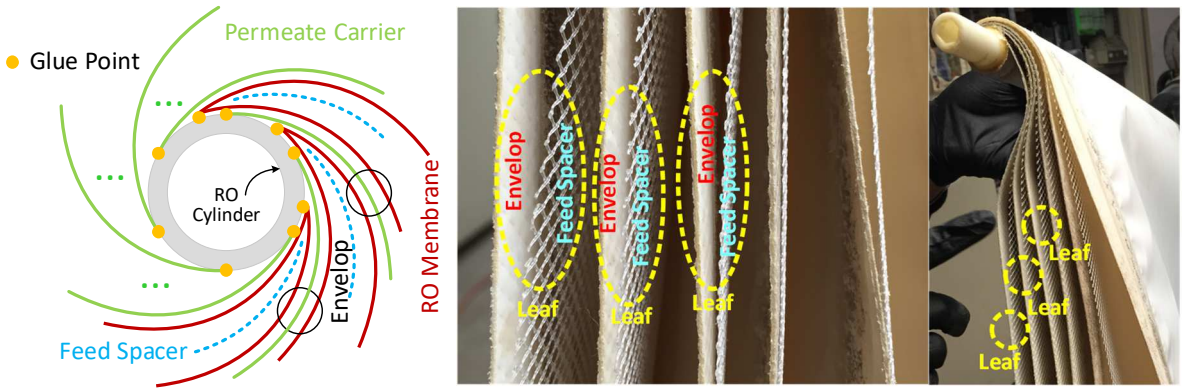

Figure 6.4 Cross-Section of Commercial Spiral Wound RO Membrane

The RO membrane should be glued on the centrifuge permeate cylinder in the same form with the commercial membrane wrapping.

6.3. Vibration System Dynamic Analysis

The centrifuge vibration system can be simplified as a vibrating mass with a spring with stiffness k and a damping component with a damping coefficient c, as illustrated in Figure 6.5.

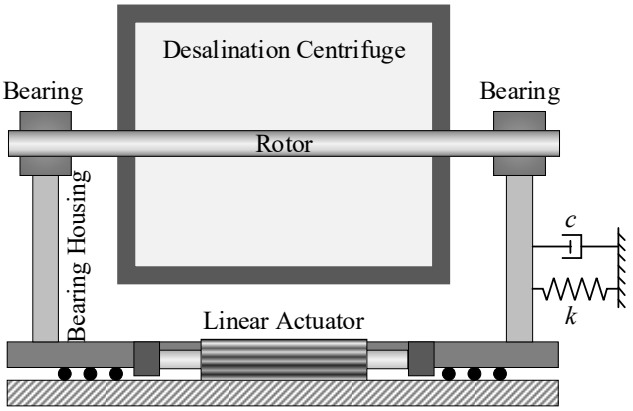

Figure 6.5 Dynamic Model of the Desalination Centrifuge

6.3.1. Analytical Modeling

If a force acts on a viscously damped spring-mass system, the equation of motion can be obtained using Newton's second law, as shown in Equation (6.3).

$$m\ddot{x} + c\dot{x} + kx = F(t) \tag{6.3}$$

Since this equation is nonhomogeneous, its solution $x(t)$ is given by the sum of the homogeneous solution, $x_h(t)$, and the particular solution, $x_p(t)$. The homogeneous solution is the solution of the homogeneous equation shown in Equation (6.4).

$$m\ddot{x} + c\dot{x} + kx = 0 \tag{6.4}$$

Equation (6.4) represents the free vibration of the system. This free vibration dies out with time under each of the three possible conditions of damping (underdamping, critical damping, and overdamping) and under all possible initial conditions. Thus, the solution of Equation (6.3) eventually reduces to the particular solution $x_p(t)$, which represents the steady-state vibration. The steady-state motion is present as long as the forcing function $F(t)$ is present. The part of the motion that dies out due to damping (the free-vibration part) is called transient. The rate at which the transient motion decays depends on the values of the system parameters k, c, and m.

For an underdamped system ($\zeta < 1$), the homogeneous solution $x_h(t)$ can be shown in Equation (6.5).

$$x_h(t) = e^{-\zeta\omega_n t}\left[C_1 \cos\left(\sqrt{1-\xi^2}\,\omega_n t\right) + C_2 \sin\left(\sqrt{1-\xi^2}\,\omega_n t\right)\right] \tag{6.5}$$

Equation (6.4) can be rearranged as shown in Equation (6.6).

$$\ddot{x} + \frac{c}{m}\dot{x} + \frac{k}{m}x = 0 \Rightarrow \ddot{x} + 2\zeta\omega_n\dot{x} + \omega_n^2 x = 0 \tag{6.6}$$

In Equation (6.6), relations between parameters can be shown in Equation (6.7).

$$\begin{cases} \omega_n = \sqrt{\dfrac{k}{m}} \\ 2\zeta\omega_n = \dfrac{c}{m} \Rightarrow \zeta = \dfrac{c}{2\sqrt{km}} \\ \zeta = \dfrac{c}{c_c} \Rightarrow c_c = 2\sqrt{km} = 2m\omega_n \end{cases} \tag{6.7}$$

For any damped system, the damping ratio ζ is defined as the ratio of the damping coefficient c to the critical damping coefficient c_c. If $F(t) = F_0 \sin\omega t$, the corresponding steady-state solution is shown in Equation (6.8).

$$x_p(t) = \frac{F_0}{\left[\left(k - m\omega^2\right)^2 + \left(c\omega\right)^2\right]^{1/2}} \sin\left(\omega t - \phi\right) \tag{6.8}$$

In Equation (6.8), the phase φ is defined in Equation (6.9).

$$\phi = \tan^{-1}\left(\frac{c\omega}{k - m\omega^2}\right) \tag{6.9}$$

Finally, by combining the homogeneous solution and the particular solution, the solution of Equation (6.3) can be given in Equation (6.10).

$$\begin{aligned} x(t) &= x_h(t) + x_p(t) \\ &= e^{-\zeta\omega_n t}\left[C_1 \cos\left(\sqrt{1-\xi^2}\,\omega_n t\right) + C_2 \sin\left(\sqrt{1-\xi^2}\,\omega_n t\right)\right] + \dots \\ &\dots + \frac{F_0}{\left[\left(k - m\omega^2\right)^2 + \left(c\omega\right)^2\right]^{1/2}} \sin\left(\omega t - \phi\right) \end{aligned} \tag{6.10}$$

In Equation (6.10), C_1 and C_2 are arbitrary constants to be determined from initial conditions.

For an initially steady state system, the initial conditions $x(t=0) = 0$, and $x'(t=0) = 0$, thus C_1 and C_2 can be found through Equation (6.11).

$$\begin{cases} C_1 = -\dfrac{F_0}{\left[\left(k - m\omega^2\right)^2 + \left(c\omega\right)^2\right]^{1/2}} \sin\left(-\phi\right) \\ C_2 = \dfrac{\left(\zeta\omega_n C_1 - \dfrac{\omega F_0}{\left[\left(k - m\omega^2\right)^2 + \left(c\omega\right)^2\right]^{1/2}} \cos\left(-\phi\right)\right)}{\sqrt{1-\xi^2}\,\omega_n} \end{cases} \tag{6.11}$$

6.3.2. Results and Discussions

The vibration mass of the centrifuge m = 100 kg, the vibration natural frequency f = 20 Hz, thus the angular velocity $\omega_n = 2\pi f$ = 125.66 rad/s. The required spring stiffness can be calculated for a resonant frequency, as $k = \omega_n^2 m$ = 1.58×10^6 N/m. The system damping ratio ζ is selected to be 0.05, 0.1, 0.15, 0.2, 0.5 to investigate different damping situations. The required peak-to-peak amplitude of the centrifuge vibration is 1.2 mm. The linear actuator will drive the desalination centrifuge according to a determined displacement function $x = x_0 \sin(\omega t)$, in which x_0 = 0.6 mm. The required force for the linear actuator can be calculated through Equation (6.12).

$$F_m = -m\omega^2 x_0 \sin(\omega t) + c\omega x_0 \cos(\omega t) + k x_0 \sin(\omega t) \tag{6.12}$$

If the centrifuge vibration is not resonant, the driving force can also be calculated by Equation (6.12) without the spring term. Suppose the system damping ratio ζ = 0.3, the required driving force with and without using resonant vibration can be seen in Figure 6.6.

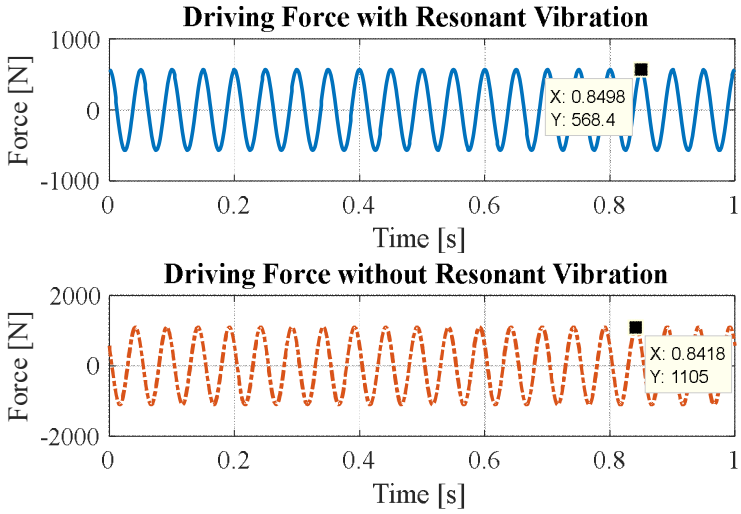

Figure 6.6 Required Driving Force with and without Resonant Vibration

Figure 6.6 shows that the required driving force is about 570 N to achieve the required steady-state shaking amplitude in the resonant vibration. However, the required driving force is

about 1100 N while without using the resonant vibration. Figure 6.7 shows that the required driving force is minimum at the resonant frequency.

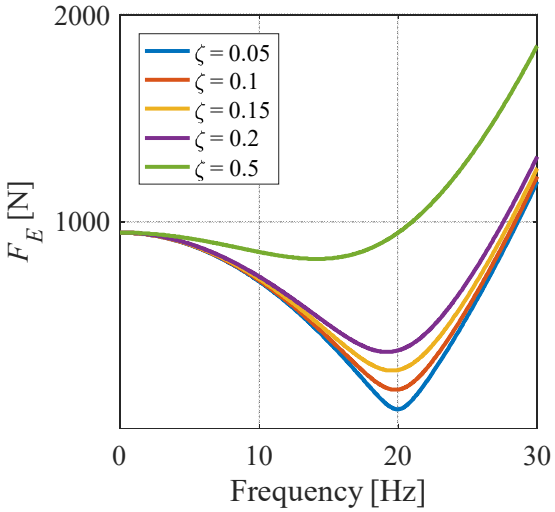

Figure 6.7 Driving Force with Different Vibration Frequencies and Damping Ratios

The calculated driving force $F_0 = F_E = 570$ N is used and the vibration response is obtained for a validation purpose. Both the MATLAB ODE numerical solution and the analytical solution shown in Equation (6.10) are used to obtain the centrifuge vibration response.

The centrifuge vibration response can be shown in Figure 6.8.

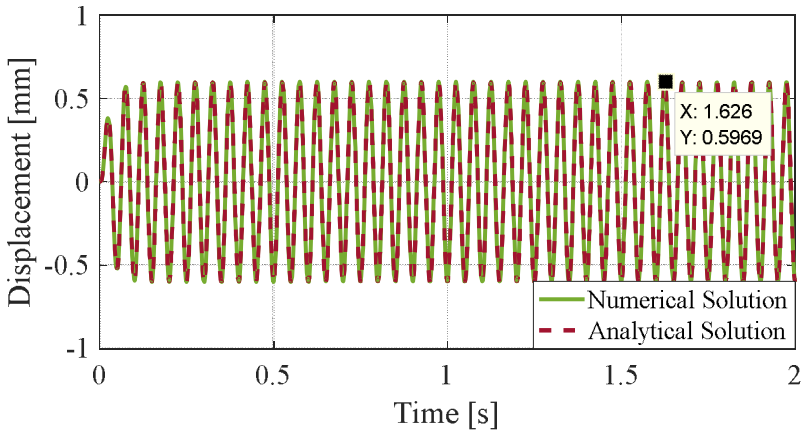

Figure 6.8 Validation of the Centrifuge Vibration Response

Figure 6.8 demonstrates that the centrifuge system can be vibrated at the desired vibration frequency $f = 20$ Hz and a peak-peak amplitude 1.2 mm.

6.4. Centrifuge Power Consumption

The process pressure of a centrifuge can be denoted with Equation (6.13).

$$P_c = \rho\omega^2 R^2 / 2 \tag{6.13}$$

In Equation (6.13), ρ is the fluid density, ω is the centrifuge angular velocity, and R is the centrifuge radius.

The illustration of an idealized continuous flow centrifuge can be shown in Figure 6.9. The feed water will be continuously driven by the centrifuge to gain a certain amount of angular momentum as described in reference [107].

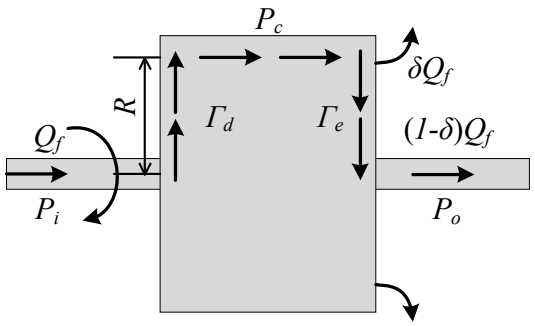

Figure 6.9 Illustration of an Idealized Centrifuge Desalination Process

The angular momentum gained in feed water can be expressed in Equation (6.14).

$$\Gamma_d = \rho Q_f \omega R^2 \tag{6.14}$$

In Equation (6.14), Q_f is feed water volumetric flow rate with a unit of m^3/s. The permeated fresh water is assumed to be thrown out through the centrifuge orifice, while the concentrated exhaust water will be collected by spoke pipes at outlet collection side. The recovered angular momentum is expressed in Equation (6.15).

$$\Gamma_e = \rho(1-\delta) Q_f \omega R^2 \tag{6.15}$$

In Equation (6.5), δ is the recovery ratio which describes the fraction of fresh water collected from feed water. By conservation of angular momentum, the lost angular momentum by permeate water is shown in Equation (6.16).

$$\Gamma_p = \rho \delta Q_f \omega R^2 \tag{6.16}$$

Thus, ideally, the power consumption in each step can be shown in Equation (6.17).

$$\begin{cases} \mathbf{P}_d = \rho Q_f \omega^2 R^2 = 2 Q_f P_c = \mathbf{P}_p + \mathbf{P}_e \\ \mathbf{P}_p = \rho \delta Q_f \omega^2 R^2 \\ \mathbf{P}_e = \rho (1-\delta) Q_f \omega^2 R^2 \end{cases} \tag{6.17}$$

In Equation (6.17), $\mathbf{P}_p$ is the power consumption by permeate water which is also the only power consumption, $\mathbf{P}_e$ is the power consumption by exhaust water which will be collected by the centrifuge, $\mathbf{P}_d$ is the total power consumption by driving the centrifuge. Thus, the total power consumption in an ideal centrifuge desalination process is the power consumption by permeate water only, as shown in Equation (6.18).

$$\mathbf{P}_{des} = \mathbf{P}_p = \mathbf{P}_d - \mathbf{P}_e = \omega \Gamma_p = \rho \delta Q_f \omega^2 R^2 = 2 \delta Q_f P_c \tag{6.18}$$

In Equation (6.18), P_c is the centrifugal pressure. In this study, the recovery ratio of the desalination process is supposed to be δ = (permeate flow rate, gpm/(feed flow rate, gpm)×100% = 2%, the feed water volumetric flowrate Q_f = 0.00252 m^3/s (40 gpm), and the centrifugal pressure is 4.137×10^6 Pa (600 psi), thus final power consumption during the centrifugal desalination process can be calculated by Equation (6.18) and shown in Equation (6.19).

$$\mathbf{P}_{des} = 2 \delta Q_f P_c = 2 \times 0.02 \times 0.00252\, m^3/s \times 4.137 \times 10^6\, N/m^2 = 417 W \tag{6.19}$$

If the power collection process is not ideal, part of the energy in exhaust water will not be recovered. An energy recovery ratio to λ is defined which is the percentage of the recovered energy from the total energy consumption. For example, if 99% of the energy in exhaust water

($\mathbf{P}_e$) can be collected, thus $\lambda = 0.99$, and the final power consumption in the centrifugal desalination process is shown in Equation (6.20).

$$\begin{aligned}
\mathbf{P}_{des} &= \mathbf{P}_p + (1-\lambda)\mathbf{P}_e = \mathbf{P}_d - \lambda\mathbf{P}_e \\
&= \rho Q_f \omega^2 R^2 - 0.99\rho(1-\delta)Q_f \omega^2 R^2 \\
&= \rho Q_f \omega^2 R^2 - 0.99\rho Q_f \omega^2 R^2 + 0.99\rho\delta Q_f \omega^2 R^2 \\
&= 0.01\rho Q_f \omega^2 R^2 + 0.99\rho\delta Q_f \omega^2 R^2 \\
&= \left(0.01 Q_f + 0.99\delta Q_f\right)\rho\omega^2 R^2 \\
&= 2\left(0.01 Q_f + 0.99\delta Q_f\right)P_c \\
&= (0.02 + 1.98\delta) Q_f P_c = 621\text{kW}
\end{aligned} \tag{6.20}$$

In the derivation of Equation (6.20), the friction loss due to roller bearings of the centrifuge $\mathbf{P}_f$ is ignored, and the windage loss of the centrifuge $\mathbf{P}_{win}$ is also be ignored assuming the centrifuge is running in a vacuum housing. Thus, the total power consumption $\mathbf{P}_t = \mathbf{P}_{des}$.

The calculated permeate flux is $Q_p = r_c Q_f = 0.8$ gpm $= 0.1816$ m^3/h for the desalination centrifuge. Thus, in the ideal case, the unit power consumption can be calculated as shown in Equation (6.21).

$$U_p = \mathbf{P}_t / Q_p = (417/0.1816)\,\text{Wh/m}^3 = 2.3\,\text{kWh/m}^3 \tag{6.21}$$

Typical SWRO system energy usage is about 3.0 kWh/m^3, thus, ideally there would be 23.3% energy saving per cubic meter of water production.

For the non-ideal case with 99% energy recovery ratio, the unit power consumption can be calculated as shown in Equation (6.22).

$$U_p = \mathbf{P}_t / Q_p = (621/0.1816)\,\text{Wh/m}^3 = 3.42\,\text{kWh/m}^3 \tag{6.22}$$

In an ideal case, the energy consumption by exhaust water will all be collected or recovered. In a non-ideal case, the energy recovery ratio of the exhaust water power consumption $\mathbf{P}_e$ above 99% is calculated by Equation (6.20) and plotted in Figure 6.10.

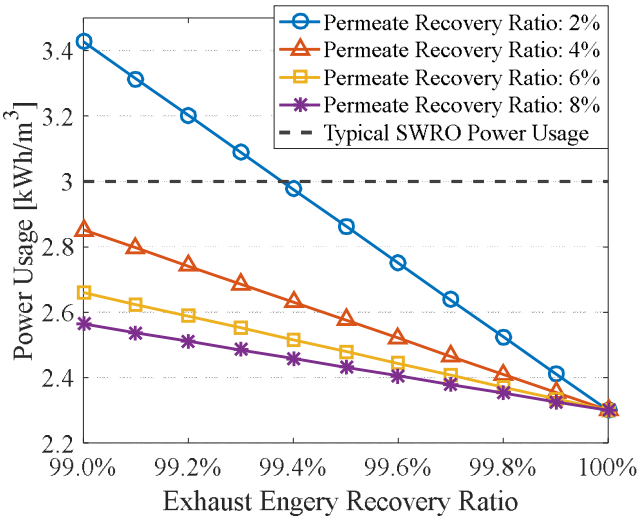

Figure 6.10 Desalination Centrifuge Power Usage Chart

Figure 6.10 shows that at a 2% permeate recovery ratio, if the energy recovery ratio is above 99.4%, the power usage of the desalination centrifuge is less than the industrial average. For all other permeate recovery ratio, the power usage of the desalination centrifuge is less than the industrial average if the energy recovery ratio is above 99%.

7. CONCLUSIONS

Concentration polarization (CP) is an inherent phenomenon in membrane desalination processes. CP is affected by local hydrodynamic and mass transport properties during membrane desalination. Numerical prediction of CP is crucial for the design of membrane separation modules, the optimization of the desalination system performance, and especially the understanding of membrane surface fouling. CP initiates and exacerbates membrane surface fouling. When the mineral salt concentration exceeds the saturation, mineral scaling will be formed on the membrane surface. A numerical prediction of membrane fouling provides an alternative approach for a direct an evaluation of fouling growth, local fluid dynamics and salts concentration distributions in a wide range of operating conditions.

The CP and membrane fouling prediction model is based on the lattice Boltzmann method (LBM). The LBM model allows a simultaneous solution of Navier-Stokes equations and the convection-diffusion equation in a membrane desalination channel. A simple and effective flux boundary scheme is proposed and validated in this study, which involves only the boundary local nodes without utilizing the finite difference approximation or the boundary-neighboring nodes interpolation. The proposed flux boundary scheme is applied to predict CP and simulate fouling growth.

The CP and permeate flux prediction result from LBM agrees well with the FEM benchmark case in a complete rejection condition. With the removal of the complete rejection assumption and with the rejection rate considered, CP is reduced with a lower rejection rate, since more salt ions would be transported through the membrane and accumulated salt ions will be reduced. A higher CP and lower permeate flux in a larger rejection rate condition indicates a trade-off between the membrane selectivity (salt rejection) and the membrane permeability (permeate

flux). Also, prediction results show that the CP boundary layer thickness is almost invariant with different salts rejection rates.

Thereafter, CP in a spacer filled channel shows that there is a higher fouling potential near the spacer-membrane contact corners just in front of and behind the spacer filaments due to higher CP values in these areas.

The LBM model for membrane fouling simulation enables a direct simulation of inorganic fouling growth at a single crystal level with respect to given solution supersaturation near the membrane surface. Both cross-flow velocity and solute concentration are lower around the formed crystal than those in the bulk flow. The predicted gypsum crystal equivalent radius and accumulated mass agree well with published experimental data and analytical results. Simulation result of the gypsum scale retardation by the bicarbonate indicates a stronger gypsum scaling retardation with higher dosage of the bicarbonate and supports the hypothesis that the bicarbonate adsorption onto the gypsum crystals is a plausible mechanism for the retardation of the surface gypsum crystal development.

The present numerical model for the membrane surface fouling growth also enables a direct evaluation of the impacts of antiscalants on the surface fouling development. It also serves as a design tool to aid in identifying suitable operating conditions for membrane filtration processes, or in the dose selection of antiscalants to mitigate inorganic fouling. Antiscalants are surface active materials that interfere with precipitation reactions primarily in ways such as keeping supersaturated solutions of sparingly soluble salts, distorting crystal shapes to get non-adherent scale, or separating crystals from solutions by adsorption. The present LB model only considers the supersaturation altering effect and the surface adsorption effect by the antiscalants, and can be used to provide initial and elementary instructions for dose selection of these mentioned types

antiscalants. However, several parameters are required as inputs for the present simulation model, such as the diffusion coefficient of salts, the supersaturation ratio of solution after the antiscalant effect, the mass transfer coefficient of foulants, and the adsorption equilibrium constant of antiscalants, to predict the CP and fouling formation with antiscalants added. The current model is limited by the availability of the required input parameters for some commercial antiscalants, and by not considering the inherent interactions between different antiscalants, or other chemical effects. A more comprehensive model will better instruct the desalination antiscalant dose selection, and the current numerical study should be viewed as a significant step in that development.

The vibration assisted desalination process is proposed in this study based on the idea of changing the hydrodynamics of the operating conditions, especially increasing the local cross flow velocity. Simulation results and test observations validated that the proposed fouling mitigation technique facilitated reducing CP in membrane desalination processes. Also, the flux decline is slower in vibration assisted desalination than conventional desalination. For example, test results show that after about 7 hours of operation, permeate flux declines 29% without vibration, 20% with 20 Hz vibration, 16% with 53 Hz vibration, and 15% with 55 Hz vibration (all with 1.2 mm vibration amplitude). Selected membrane fouling metrics indicated that there is less fouling formed on the membrane surface under these vibration conditions. Also, correlation between permeate flux and the vibration velocity is established based on test data.

The challenges of improving the membrane desalination performance include the increase of permeate freshwater flux, and the decrease of membrane fouling, power consumption and hardware cost. A novel desalination centrifuge is designed in this study to accomplish these goals by eliminating the cost of the high-pressure feed pump and mitigating membrane fouling

through the vibration assisted desalination technique. Energy consumption calculations show that under certain conditions, the power usage of the desalination centrifuge is less than the industrial average. Typical SWRO system energy usage is about 3.0 kWh/m^3. Ideally, the energy usage of the desalination centrifuge is about 2.3 kWh/m^3, thus there would be 23.3% energy saving per cubic meter of water production. For a 2% permeate recovery ratio of the desalination centrifuge, if the energy recovery ratio is above 99.4%, the power usage of the desalination centrifuge is less than industrial average. For all other permeate recovery ratio, the power usage of the desalination centrifuge is less than the industrial average if the energy recovery ratio of the centrifuge is above 99%.

Future studies may involve the simulation of the crystal nucleation, which is the basis of the crystal growth study for multiple crystals. The developing of a second-order accuracy flux boundary scheme in the LBM framework is also a promising topic.

REFERENCES

[1] B. Van der Bruggen, C. Vandecasteele, Distillation vs. Membrane Filtration: Overview of Process Evolutions in Seawater Desalination, Desalination. 143 (2002) 207–218.

[2] M.F.A. Goosen, S.S. Sablani, H. Al-Hinai, S. Al-Obeidani, R. Al-Belushi, D. Jackson, Fouling of Reverse Osmosis and Ultrafiltration Membranes: A Critical Review, Separation Science and Technology. 39 (2004) 2261–2297.

[3] A. Al-Karaghouli, L.L. Kazmerski, Energy Consumption and Water Production Cost of Conventional and Renewable-Energy-Powered Desalination Processes, Renewable and Sustainable Energy Reviews. 24 (2013) 343–356.

[4] A. Antony, J.H. Low, S. Gray, A.E. Childress, P. Le-Clech, G. Leslie, Scale Formation and Control in High Pressure Membrane Water Treatment Systems: A Review, Journal of Membrane Science. 383 (2011) 1–16.

[5] I.G. Wenten, Khoiruddin, Reverse Osmosis Applications: Prospect and Challenges, Desalination. 391 (2016) 112–125.

[6] C.R. Bouchard, P.J. Carreau, T. Matsuura, S. Sourirajan, Modeling of Ultrafiltration: Predictions of Concentration Polarization Effects, Journal of Membrane Science. 97 (1994) 215–229.

[7] S. Kim, E. Hoek, Modeling Concentration Polarization in Reverse Osmosis Processes, Desalination. 186 (2005) 111–128.

[8] E.M.V. Hoek, M. Elimelech, Cake-Enhanced Concentration Polarization: A New Fouling Mechanism for Salt-Rejecting Membranes, Environmental Science and Technology. 37 (2003) 5581–5588.

[9] S. Shirazi, C.J. Lin, D. Chen, Inorganic Fouling of Pressure-Driven Membrane Processes - A Critical Review, Desalination. 250 (2010) 236–248.

[10] W. Guo, H.H. Ngo, J. Li, A Mini-Review on Membrane Fouling, Bioresource Technology. 122 (2012) 27–34.

[11] W. Gao, H. Liang, J. Ma, M. Han, Z. lin Chen, Z. shuang Han, G. bai Li, Membrane Fouling Control in Ultrafiltration Technology for Drinking Water Production: A Review, Desalination. 272 (2011) 1–8.

[12] C.Y. Tang, T.H. Chong, A.G. Fane, Colloidal Interactions and Fouling of NF and RO Membranes: A Review, Advances in Colloid and Interface Science. 164 (2011) 126–143.

[13] A.L. Zydney, Stagnant Film Model for Concentration Polarization in Membrane Systems, Journal of Membrane Science. 130 (1997) 275–281.

[14] P.L.T. Brian, Concentration Polar Zation in Reverse Osmosis Desalination with Variable Flux and Incomplete Salt Rejection, Industrial and Engineering Chemistry Fundamentals. 4 (1965) 439–445.

[15] D. Bhattacharyya, S.L. Back, R.I. Kermode, M.C. Roco, Prediction of Concentration Polarization and Flux Behavior in Reverse Osmosis by Numerical Analysis, Journal of Membrane Science. 48 (1990) 231–262.

[16] A.S. Berman, Laminar Flow in Channels with Porous Walls, Journal of Applied Physics. 24 (1953) 1232–1235.

[17] F. Li, W. Meindersma, A.B. de Haan, T. Reith, Optimization of Commercial Net Spacers in Spiral Wound Membrane Modules, Journal of Membrane Science. 208 (2002) 289–302.

[18] A. Subramani, S. Kim, E.M. V Hoek, Pressure, Flow, and Concentration Profiles in Open and Spacer-Filled Membrane Channels, Journal of Membrane Science. 277 (2006) 7–17.

[19] M. Shakaib, S.M.F. Hasani, M. Mahmood, Study on the Effects of Spacer Geometry in Membrane Feed Channels Using Three-Dimensional Computational Flow Modeling, Journal of Membrane Science. 297 (2007) 74–89.

[20] S. Ma, L. Song, S.L. Ong, W.J. Ng, A 2-D Streamline Upwind Petrov/Galerkin Finite Element Model for Concentration Polarization in Spiral Wound Reverse Osmosis Modules, Journal of Membrane Science. 244 (2004) 129–139.

[21] L. Song, S. Ma, Numerical Studies of the Impact of Spacer Geometry on Concentration Polarization in Spiral Wound Membrane Modules, Industrial and Engineering Chemistry Research. 44 (2005) 7638–7645.

[22] J. Kromkamp, A. Bastiaanse, J. Swarts, G. Brans, R.G.M. Van Der Sman, R.M. Boom, A Suspension Flow Model for Hydrodynamics and Concentration Polarisation in Crossflow Microfiltration, Journal of Membrane Science. 253 (2005) 67–79.

[23] E. Lyster, Y. Cohen, Numerical Study of Concentration Polarization in a Rectangular Reverse Osmosis Membrane Channel: Permeate Flux Variation and Hydrodynamic End Effects, Journal of Membrane Science. 303 (2007) 140–153.

[24] W. Zhang, J. Luo, L. Ding, M.Y. Jaffrin, A Review on Flux Decline Control Strategies in Pressure-Driven Membrane Processes, Industrial and Engineering Chemistry Research. 54 (2015) 2843–2861.

[25] M. Okazaki, S. Kimura, Scale Formation on Reverse-Osmosis Membranes, Journal of Chemical Engineering of Japan. 17 (1984) 145–151.

[26] J. Gilron, D. Hasson, Calcium Sulphate Fouling of Reverse Osmosis Membranes: Flux Decline Mechanism, Chemical Engineering Science. 42 (1987) 2351–2360.

[27] J. Borden, J. Gilron, D. Hasson, Analysis of RO Flux Decline Due to Membrane Surface

Blockage, Desalination. 66 (1987) 257–269.

[28] M. Brusilovsky, J. Borden, D. Hasson, Flux Decline Due to Gypsum Precipitation on RO Membranes, Desalination. 86 (1992) 187–222.

[29] M. Uchymiak, E. Lyster, J. Glater, Y. Cohen, Kinetics of Gypsum Crystal Growth on a Reverse Osmosis Membrane, Journal of Membrane Science. 314 (2008) 163–172.

[30] A. Rahardianto, W.Y. Shih, R.W. Lee, Y. Cohen, Diagnostic Characterization of Gypsum Scale Formation and Control in RO Membrane Desalination of Brackish Water, Journal of Membrane Science. 279 (2006) 655–668.

[31] E. Lyster, M. man Kim, J. Au, Y. Cohen, A Method for Evaluating Antiscalant Retardation of Crystal Nucleation and Growth on RO Membranes, Journal of Membrane Science. 364 (2010) 122–131.

[32] M. Uchymiak, A. Rahardianto, E. Lyster, J. Glater, Y. Cohen, A Novel RO Ex Situ Scale Observation Detector (EXSOD) for Mineral Scale Characterization and Early Detection, Journal of Membrane Science. 291 (2007) 86–95.

[33] A.I. Radu, L. Bergwerff, M.C.M. van Loosdrecht, C. Picioreanu, A Two-Dimensional Mechanistic Model for Scaling in Spiral Wound Membrane Systems, Chemical Engineering Journal. 241 (2014) 77–91.

[34] S.S. Datta, T.S. Ramakrishnan, D.A. Weitz, Mobilization of a Trapped Non-Wetting Fluid from a Three-Dimensional Porous Medium, AIChE Journal. 55 (2014) 494–504.

[35] N. Prihasto, Q.-F. Liu, S.-H. Kim, Pre-Treatment Strategies for Seawater Desalination by Reverse Osmosis System, Desalination. 249 (2009) 308–316.

[36] M. Elimelech, W.A. Phillip, The Future of Seawater Desalination: Energy, Technology, and the Environment, Science. 333 (2011) 712–717.

[37] C.J. Gabelich, T.I. Yun, B.M. Coffey, I.H.M. Suffet, Effects of Aluminum Sulfate and Ferric Chloride Coagulant Residuals on Polyamide Membrane Performance, Desalination. 150 (2002) 15–30.

[38] M. Al-Ahmad, F.A. Aleem, Scale Formation and Fouling Problems Effect on the Performance of MSF and RO Desalination Plants in Saudi Arabia, Desalination. 93 (1993) 287–310.

[39] A. Sweity, Y. Oren, Z. Ronen, M. Herzberg, The Influence of Antiscalants on Biofouling of RO Membranes in Seawater Desalination, Water Research. 47 (2013) 3389–3398.

[40] E.M. Vrijenhoek, S. Hong, M. Elimelech, Influence of Membrane Surface Properties on Initial Rate of Colloidal Fouling of Reverse Osmosis and Nanofiltration Membranes, Journal of Membrane Science. 188 (2001) 115–128.

[41] J. Gilron, S. Belfer, P. Väisänen, M. Nyström, Effects of Surface Modification on Antifouling and Performance Properties of Reverse Osmosis Membranes, Desalination. 140 (2001) 167–179.

[42] K.Y. Jee, D.H. Shin, Y.T. Lee, Surface Modification of Polyamide RO Membrane for Improved Fouling Resistance, Desalination. 394 (2016) 131–137.

[43] D. Rana, T. Matsuura, Surface Modifications for Antifouling Membranes_2010.PDF, Chemical Reviews. 110 (2010) 2448–2471.

[44] S.K. Gupta, T.R.D. Patel, R.C. Ackerberg, Wall Heat/Mass Transfer in Pulsatile Flow, Chemical Engineering Science. 37 (1982) 1727–1739.

[45] T.J. Kennedy, R.L. Merson, B.J. McCoy, Improving Permeation Flux by Pulsed Reverse Osmosis, Chemical Engineering Science. 29 (1974) 1927–1931.

[46] D.E. Hadzismajlovic, C.D. Bertram, Flux Enhancement in Turbulent Crossflow Microfiltration of Yeast Using a Collapsible-Tube Pulsation Generator, Journal of Membrane Science. 163 (1999) 123–134.

[47] L. Malaeb, G.M. Ayoub, Reverse Osmosis Technology for Water Treatment: State of the Art Review, Desalination. 267 (2011) 1–8.

[48] W. Shi, M.M. Benjamin, Membrane Interactions with NOM and an Adsorbent in a Vibratory Shear Enhanced Filtration Process (VSEP) System, Journal of Membrane Science. 312 (2008) 23–33.

[49] W. Shi, M.M. Benjamin, Fouling of RO Membranes in a Vibratory Shear Enhanced Filtration Process (VSEP) System, Journal of Membrane Science. 331 (2009) 11–20.

[50] W. Shi, M.M. Benjamin, Effect of Shear Rate on Fouling in a Vibratory Shear Enhanced Processing (VSEP) RO System, Journal of Membrane Science. 366 (2011) 148–157.

[51] R. Bian, K. Yamamoto, Y. Watanabe, Effect of Shear Rate on Controlling the Concentration Polarization and Membrane Fouling, Desalination. 131 (2000) 225–236.

[52] S. Lee, R.M. Lueptow, Control of Scale Formation in Reverse Osmosis by Membrane Rotation, Desalination. 155 (2003) 131–139.

[53] S. Chen, D. Martínez, R. Mei, On Boundary Conditions in Lattice Boltzmann Methods, Physics of Fluids. 8 (1996) 2527–2536.

[54] C.K. Aidun, J.R. Clausen, Lattice-Boltzmann Method for Complex Flows, Annual Review of Fluid Mechanics. 42 (2010) 439–472.

[55] J. Zhang, Lattice Boltzmann Method for Microfluidics: Models and Applications, Microfluidics and Nanofluidics. 10 (2011) 1–28.

[56] Y. Chen, Q. Cai, Z. Xia, M. Wang, S. Chen, Momentum-Exchange Method in Lattice Boltzmann Simulations of Particle-Fluid Interactions, Physical Review E - Statistical, Nonlinear, and Soft Matter Physics. 88 (2013) 1–15.

[57] S.D.C. Walsh, M.O. Saar, Macroscale Lattice-Boltzmann Methods for Low Peclet Number Solute and Heat Transport in Heterogeneous Porous Media, Water Resources Research. 46 (2010) 1–15.

[58] Q. Kang, D. Zhang, S. Chen, X. He, Lattice Boltzmann Simulation of Chemical Dissolution in Porous Media, Physical Review E. 65 (2002) 036318.

[59] S. Anwar, M.C. Sukop, Lattice Boltzmann Models for Flow and Transport in Saturated Karst, Groundwater. 47 (2009) 401–413.

[60] P.L. Bhatnagar, E.P. Gross, M. Krook, A Model for Collision Processes in Gases. I. Small Amplitude Processes in Charged and Neutral One-Component Systems, Physical Review. 94 (1954) 511–525.

[61] T. Zhang, B. Shi, Z. Guo, Z. Chai, J. Lu, General Bounce-Back Scheme for Concentration Boundary Condition in the Lattice-Boltzmann Method, Physical Review E. 85 (2012) 016701.

[62] Q. Chen, X. Zhang, J. Zhang, Improved Treatments for General Boundary Conditions in the Lattice Boltzmann Method for Convection-Diffusion and Heat Transfer Processes, Physical Review E. 88 (2013) 033304.

[63] Z. Guo, T.S. Zhao, Lattice Boltzmann Model for Incompressible Flows through Porous Media, Physical Review E. 66 (2002) 036304.

[64] M. Yoshino, T. Inamuro, Lattice Boltzmann Simulations for Flow and Heat/Mass Transfer Problems in a Three-Dimensional Porous Structure, International Journal for Numerical Methods in Fluids. 43 (2003) 183–198.

[65] Y.H. Qian, S.A. Orszag, Lattice Bgk Models for the Navier-Stokes Equation: Nonlinear Deviation in Compressible Regimes, EPL (Europhysics Letters). 21 (1993) 255–259.

[66] Z. Chai, T.S. Zhao, Lattice Boltzmann Model for the Convection-Diffusion Equation, Physical Review E. 87 (2013) 063309.

[67] T. Krüger, F. Varnik, D. Raabe, Shear Stress in Lattice Boltzmann Simulations, Physical Review E. 79 (2009) 046704.

[68] J. Latt, B. Chopard, O. Malaspinas, M. Deville, A. Michler, Straight Velocity Boundaries in the Lattice Boltzmann Method, Physical Review E. 77 (2008) 056703.

[69] C.M. Teixeira, Incorporating Turbulence Models into the Lattice-Boltzmann Method, International Journal of Modern Physics C. 9 (1998) 1159–1175.

[70] R. Huang, H. Wu, A Modified Multiple-Relaxation-Time Lattice Boltzmann Model for Convection-Diffusion Equation, Journal of Computational Physics. 274 (2014) 50–63.

[71] T. Krüger, H. Kusumaatmaja, A. Kuzmin, O. Shardt, G. Silva, E.M. Viggen, The Lattice Boltzmann Method, Springer International Publishing, 2017.

[72] Z. Guo, C. Zheng, B. Shi, Discrete Lattice Effects on the Forcing Term in the Lattice Boltzmann Method, Physical Review E. 65 (2002) 046308.

[73] H.C. Mai, K.H. Lin, C.H. Yang, C.A. Lin, A Thermal Lattice Boltzmann Model for Flows with Viscous Heat Dissipation, CMES - Computer Modeling in Engineering and Sciences. 61 (2010) 45–63.

[74] A.J.C. Ladd, R. Verberg, Lattice-Boltzmann Simulations of Particle-Fluid Suspensions, Journal of Statistical Physics. 104 (2001) 1191–1251.

[75] Q. Zou, X. He, On Pressure and Velocity Boundary Conditions for the Lattice Boltzmann BGK Model, Physics of Fluids. 9 (1997) 1591–1598.

[76] J. Huang, W.A. Yong, Boundary Conditions of the Lattice Boltzmann Method for Convection-Diffusion Equations, Journal of Computational Physics. 300 (2015) 70–91.

[77] L. Li, R. Mei, J.F. Klausner, Boundary Conditions for Thermal Lattice Boltzmann Equation Method, Journal of Computational Physics. 237 (2013) 366–395.

[78] P.H. Kao, R.J. Yang, An Investigation into Curved and Moving Boundary Treatments in the Lattice Boltzmann Method, Journal of Computational Physics. 227 (2008) 5671–5690.

[79] J. Wang, M. Wang, Z. Li, A Lattice Boltzmann Algorithm for Fluid-Solid Conjugate Heat Transfer, International Journal of Thermal Sciences. 46 (2007) 228–234.

[80] H. Yoshida, M. Nagaoka, Multiple-Relaxation-Time Lattice Boltzmann Model for the Convection and Anisotropic Diffusion Equation, Journal of Computational Physics. 229 (2010) 7774–7795.

[81] Q. Kang, D. Zhang, P.C. Lichtner, I.N. Tsimpanogiannis, Lattice Boltzmann Model for Crystal Growth from Supersaturated Solution, Geophysical Research Letters. 31 (2004) L21604.

[82] Q. Kang, P.C. Lichtner, D. Zhang, Lattice Boltzmann Pore-Scale Model for Multicomponent Reactive Transport in Porous Media, Journal of Geophysical Research: Solid Earth. 111 (2006) 1–12.

[83] Q. Kang, P.C. Lichtner, D. Zhang, An Improved Lattice Boltzmann Model for Multicomponent Reactive Transport in Porous Media at the Pore Scale, Water Resources Research. 43 (2007) 1–12.

[84] H.-B. Huang, X.-Y. Lu, M.C. Sukop, Numerical Study of Lattice Boltzmann Methods for

a Convection–Diffusion Equation Coupled with Navier–Stokes Equations, Journal of Physics A: Mathematical and Theoretical. 44 (2011) 055001.

[85] A. Poisson, A. Papaud, Diffusion Coefficients of Major Ions in Seawater, Marine Chemistry. 13 (1983) 265–280.

[86] J. Perko, R.A. Patel, Single-Relaxation-Time Lattice Boltzmann Scheme for Advection-Diffusion Problems with Large Diffusion-Coefficient Heterogeneities and High-Advection Transport, Physical Review E. 89 (2014) 053309.

[87] W. Li, X. Su, A. Palazzolo, S. Ahmed, E. Thomas, Reverse Osmosis Membrane, Seawater Desalination with Vibration Assisted Reduced Inorganic Fouling, Desalination. 417 (2017) 102–114.

[88] H.B. Park, J. Kamcev, L.M. Robeson, M. Elimelech, B.D. Freeman, Maximizing the Right Stuff: The Trade-off between Membrane Permeability and Selectivity, Science. 356 (2017) eaab0530.

[89] W.Y. Shih, A. Rahardianto, R.W. Lee, Y. Cohen, Morphometric Characterization of Calcium Sulfate Dihydrate (Gypsum) Scale on Reverse Osmosis Membranes, Journal of Membrane Science. 252 (2005) 253–263.

[90] H.J. Oh, Y.K. Choung, S. Lee, J.S. Choi, T.M. Hwang, J.H. Kim, Scale Formation in Reverse Osmosis Desalination: Model Development, Desalination. 238 (2009) 333–346.

[91] F. Alimi, A. Gadri, Kinetics and Morphology of Formed Gypsum, Desalination. 166 (2004) 427–434.

[92] P. Dydo, M. Turek, J. Ciba, K. Wandachowicz, J. Misztal, The Nucleation Kinetic Aspects of Gypsum Nanofiltration Membrane Scaling, Desalination. 164 (2004) 41–52.

[93] S. Lee, C.H. Lee, Effect of Operating Conditions on CaSO4 Scale Formation Mechanism in Nanofiltration for Water Softening, Water Research. 34 (2000) 3854–3866.

[94] A. Rahardianto, B.C. Mccool, Y. Cohen, Reverse Osmosis Desalting of Inland Brackish Water of High Gypsum Scaling Propensity: Kinetics and Mitigation of Membrane Mineral Scaling, Environmental Science and Technology. 42 (2008) 4292–4297.

[95] K.J. Kim, A. Mersmann, Estimation of Metastable Zone Width in Different Nucleation Processes, Chemical Engineering Science. 56 (2001) 2315–2324.

[96] M.C. Porter, Concentration Polarization with Membrane Ultrafiltration, Industrial and Engineering Chemistry Product Research and Development. 11 (1972) 234–248.

[97] J. Wang, D.S. Dlamini, A.K. Mishra, M.T.M. Pendergast, M.C.Y. Wong, B.B. Mamba, V. Freger, A.R.D. Verliefde, E.M.V. Hoek, A Critical Review of Transport through Osmotic Membranes, Journal of Membrane Science. 454 (2014) 516–537.

[98] I. Sutzkover, D. Hasson, R. Semiat, Simple Technique for Measuring the Concentration Polarization Level in a Reverse Osmosis System, Desalination. 131 (2000) 117–127.

[99] D. Rana, T. Matsuura, Surface Modifications for Antifouling Membranes, Chemical Reviews. 110 (2010) 2448–2471.

[100] E.W. Tow, J.H. Lienhard, Quantifying Osmotic Membrane Fouling to Enable Comparisons across Diverse Processes, Journal of Membrane Science. 511 (2016) 92–107.

[101] M.A. Javeed, K. Chinu, H.K. Shon, S. Vigneswaran, Effect of Pre-Treatment on Fouling Propensity of Feed as Depicted by the Modified Fouling Index (MFI) and Cross-Flow Sampler-Modified Fouling Index (CFS-MFI), Desalination. 238 (2009) 98–108.

[102] J.C. Schippers, J. Verdoum, The Modified Fouling Index, a Method of Determining the Fouling Characteristics of Water, Desalination. 32 (1980) 137–148.

[103] K. Katsoufidou, S.G. Yiantsios, A.J. Karabelas, Experimental Study of Ultrafiltration Membrane Fouling by Sodium Alginate and Flux Recovery by Backwashing, Journal of Membrane Science. 300 (2007) 137–146.

[104] A. Alhadidi, A.J.B. Kemperman, B. Blankert, J.C. Schippers, M. Wessling, W.G.J. van der Meer, Silt Density Index and Modified Fouling Index Relation, and Effect of Pressure, Temperature and Membrane Resistance, Desalination. 273 (2011) 48–56.

[105] E. Brauns, E. Van Hoof, B. Molenberghs, C. Dotremont, W. Doyen, R. Leysen, A New Method of Measuring and Presenting the Membrane Fouling Potential, Desalination. 150 (2002) 31–43.

[106] J.R. Werber, A. Deshmukh, M. Elimelech, Can Batch or Semi-Batch Processes Save Energy in Reverse-Osmosis Desalination?, Desalination. 402 (2017) 109–122.

[107] P.M. Wild, G.W. Vickers, N. Djilali, The Fundamental Principles and Design Considerations for the Implementation of Centrifugal Reverse Osmosis, Proceedings of the Institution of Mechanical Engineers, Part E. 211 (1997) 67–81.

[108] H. Mallubhotla, G. Belfort, Flux Enhancement during Dean Vortex Microfiltration. 8. Further Diagnostics, Journal of Membrane Science. 125 (1997) 75–91.

APPENDIX A

Appendix A covers the derivation of the proposed flux boundary scheme. Since curved boundaries can be approximated by zig-zag staircases, a straight boundary will be used for the illustrating the derivation process. Substituting concentration distribution functions (in post-streaming form) on the top boundary illustrated in Figure A1.1 into Equation (2.44) yields Equation (A1.1).

$$\frac{\delta y}{\delta t}\underbrace{\left(g_2+g_5+g_6\right)}_{\text{known}}-\frac{\delta y}{\delta t}\underbrace{\left(g_4+g_7+g_8\right)}_{\text{unknown}}=u_y C-\frac{\tau}{3}\frac{\delta y^2}{\delta t}\frac{\partial C}{\partial y} \tag{A1.1}$$

In Equation (A1.1), $c = \delta y/\delta t$ is the lattice speed contained in the discrete velocity $\mathbf{e}_i$. There are no available distribution functions streaming from wall nodes ($y = NY+1$) to the boundary nodes ($y = NY$), thus g_4, g_7, g_8 are unknown distribution functions after the streaming operation. These unknown distribution functions should be prescribed and constrained by certain boundary conditions. For all interior nodes in the simulation domain, post-streaming distribution functions will be calculated based on neighboring post-collision distribution functions. Similarly, unknown post-streaming distribution functions of g_4, g_7 and g_8 on boundary mass nodes can also be calculated by post-collision distribution functions g_2^+, g_5^+, and g_6^+.

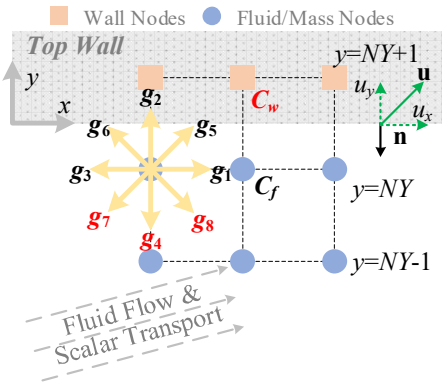

Figure A1.1 Illustration of a Top Boundary

Referring to Figure A1.1, calculated post-streaming distribution functions g_2, g_5 and g_6 at boundary wall nodes ($y = NY+1$) equal post-collision distributions g_2^+, g_5^+, and g_6^+ at boundary mass nodes ($y = NY$), respectively, as expressed in Equation (A1.2).

$$\begin{cases} g_2(x, NY+1) = g_2^+(x, NY) \\ g_5(x+1, NY+1) = g_5^+(x, NY) \\ g_6(x-1, NY+1) = g_6^+(x, NY) \end{cases} \tag{A1.2}$$

From the approximation equation shown in Equation (2.46), concentration gradients can be estimated by distribution functions at boundary wall nodes and boundary mass nodes, as shown in Equation (A1.3).

$$\begin{cases} \dfrac{g_2(x, NY+1) - g_2(x, NY)}{\delta y} = w_2 \dfrac{C_w - C_f}{\delta y} \\ \dfrac{g_5(x+1, NY+1) - g_5(x, NY)}{\delta y} = w_5 \dfrac{\left(C_w + \dfrac{\delta C_w}{\delta x}\delta x\right) - C_f}{\delta y} \\ \dfrac{g_6(x-1, NY+1) - g_6(x, NY)}{\delta y} = w_6 \dfrac{\left(C_w - \dfrac{\delta C_w}{\delta x}\delta x\right) - C_f}{\delta y} \end{cases} \tag{A1.3}$$

Note that in Equation (A1.3), the variation of the wall concentration at a given node along the x direction is linearized using the first order Taylor expansion around the given node. Combining of Equation (A1.2) and Equation (A1.3) yields the relation between unknown post-streaming distribution functions and known post-collision distribution functions at boundary mass nodes, as shown in Equation (A1.4).

$$(g_2 + g_5 + g_6) = (g_2^+ + g_5^+ + g_6^+) - 1/6\,\delta y (C_w - C_f)/\delta y = (g_2^+ + g_5^+ + g_6^+) - 1/6\,\delta y \frac{\partial C}{\partial y} \tag{A1.4}$$

In Equation (A1.4), weight coefficients in the lattice Boltzmann model are substituted, as $w_2 = 1/9$, $w_5 = 1/36$, $w_6 = 1/36$, and $w_2+w_5+w_6 = 1/6$. Also, the first-order normal derivative $\partial C/\partial \mathbf{n}$

on the right-hand side of Equation (A1.4) is the replacement of the finite difference scheme approximation $(C_w\text{-}C_f)/\delta y$ on the right-hand side of Equation (A1.3). Finally, Equation (A1.5) can be derived when substitute $(g_2+g_5+g_6)$ from Equation (A1.4) into Equation (A1.1).

$$\frac{\delta y}{\delta t}\left(g_4+g_7+g_8\right)-\frac{\delta y}{\delta t}\left(g_2^+ + g_5^+ + g_6^+\right)=-\left(u_y C-\frac{(\tau-1/2)}{3}\frac{(\delta y)^2}{\delta t}\frac{\partial C}{\partial y}\right) \qquad \text{(A1.5)}$$

The right-hand side of Equation (A1.5) is actually total mass flux flowing from the top wall to the fluid phase (the surface normal **n** direction), and the coefficient term of the concentration gradient is the diffusion coefficient, i.e. $D = (\tau_s\text{-}1/2)(\delta h)^2/(3\delta t)$ from Equation (2.8). Equation (A1.5) is the general implementation form appearing in the mass flux boundary scheme for a top straight boundary. During the implementation process, unknown post-streaming distribution functions g_4, g_7 and g_8 can be calculated by the post-collision form of known distribution functions g_2^+, g_5^+, and g_6^+. The implementation form of Equation (A1.5) can be expressed in a general form shown in Equation (A1.6) or Equation (2.45).

$$\begin{aligned}&\underbrace{\sum_{\mathbf{e}_i\cdot\mathbf{n}>0} g_i\mathbf{e}_i\cdot\mathbf{n}}_{\text{unkonwn}}+\underbrace{\sum_{\mathbf{e}_i\cdot\mathbf{n}\le 0} g_i^+\mathbf{e}_i\cdot\mathbf{n}}_{\text{konwn}}=\left(\mathbf{u}C-D\nabla C\right)\cdot\mathbf{n}=\mathbf{J}_\sigma\cdot\mathbf{n}\\&=\left[\left(u_x-D\,\partial C/\partial x\right)\mathbf{i}+\left(u_y-D\,\partial C/\partial y\right)\mathbf{j}+\left(u_z-D\,\partial C/\partial z\right)\mathbf{k}\right]\cdot\mathbf{n}\end{aligned} \qquad \text{(A1.6)}$$

Although Equation (A1.6) is the general form of Equation (A1.5) which is valid for top boundaries, as will be discussed, Equation (A1.6) is also correct for the bottom boundary. The top and the bottom boundaries are also representatives to the right and left boundaries due to the similarity of surface normal directions. Consequently, Equation (A1.6) is valid for curved boundaries with staircase approximations comprising all straight boundaries.

For the bottom boundary illustrated in Figure A1.2, substituting concentration distribution functions (in post-streaming form) on the bottom boundary illustrated in Figure A1.2 into Equation (2.44) yields Equation (A1.7).

$$\frac{\delta y}{\delta t}\underbrace{\left(g_2+g_5+g_6\right)}_{\text{unknown}}-\frac{\delta y}{\delta t}\underbrace{\left(g_4+g_7+g_8\right)}_{\text{known}}=u_y C-\frac{\tau}{3}\frac{\delta y^2}{\delta t}\frac{\partial C}{\partial y} \tag{A1.7}$$

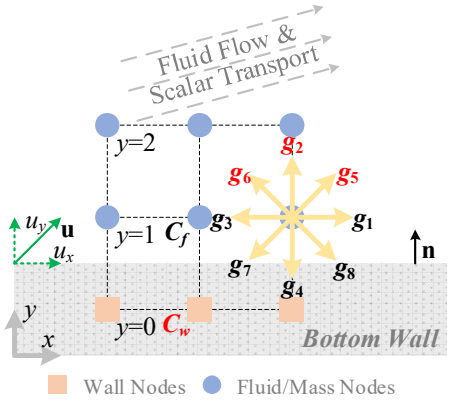

Figure A1.2 Illustration of a Bottom Boundary

Similar to Equation (A1.2) and referring Figure A1.2, calculated post-streaming distribution functions g_4, g_7 and g_8 at boundary wall nodes ($y = 0$) equal post-collision distributions g_4^+, g_7^+, and g_8^+ at boundary mass nodes ($y = 1$), respectively, as expressed in Equation (A1.8).

$$\begin{cases} g_4\left(x,0\right)=g_4^+\left(x,1\right) \\ g_7\left(x+1,0\right)=g_7^+\left(x,1\right) \\ g_8\left(x-1,0\right)=g_8^+\left(x,1\right) \end{cases} \tag{A1.8}$$

From the approximation equations in Equation (2.45), concentration gradients can be estimated by distribution functions at boundary wall nodes and boundary mass nodes, as shown in Equation (A1.9).

$$\begin{cases} \dfrac{g_4\left(x,0\right)-g_4\left(x,1\right)}{\delta y}=w_4\dfrac{C_w-C_f}{\delta y} \\ \dfrac{g_7\left(x+1,0\right)-g_7\left(x,1\right)}{\delta y}=w_7\dfrac{\left(C_w+\dfrac{\delta C_w}{\delta x}\delta x\right)-C_f}{\delta y} \\ \dfrac{g_8\left(x-1,0\right)-g_8\left(x,1\right)}{\delta y}=w_8\dfrac{\left(C_w-\dfrac{\delta C_w}{\delta x}\delta x\right)-C_f}{\delta y} \end{cases} \tag{A1.9}$$

Combining of Equation (A1.8) and Equation (A1.9) yields the relation between unknown post-streaming distribution functions and known post-collision distribution functions at boundary mass nodes, as shown in Equation (A1.10).

$$\left(g_4+g_7+g_8\right)=\left(g_4^+ + g_7^+ + g_8^+\right)-1/6\,\delta y\left(C_w-C_f\right)\Big/\delta y=\left(g_4^+ + g_7^+ + g_8^+\right)+1/6\,\delta y\frac{\partial C}{\partial y} \quad \text{(A1.10)}$$

Finally, Equation (A1.11) can be derived when substitute (g_4+g_7+g_8) from Equation (A1.10) into Equation (A1.7).

$$\frac{\delta y}{\delta t}\left(g_2+g_5+g_6\right)-\frac{\delta y}{\delta t}\left(g_4^+ + g_7^+ + g_8^+\right)=u_y C-\frac{\left(\tau-1/2\right)}{3}\frac{\left(\delta y\right)^2}{\delta t}\frac{\partial C}{\partial y} \quad \text{(A1.11)}$$

So, it is demonstrated that Equation (A1.11) can also described by the general form of Equation (A1.6). For a standard square lattice, the non-dimensional lattice spacing $\delta h = \delta x = \delta y = 1$. The lattice time step δt is set to 1 so that the particles travel one lattice spacing during one time-step. So, in Equation (A1.6), both $\mathbf{e}_i$ and $\mathbf{n}$ are unit vectors. The mass flux vector $\mathbf{J}_\sigma$ in Equation (A1.6) is defined in the Cartesian coordinate system. The surface normal vector $\mathbf{n}$ pointing outward to the fluid phase works to redirect total mass flux to the normal vector direction (mass flux flows out of the solid phase toward the fluid phase, normal to the boundary). Also, the unit normal vector $\mathbf{n}$ should be in one of the three cartesian coordinate directions. Thus, the present boundary scheme works for curved boundaries in staircase form. Finally, the relation between the first-order moment of distribution functions and heat/mass flux shown in Equation (A1.6) is valid for both interior nodes and boundary nodes of the simulation domain.

APPENDIX B

Appendix B covers the conversion procedures between physical SI units (International System of Units) and dimensionless LBM units. In the lattice Boltzmann method, units of physical quantities are usually dimensionless. Also, lattice spacing and time step are usually selected to be unity ($\delta x = \delta y = \delta t = 1$), thus the lattice speed $c = 1$. Furthermore, some special dimensionless numbers are frequently used to characterize the target system. For example, flows with same Reynolds numbers (Re = uL/v) are equivalent for hydrodynamics, and solutions with same Schmidt numbers (Sc = v/D) are equivalent for mass transport. A physical quantity Q can be written with a number and a unit, as $Q = \bar{Q} \times C_Q$, in which, Q is a physical quantity with a physical unit $[Q]$, $\bar{Q}$ is a dimensionless quantity with a dimensionless unit $[\bar{Q}] = 1$ and C_Q is the conversion factor from $\bar{Q}$ to Q with a unit $[C_Q] = [Q]$. Dimensionless numbers such as the Reynolds number and the Schmidt number should be invariant whether in a physical unit or in a dimensionless LBM unit. Assuming that flows with the same Re and Sc are equivalent, thus the conversion factors should be 1, as shown in Equation (2.1).

$$\mathrm{Re} = \overline{\mathrm{Re}} \Leftrightarrow C_{\mathrm{Re}} \doteq 1 \tag{A2.1}$$

There are a variety of conversion methods between physical SI units and dimensionless LBM units. The following procedures are followed in this paper. Note that a symbol with an overhead bar denotes a dimensionless quantity.

(1) General input parameters include: Channel height: $H = 1\times10^{-3}$ [m]; Kinematic viscosity of water: $v = 1\times10^{-6}$ [m2/s]; Density of water: $\rho = 1\times10^{3}$ [kg/m3]; Diffusion coefficient of ions in seawater: D = 1.5×10^{-9} [m2/s];

(2) Mesh resolution or node number of the channel height $H_{LBM} = 100$.

Conversion factor of length: $C_H = H/H_{LBM}$, [m].

(3) LBM density is generally selected to be 1: $\rho_{LBM} = 1$.

Conversion factor of density: $C_\rho = \rho/\rho_{LBM}$, [kg/m3].

(4) Set the relaxation time for concentration field: $\tau_s = 0.51$.

(5) Set a reference diffusion coefficient $D_{ref} = kD$ (k>0, the coefficient k is case dependent);

For convenience, choose a unit lattice spacing and a unit time step, as shown in Equation (A2.2).

$$\overline{\Delta x} = 1,\ \overline{\Delta t} = 1 \Rightarrow c = \overline{\Delta x} / \overline{\Delta t} = 1 \tag{A2.2}$$

(6) Schmidt number: $\mathrm{Sc} = \nu / D_{ref}$;

(7) Conversion factor of time can be shown in Equation (A2.3).

$$C_T = \frac{C_H^2 \left(\tau_s - 1/2\right)}{3 D_{ref}} \tag{A2.3}$$

(8) Conversion factor of velocity: $C_U = C_H / C_T$;

(9) Conversion factor of force per volume: $C_F = C_\rho C_H / C_T^2$;

(10) Diffusion coefficient in dimensionless unit can be shown in Equation (A2.4).

$$\overline{D} = D_{ref} C_T \big/ C_H^2 \tag{A2.4}$$

(11) Kinematic viscosity in dimensionless unit can be shown in Equation (A2.5).

$$\overline{\nu} = \overline{D} \times \mathrm{Sc} \tag{A2.5}$$

(12) Relaxation time for fluid can be shown in Equation (A2.6).

$$\tau = 3\overline{\nu} + 1/2 \tag{A2.6}$$

Usually, the calculated Mach number in the LBM unit system is larger than calculated in the physical unit system due to the smaller sound speed in LBM, otherwise the simulations would be too expensive. LBM simulates incompressible flow under a low Mach number condition (Ma = u/c_s<0.3, where u is the macroscopic flow velocity and c_s is the speed of sound) with a weak variation in density.